Inorganic Chemistry
Viewpoint
Cite This: *Inorg. Chem.* 2019, 58, 14939−14980
pubs.acs.org/IC

Viewpoint: Atomic-Scale Design Protocols toward Energy, Electronic, Catalysis, and Sensing Applications

Florian Belviso,[†] Victor E. P. Claerbout,[†] Aleix Comas-Vives,[‡] Naresh S. Dalal,[§,‖] Feng-Ren Fan,[⊥] Alessio Filippetti,[#] Vincenzo Fiorentini,[#] Lucas Foppa,[∇] Cesare Franchini,[○,◆] Benjamin Geisler,[⊕] Luca M. Ghiringhelli,[⊗] Axel Groß,[◑,◐] Shunbo Hu,[◒] Jorge Íñiguez,[◓,◩] Steven Kaai Kauwe,[⬕] Janice L. Musfeldt,[◪] Paolo Nicolini,[†] Rossitza Pentcheva,[⊕] Tomas Polcar,[†] Wei Ren,[◒] Fabio Ricci,[⬡] Francesco Ricci,[⬢] Huseyin Sener Sen,[†] Jonathan Michael Skelton,[⬠] Taylor D. Sparks,[⬕] Alessandro Stroppa,[◭] Andrea Urru,[#,◀] Matthias Vandichel,[⊖,⦶] Paolo Vavassori,[◨,▶] Hua Wu,[⊥,◧] Ke Yang,[⊥] Hong Jian Zhao,[◓,⬒] Danilo Puggioni,[*,⬓] Remedios Cortese,[*,⬔] and Antonio Cammarata[*,†]

[†] Department of Control Engineering, Czech Technical University in Prague, Technicka 2, 16627 Prague 6, Czech Republic

[‡] Department of Chemistry, Universitat Autònoma de Barcelona, 08193 Cerdanyola del Vallès, Catalonia, Spain

[§] National High Magnet Field Lab, Tallahassee, Florida 32310, United States

[‖] Department of Chemistry & Biochemistry, Florida State University, Tallahassee, Florida 32306, United States

[⊥] Laboratory for Computational Physical Sciences (MOE), State Key Laboratory of Surface Physics, and Department of Physics, Fudan University, Shanghai 200433, China

[#] Department of Physics at University of Cagliari, and CNR-IOM, UOS Cagliari, Cittadella Universitaria, I-09042 Monserrato (CA), Italy

[∇] Department of Chemistry and Applied Biosciences, ETH Zürich, Vladimir-Prelog-Weg 1-5, CH-8093 Zürich, Switzerland

[○] Faculty of Physics and Center for Computational Materials Science, University of Vienna, Sensengasse 8, A-1090 Vienna, Austria

[◆] Dipartimento di Fisica e Astronomia, Università di Bologna, Bologna 40127, Italy

[⊕] Department of Physics and Center for Nanointegration (CENIDE), Universität Duisburg-Essen, Lotharstr. 1, Duisburg 47057, Germany

[⊗] Fritz-Haber-Institut der Max-Planck-Gesellschaft, Berlin-Dahlem 14195, Germany

[◑] Electrochemical Energy Storage, Helmholtz Institut Ulm, Ulm 89069, Germany

[◐] Institute of Theoretical Chemistry, Ulm University, Ulm 89069, Germany

[◒] Department of Physics, Materials Genome Institute, and International Center of Quantum and Molecular Structures, Shanghai University, 99 Shangda Road, Shanghai 200444, China

[◓] Materials Research and Technology Department, Luxembourg Institute of Science and Technology, Avenue des Hauts-Fourneaux 5, L-4362 Esch/Alzette, Luxembourg

[⊖] Department of Chemical Sciences and Bernal Institute, Limerick University, Limerick, Ireland

[⦶] Department of Chemistry and Material Science and Department of Applied Physics, Aalto University, Espoo 02150, Finland

[◨] CIC nanoGUNE, San Sebastian E-20018, Spain

[◧] Collaborative Innovation Center of Advanced Microstructures, Nanjing 210093, China

[⬒] Physics Department and Institute for Engineering, University of Arkansas, Fayetteville, Arkansas 72701,United States

[⬓] Department of Materials Science and Engineering, Northwestern University, 2220 Campus Drive, Evanston, Illinois 60208, United States

[⬔] Department of Physics and Chemistry, Università degli Studi di Palermo, Viale delle Scienze ed. 17, Palermo 90128, Italy

[◩] Physics and Materials Research Unit, University of Luxembourg, Rue du Brill 41, Belvaux L-4422, Luxembourg

[⬕] Materials Science & Engineering Department, University of Utah, 122 Central Campus Drive, Salt Lake City, Utah 84112, United States

[◪] Department of Chemistry, University of Tennessee, Knoxville, Tennessee 37996, United States

[⬡] Physique Theorique des Materiaux, Universite de Liege, Sart-Tilman B-4000, Belgium

[⬢] Institute of Condensed Matter and Nanosciences, Universite Catholique de Louvain, Chemin des Etoiles 8, Louvain-la-Neuve B-1348, Belgium

[⬠] Department of Chemistry, University of Manchester, Oxford Road, Manchester M13 9PL, United Kingdom

[◭] CNR-SPIN, Department of Physical Sciences and Chemistry, Universita degli Studi dell'Aquila, Via Vetoio, Coppito (AQ) 67010, Italy

[▶] IKERBASQUE, Basque Foundation for Science, Bilbao 48013, Spain

Received: June 20, 2019
Published: October 31, 2019

DOI: 10.1021/acs.inorgchem.9b01785
Inorg. Chem. 2019, 58, 14939−14980

ABSTRACT: Nanostructured materials are essential building blocks for the fabrication of new devices for energy harvesting/storage, sensing, catalysis, magnetic, and optoelectronic applications. However, because of the increase of technological needs, it is essential to identify new functional materials and improve the properties of existing ones. The objective of this Viewpoint is to examine the state of the art of atomic-scale simulative and experimental protocols aimed to the design of novel functional nanostructured materials, and to present new perspectives in the relative fields. This is the result of the debates of Symposium I “Atomic-scale design protocols towards energy, electronic, catalysis, and sensing applications”, which took place within the 2018 European Materials Research Society fall meeting.

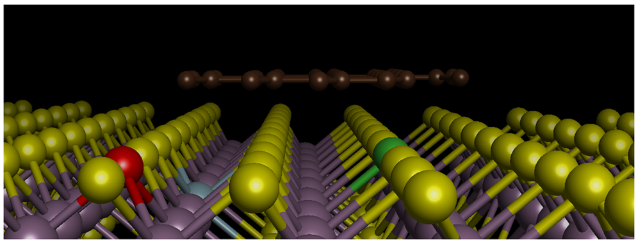

1. INTRODUCTION

Modern technology has a huge impact on our everyday life. For example, nowadays a vast number of tasks can be performed with a couple of clicks. Functional materials, that is, materials exhibiting adaptive capabilities to external stimuli,[1] form the basis for a wide range of technologies. Their societal impact is tantamount in energy harvesting/storage, sensing, catalysis, magnetic, and optoelectronic applications.

During the last years, intensive research activities have been devoted to the synthesis and characterization of nanomaterials. The discovery of novel materials with desirable properties, however, requires that we understand the atomic structural principles governing the functional response. In this perspective, the Symposium I “Atomic-scale design protocols towards energy, electronic, catalysis, and sensing applications”, which took place within the 2018 European Materials Research Society fall meeting, focused on the recent developments of design strategies for smart materials. Here, the outcomes of the Symposium’s debates are reported.

This Viewpoint first focuses on general technical aspects of performing first-principles calculations, on creating integrated data infrastructures and extracting useful information from them, and on issues related to machine learning techniques. Materials and processes for energy conversion through catalysis and hazards in energy storage in batteries are then addressed. A broad range of functional materials is covered in the remaining sections of this Viewpoint, from molecular solids and metallic multilayer composites, oxide thermoelectrics, and “ferroelectric” metals to hybrid organic−inorganic perovskites and triboelectric materials. These examples illustrate the challenges in understanding and improving functional materials, but they also demonstrate the progress that has been made on an atomistic level by advanced techniques, both in theoretical and experimental studies. Particular emphasis has been put on synergistic investigations involving experimentals, materials informatics, and computational approaches, which can provide the fundamental understanding of these materials as well as new insights necessary to guide and accelerate the search of materials with targeted functionalities.

2. PREDICTING THE BAND GAP OF COMPLEX MATERIALS: COMPUTATIONAL METHODS AND PROCEDURES

The prediction and interpretation of materials properties requires the combination of advanced theoretical models and accurate numerical schemes. For decades, density functional theory (DFT)[2,3] has been the primary method to estimate the ground-state properties of materials, and it still represents a common methodological scheme for studying a wide variety of physical phenomena, including those reviewed in the present Viewpoint. Despite its great success, DFT has some limitations arising from the approximation used to construct the exchange and correlation functionals that hinders its performance. An archetypal shortcoming of DFT is the calculation of the band gap, a property of fundamental importance and crucial for all practical applications, including energy, electronic, catalysis, and sensing applications, which are the main focus of this work and will be elaborated and discussed more extensively in the following sections. A variety of quantum-mechanical methods has been proposed to cure this problem, including local corrections inspired by the Hubbard-based models[4] (e.g., DFT +U and self-interaction corrected schemes), hybrid functionals

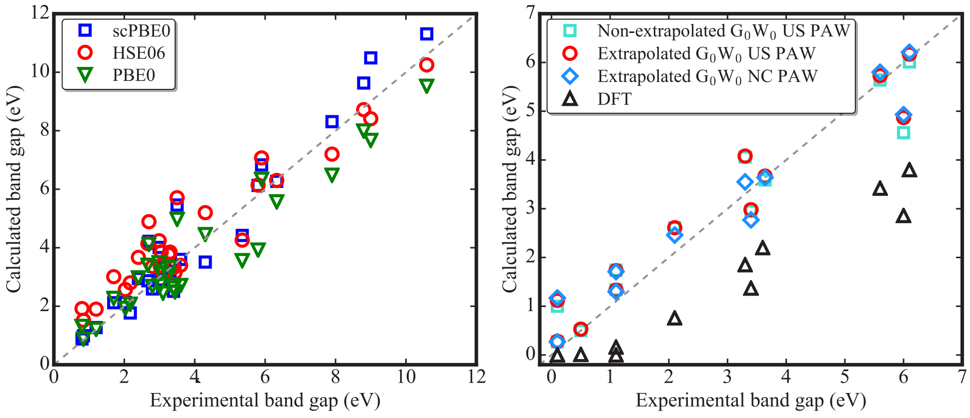

Figure 1. Comparison between calculated and experiment band gaps. (a) Hybrid functionals for a data set including 30 semiconductors and (b) GW applied to a perovskite data set including 3d, 4d, and 5d transition metals. Adapted from refs 10 and 12.

DOI: 10.1021/acs.inorgchem.9b01785
Inorg. Chem. 2019, 58, 14939−14980

(e.g., see refs 5−7), quasiparticle approaches[8] (GW), and, for what concern the optical excitations, the Bethe-Salpeter equation (BSE).[9]

2.1. scPBE0 Hybrid Functional. A promising compromise between the computational cost and the accuracy of the calculated band gap value is represented by hybrid functionals. Figure 1 shows a selection of hybrid functional band gaps computed for a wide set of insulating and semiconducting materials.[10] Despite the research effort made so far, further investigation is still needed to improve the prediction of the band gap value, which mainly relies on mixing parameters at the basis of the hybrid energy functional formulation. As an example, the procedure to carry one scPBE0[10] calculation is here concisely described, which is one of the last members of the hybrid family.

The scPBE0 hybrid energy functional is based on the self-consistent evaluation of the mixing parameter α, which controls the amount of HF exchange.[10]is the This is done by means of an iterative calculation of the static dielectric constant using the perturbation expansion after discretization (PEAD) method.[11] Specifically, one starts the self-consistent loop by using the standard mixing $\alpha_{\text{in}} = 0.25$. At the end of this iteration the output mixing α_{out} is determined as the inverse of the mean value of the diagonal elements of the dielectric function evaluated by PEAD; that is, $\alpha_{\text{out}} = 1/\bar{\varepsilon}_\infty$, where ε_∞ is the ion-clamped static dielectric tensor. This new value of α is then used to start a new iteration. The self-consistent procedure stops when $\alpha_{\text{out}} - \alpha_{\text{in}}$ is smaller than the desired accuracy (usually $\sim 10^{-2}$).

The results obtained by fixed-α (PBE0 and HSE03) and self-consistent (scPBE0) hybrids (Figure 1 show that scPBE0 performs better for band gaps smaller than ~8 eV, whereas for larger gaps PBE0 appears to be a better choice. The nonempirical extension of range-separated hybrids, in which not only the mixing parameters α but also the screening length (typically labeled μ in HSE-like hybrids), represents a possible route for improvement. Following this idea, a new class of nonempirical hybrid functionals based on a model dielectric function has been recently proposed that indeed predicts accurately band gaps for both narrow- and wide-gap semiconductor.[13] The next level of theory, which allows the computation of quasiparticle energies and guarantees an improved prediction of band gaps, is the GW method.[8]

2.2. GW Method. The GW method is probably the most accurate approach presently available for condensed matter physics calculations. Alternative advanced methodologies have been developed in other sectors, for example, quantum-chemistry methods, such as Møller−Plesset perturbation and coupled cluster theories,[14] which are however still computationally too demanding when applied to complex extended systems. The essence of the GW scheme is the inclusion of the self-energy, defined as $\Sigma = iGW$ (where G is the single particle Green's function, and W is the screened Coulomb interaction), in the generalized Kohn−Sham equations. Regrettably enough, despite its success, the proper use of the GW method is not well-established from a technical point of view, yielding to nonconverged solutions. In fact, the convergence criteria requires a summation over many empty states (N) and a sufficiently dense k-points mesh resulting in large computational cost and memory requirements. However, two different routes can be followed to obtained converged results:[12]

1. *Basis-set extrapolation.* The core aspect of this scheme is to extrapolate the quasi-particle (QP) energies obtained using a finite-basis-set to the infinite-basis-set limit through the formulawhere $E(N_k,N)$ is the calculated QP energies with N_k **k**-points and N bands, $E(N_k, N_\infty)$ is the corresponding extrapolated ($N \to \infty$) QP energies, and the variables n_k and N_k indicate the number of **k**-points in the small and large **k**-point mesh, respectively.

2. *Conventional scheme.* This method attempts to converge the QP energies with respect to a set of three parameters: number of bands, energy cutoff for the plane wave expansion for the orbitals E_{pw}, and the number of **k**-points.

$$E_\infty(N_k, N_\infty) \approx \underbrace{E_\infty(n_k, N_\infty) - E(n_k, N)}_{\Delta_N(n_k)} \overbrace{ + E(N_k, N)}^{\Delta_k(N)} \quad (1)$$

An important aspect to consider when performing GW calculations is the choice of the pseudopotential. Even though accurate results can be also obtained with ultrasoft pseudopotentials, it is recommended, when possible, to adopt norm-conserving pseudopotentials. Following the above consideration one can achieve a remarkably good fundamental band gap for a wide set of transition metal perovskites, as shown in Figure 1.

An additional ambiguity, which is often a source of confusion, is the difference between fundamental electronic gap, that is, the energy difference between the lowest unoccupied state and the highest occupied one, and the optical gap, which includes electron−hole interaction and is lower than the fundamental electronic gap by an amount that is typically referred to as excitonic energy.[15] Excitonic effects, not included in the GW scheme, can be accounted for by using the Bethe-Salpeter equation, in which the response function is computed from the Dyson-like equation.[16]

2.3. BSE Calculations. The procedure to conduct BSE calculations consists of four steps:[17]

1. Standard self-consistent DFT calculations. If the DFT ground state turns out to be metallic it is necessary to add a small U or a scissor operator (only in this step).

2. Additional DFT step to compute the one-electron wave functions and eigenenergies of all virtual orbitals evaluated by an exact diagonalization.

3. G_0W_0 runs to compute the QP energies and static screened interaction W, and

4. BSE run (typically in the Tamm-Dancoff approximation[18]) to compute the frequency-dependent macroscopic dielectric function

$$\varepsilon(\omega) = 1 - \lim_{q \to 0} V(\mathbf{q}) \sum_\Lambda \left(\frac{1}{\omega - \Omega_\Lambda + i\eta} - \frac{1}{\omega + \Omega_\Lambda - i\eta} \right) \times \left\{ \sum_{\mathbf{k}} \omega_{\mathbf{k}} \sum_{v,c} \langle \psi_{c\mathbf{k}} | e^{i\mathbf{q}\cdot\mathbf{r}} | \psi_{v\mathbf{k}} \rangle X^\Lambda_{cv\mathbf{k}} \right\} \times \{c.\ c.\} \quad (2)$$

with the oscillator strengths S_Λ associated with the optical transitions defined by

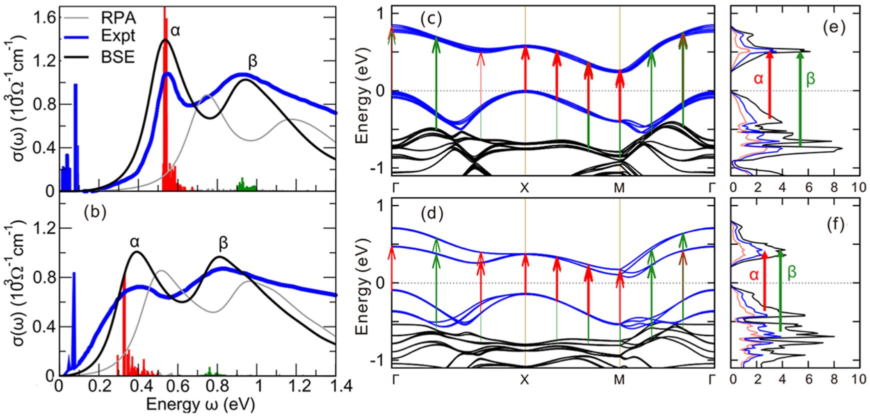

Figure 2. Experimental and calculated optical conductivity spectra $\sigma(\omega)$ of (a) Sr_2IrO_4 and (b) $Sr_3Ir_2O_7$. The gray vertical lines represent the oscillator strength whose contributions to α and β peaks are highlighted in red and blue colors, respectively. (c, d) *GW* band structure. (e, f) *GW* total density of states. The red and blue arrows in (c, d) represent the dominant interband transitions for the α and β peaks, respectively. The width of the arrows denotes the normalized amplitude of BSE eigenvectors $|X^{\Lambda}_{cv\mathbf{k}}|$. Adapted from ref 17.

$$S_{\Lambda} = \mathbf{Tr}\left[\left\{\sum_{\mathbf{k}} w_{\mathbf{k}} \sum_{v,c} \langle \psi_{c\mathbf{k}}|e^{i\mathbf{q}\cdot\mathbf{r}}|\psi_{v\mathbf{k}}\rangle X^{\Lambda}_{cv\mathbf{k}}\right\} \times \{c.\ c.\}\right] \quad (3)$$

In the last two equations, Ω_{Λ} and X^{Λ} are BSE eigenvalues and eigenvectors, respectively, V is the bare interaction, η is a positive infinitesimal, and $w_{\mathbf{k}}$ are the k-point weights, while $\psi_{v\mathbf{k}}$ and $\psi_{c\mathbf{k}}$ refer to occupied and unoccupied DFT(+U) wave functions, respectively.

With these prescriptions, excellent optical properties are obtained for the challenging spin−orbit coupled Dirac-Mott properties of Sr_2IrO_4 and $Sr_3Ir_2O_7$,[17] as shown in Figure 2. Note that step 3 is rather expensive and does not scale favorably with the number of k points. Considering that the calculation of BSE spectra requires many k points to reach a good level of convergence, it can be useful to adopt an analytical treatment of the screening as input in the BSE run (step 4):

$$\varepsilon^{-1}_{\mathbf{G},\mathbf{G}}(\mathbf{q}) = \varepsilon^{-1}_{\infty} + (1 - \varepsilon^{-1}_{\infty})\left[1 - \exp\left(-\frac{|\mathbf{q} + \mathbf{G}|^2}{4\lambda^2}\right)\right] \quad (4)$$

where ε_{∞} is the static ion-clamped dielectric function in the long-wave limit, and the screening length parameter λ is derived by fitting the screening ε^{-1} at small wave vectors with respect to $|\mathbf{q} + \mathbf{G}|$ with $\mathbf{q}$ and $\mathbf{G}$ being the wave vector and lattice vector of the reciprocal cell, respectively.[17]

2.4. Outlook. In conclusion, a set of state-of-the-art first-principles schemes have been briefly scrutinized; these are capable to deliver a good estimation of band gaps, not only for standard semiconductors but also for complex oxides with different electronic configurations, magnetic orderings, structural characteristics, and spin−orbit coupling strength. These methods, in particular, GW and BSE, are computationally very demanding, and much care must be taken in setting up the computational protocol. As future challenges, it would be desirable and useful (i) to find common standards for the automation of these complex sequences of simulations (streamline workflows), (ii) to build a high-quality beyond-DFT materials database ("Quantum Materials Repository") and, possibly, (iii) to envision smart ways to accelerate the calculations without loss of accuracy (machine learning techniques). This would facilitate a paradigmatic shift in the materials modeling community from massively DFT-based calculations to beyond-DFT schemes, which would be beneficial for the quality and accuracy of the results and therefore for the prediction and understanding of material-specific functionalities.

3. DATA-DRIVEN MATERIALS SCIENCE: BUILDING MAPS OF MATERIALS PROPERTIES

3.1. Descriptors in Materials Science. High-performance computing (HPC) is used for the search and design of novel functional materials with improved functionalities. According to the Springer Materials database,[19] ~250 000 inorganic materials, including stable and metastable phases, are known to exist. Unfortunately, even somewhat basic properties—such as elastic constants, electrical and thermal conductivity, and similar—are systematically known only for very few of them. Computational high-throughput initiatives like Materials Project,[20] AFLOW,[21] and OQMD[22] have collected information on hundreds of thousands of possible materials and made them available in open-access databases. However, while electronic structure calculations provide a wealth of information, the majority of these data are not efficiently used.

Recently, a manifesto[23] on how scientific data should be handled has been proposed: It goes under the acronym FAIR, which stands for findable, accessible, interoperable, and reusable/repurposable. The recently established Novel Materials Discovery (NOMAD) Laboratory[24,25] already complies to the FAIR principles. This is made possible by the NOMAD Repository & Archive, as of end of 2018 containing more than 50 000 000 open-access single-point calculations of millions of different chemical compositions and atomic structures, mainly bulk materials. These include also calculations from the above-mentioned databases and more. For all the calculations, original input and output files are stored in the Repository, and a code-independent representation of all calculations' data is accessible in the Archive, thanks to a remapping of the raw data into a hierarchical metadata framework.[24]

It is easy to realize that the number of possible stable and metastable materials is to all practical purposes infinite. This suggests that novel functional materials with superior properties for any conceivable application should exist but are not yet known. High-throughput scanning of the compositional and structural materials space may not be an efficient approach when used with accurate electronic-structure methods, because the latter are computationally demanding in terms of CPU/GPU hours.

A promising alternative approach is to construct models almost as accurate as reliable electronic-structure methods but running at a fraction of the cost by means of learning algorithms. This is the realm of artificial intelligence or (big-)data analytics that is data mining, machine/statistical learning, deep learning, compressed sensing, and others. In the past 10 years, more and more such approaches have been developed and applied to the wealth of materials-science data.[26−37] The first blind-test, crowd-sourced competition for the machine learning of properties from materials-science data—the NOMAD 2018 Kaggle competition[38]—has been a recent turning point toward widespread acceptance of good-practice protocols in data-driven materials science. Besides, it confirmed (Gaussian) kernel methods or, alternatively, the similar Gaussian-process regression, artificial neural networks, and tree-regression methods as the most popular and versatile artificial-intelligence approaches.[38]

In all the cited works, the crucial step is the identification of *descriptors* that capture the underlying mechanism of a given material's property or function and are the numerical input for the machine-learning model. The descriptors are carefully designed by the researcher, via imposing known physical symmetries and constraints. Alternatively, the descriptors can be learned from the data; more precisely, the best descriptors can be identified among a possibly immense set of candidates by exploiting a signal-analysis technique known as compressed-sensing (CS).[38]

3.2. Compressed Sensing. The compressed sensing (CS) approach reconstructs a high-quality "signal", starting from a sparse set of "observations".[40,41] Mathematically, given a set of samples measured incoherently ($\boldsymbol{P}$) CS finds the sparse solution ($\boldsymbol{c}$) of an undetermined system of linear equations $\boldsymbol{Dc} = \boldsymbol{P}$, where $\boldsymbol{D}$ is the *sensing matrix* with the number of columns much larger than the number of rows. The recasting of CS into materials-science challenges[39,42] starts from a set of materials (m_i) with observable properties listed in vector $\boldsymbol{P}_i$ and a possibly immense list of test features d_j, which form the features space. The projection of each i-material into the j-feature is the i,j component of the sensing matrix $\boldsymbol{D}$. The sparse solution of arg min$_c$ ($\|\boldsymbol{P} - \boldsymbol{Dc}\|_2{}^2 + \lambda\|\boldsymbol{c}\|_0$), where $\|\boldsymbol{c}\|_0$ is the improper norm of $\boldsymbol{c}$ (i.e., its number of nonzero components), gives the optimum Ω-dimensional descriptor, that is, the set of features "singled out" by the Ω nonzero components of the solution vector $\boldsymbol{c}$. The first term in the minimized expression is a familiar mean square error, as in least-squares regression; the second term is known as regularization. In this case, a "penalty" is paid for every nonzero component of $\boldsymbol{c}$. Effectively, CS performs a *dimensionality reduction* from the large input features space to the selected low-dimensional descriptor. Differently from most dimensionality-reduction schemes,[43] CS provides an "inspectable" solution, in the sense that the components of the selected descriptor are among the input features.

The sure independence screening and sparsifying operator (SISSO)[44] is a recently developed CS-based method, designed for identifying low-dimensional descriptors for material properties. It is an iterative scheme that combines the sure independence screening scheme (SIS)[45] for dimensionality reduction of huge features space and the sparsifying operators (SO) for finding sparse solutions. SISSO improves the results over the conventional CS methods, such as the linear absolute shrinkage and selection operator (LASSO)[39,42,46] and greedy algorithms,[47,48] when features are correlated, and can efficiently manage immense features spaces.

For applying SISSO, a feature space Φ_q is constructed by starting from a set of primary features and a set of unary and binary operators, such as +, −, exp, $\sqrt{\ }$, etc. The features are then iteratively combined with the operators, where at each iteration each feature, or pair of features, is exhaustively combined with each unary/binary operator, with the constraint that sums and differences are taken only among homogeneous quantities. The index q in Φ_q counts how many such iterations were performed. The primary features are typically *atomic properties* (e.g., ionization potential, radius of s or p valence orbital, etc.) and *compounds properties* (e.g., formation energy of dimers, volume of the unit cell in a given crystal structure, average coordination, ...)[44]. Φ_q contains features in terms of mathematical expressions; when the values of the features are determined for each material m_i, the matrix $\boldsymbol{D}$ is constructed. The *atomic properties* are repurposable and therefore can be used for many descriptors and model learning. For easier reference and reusability, the atomic features used in this work and other related works[39,42,44,49] can be accessed online at the NOMAD Analytics Toolkit: https://analytics-toolkit.nomad-coe.eu.[50] A tutorial[51] shows how to access these quantities and use them in a python notebook.

Next, a sketch of the SISSO approach for one important class of problems in materials science will follow: constructing materials-properties maps. Then, one application of the method is shown.

3.3. SISSO for Building Materials-Properties Maps. A materials-property map (Figure 3) is a low-dimensional representation of the materials space, where each material is represented by means of a convenient descriptor. The components of the descriptor are the coordinates in the low-dimensional representation, such that all materials sharing a certain property (e.g., being metal or topological insulator) are located in the same convex hull. In a useful map, hulls containing materials with exclusive properties (e.g., metals vs insulators) do not overlap.

The mathematical formulation of SISSO for classification[44] substitutes a measure of overlap between convex hulls to the usual mean square error adopted in continuous problems.[44] For a property with M categories, the norm for classification is defined as

$$\hat{\boldsymbol{c}} = \arg\min_{\boldsymbol{c}} \left(\sum_{I=1}^{M-1} \sum_{J=I+1}^{M} O_{IJ}(\boldsymbol{D}, \boldsymbol{c}) + \lambda \|c\|_0 \right) \qquad (5)$$

where $O_{IJ}(\boldsymbol{D}, \boldsymbol{c})$ is the number of data in the overlap region between the I and J domains, $\boldsymbol{c}$ is a vector with 0 or 1 elements, so that a feature k (the kth column of $\boldsymbol{D}$) is selected (deselected) when $c_k = 1(0)$, and λ is a parameter controlling the number of nonzero elements in $\boldsymbol{c}$. O_{IJ} depends on ($\boldsymbol{D}$, $\boldsymbol{c}$) in the sense that the nonzero values of $\boldsymbol{c}$ select features from $\boldsymbol{D}$ that determine the coordinates of the data and the shape of the convex hulls.

The SISSO algorithm provides an efficient solution to eq 5 also when the number of columns of $\boldsymbol{D}$ (size of the features space) is immense.[44] SISSO has been successfully applied to identify descriptors for relevant materials-science properties.[44,52,49,53] As a showcase application of SISSO, we

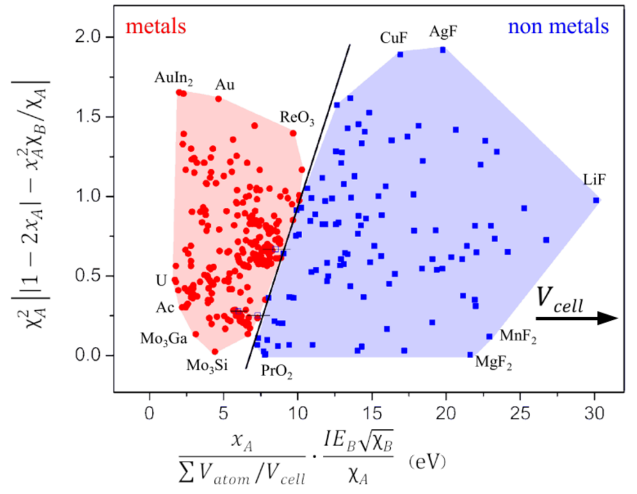

Figure 3. Material-property map for the metal/nonmetal classification (see ref 44 for the data and a more detailed discussions). The axes are the components of the descriptor, as found by SISSO, by imposing that materials classified as metal are represented in a (convex) region that does not overlap with the region containing materials classified as nonmetals. In the descriptor, x is the atomic fraction, IE is the ionization energy, χ is the electronegativity, V_{atom} is the volume of a sphere with radius equal to the covalent radius of the element, and V_{cell} is the volume of the unit cell of the considered material.[44] The red circles/blue squares are the training metal/nonmetal materials.

summarize here the recently introduced new descriptor for the prediction of stable ABX_3 perovskites.[49]

3.3.1. Stability Prediction of ABX_3 Perovskites. Perovskite materials possess exceptional properties for a variety of applications such as electrocatalysis, proton conduction, ferroelectrics, battery materials, as well as photovoltaics and optoelectronics.[54−59] ABX_3 perovskite crystal structures are defined as a network of corner-sharing BX_6 octahedra surrounding a larger A-site cation ($r_A > r_B$).

While the A and B cations can span the periodic table, the X anion is typically a chalcogen or halogen. Distortions from the cubic structure can arise from size-mismatch of the cations and anion, which results in additional perovskite structures and nonperovskite structures. The B cation can also be replaced by two different ions resulting in a double perovskite with chemical formula $A_2B'B''X_6$.

Predicting the stability of ABX_3 and $A_2B'B''X_6$ compounds remains a longstanding challenge for the discovery of new functional materials. Most of the approaches that address this challenge are computationally demanding, limiting their use to a small set of materials.[60−63] Conversely, descriptor-based approaches enable high-throughput screening applications, because they provide rapid estimates of material properties.[64] A notable example of "human-learned" descriptor is the Goldschmidt tolerance factor[65]

$$t = \frac{r_A + r_X}{\sqrt{2}\,(r_B + r_X)} \tag{6}$$

introduced in 1926 and since then used extensively to predict the stability of ABX_3 perovskites based only on the ionic radii (r_i) of each ion ($i = A, B, X$). The prediction accuracy of t is not very high, especially for compounds containing heavier halides.[66] Considering a data set of 576 ABX_3 experimentally characterized material compositions,[67−69] the overall prediction accuracy of t is 74%. Using the same 576 ABX_3 materials, Bartel et al.[49] set up SISSO by starting from r_i and the oxidation numbers (ν_i). Note that, in eq 6, ν_i are implicitly used to determine r_i. Out of a constructed feature space of 3 × 10^9 features (up to the third iteration of feature/operator combination), the following one-dimensional (1D) descriptor was identified:

$$\tau = \frac{r_X}{r_B} - \nu_A \left(\nu_A - \frac{r_A/r_B}{\ln r_A/r_B} \right) \tag{7}$$

This new tolerance factor (τ) shows a prediction accuracy of 94% and nearly uniform performance across the five anions evaluated (X = O^{2-}, F^-, Cl^-, Br^-, I^-). Like t, τ requires only the chemical composition, allowing the tolerance factor to be agnostic to the many structures that are considered perovskites. In addition, τ provides a monotonic estimate of the probability that a material is stable in the perovskite structure (Figure 4). The accurate and probabilistic nature of τ, as well as its generalizability over a broad range of ABX_3 and $A_2B'B''X_6$ perovskites [with $r_B = (r_{B'} + r_{B''})/2$ in eq 7] allows for new physical insights into the stability of the perovskite structure. As a direct result, Bartel et al. report the prediction of 23 314 new double-perovskite oxides and halides.[49]

The equations found by SISSO are not then necessarily unique, and all components of the descriptors may change at each added dimension. This reflects the approximate nature of the equations and the unavoidable relationships among features. In words, one or more primary features may be accurately described by nonlinear functions of a subset of the remaining features. It is also noted that the mathematical constraints imposed in order to obtain the minimally overlapping convex hulls are very flexible but not complete; that is, the found descriptor → property relationship is intrinsically approximate.

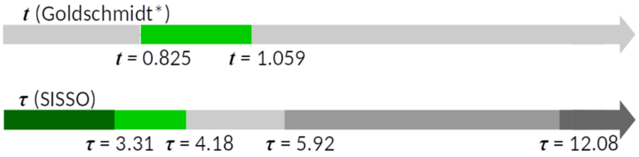

Figure 4. 1D maps for Goldschmidt t vs the newly proposed τ for perovskite-stability prediction. The green (gray) areas are the domains of predicted stability (instability) of perovskites. The boundaries of Goldschmidt's t were trained via a decision-tree classifier over the same data set used for SISSO, hence, the asterisk. In the case of τ, the darker green and gray areas are regions of 100% prediction accuracy. So, if for a material τ is smaller than 3.31 or larger than 12.08, its classification is certain. At τ = 4.18, the predicted probability that a material is a perovskite is 50%, and the probability to be perovskite smoothly decreases from left to right.

3.4. The NOMAD Analytics Toolkit. Artificial intelligence approaches like SISSO are promising tools that could become part of the modern materials scientist's set of skills. In this respect, it is fundamental for any researcher adopting such methods to share not only the data used for training the algorithms but also the (implemented) learning algorithm themselves. This has both educational/tutorial purposes and the merit of improving scientific reproducibility. Besides maintaining a large (and growing) Repository & Archive, the NOMAD Laboratory also provides the infrastructure to share data-analytic tools, in terms of python (or other languages) notebooks. By logging in at https://analytics-toolkit.nomad-coe.eu, users can find tutorial notebooks, for instance, introducing the CS method and allowing for the reproduction of published results such as those presented in refs 35, 39, 42, 44, 49, 52, and more.

3.5. Outlook. Compressed-sensing-based descriptor identification is a promising approach for the artificial-intelligence-assisted determination of maps of materials properties. In particular, SISSO is a powerful tool for the identification of descriptors starting from a huge number of candidates. However, this approach is currently limited to scalar features. This seems to be not a severe limitation in cases where the chemical composition of a material corresponds to a well-defined structure, including crystal symmetry and atomic arrangement. In this case, suitable descriptors depending on properties of free atoms are readily found. When polymorphism is present, the atomic (local) environment appears to be a necessary input, but currently the approach described in this section lacks a systematic strategy to construct environment-dependent features of increasing complexity, to be used as candidates in the feature space.

4. IDENTIFYING ERROR IN MACHINE LEARNING MODELS

The design of new materials has long relied on DFT, molecular dynamics, phase field calculations, and more. While these approaches are very useful, they are also costly in terms of computational resources and time, limiting their utility. In the past decade, we have seen a surge in interest in applying machine learning (ML) techniques to help address these challenges.[70−72] For example, fewer computations need to be performed if an ML algorithm is able to prescreen compounds of interest.[73,74]

Despite increasingly broad acceptance of ML in the discovery of new materials, there remain common and often valid criticisms,[75] which include:

(i) Necessity of data. Is there sufficient data in the literature, and how do we organize it in a way that is useful?
(ii) ML algorithms are a black box. As such they lack the ability to provide physical insight from a mechanistic perspective.
(iii) Suspicions about the ability to extrapolate beyond the training data.
(iv) We often do not consider the error, or uncertainty, associated with model predictions.
(v) Reported error does not represent the actual ability to predict targets due to overfitting.
(vi) Given relatively recent adoption of data science into material science, there remain numerous instances of bad data practices.

The ML community has begun to identify and address these issues in a number of ways.[76,77] Next, a tool to allow materials research practitioners to leverage their chemical knowledge to identify model error is explored.

4.1. An Interactive Tool to Visualize Model Error and Chemistry. The error identification in ML is accomplished by providing an interactive tool to visualize error and chemistry. In our experience, materials researchers want to rely on their own chemical intuition as they address the following questions:

(a) Do I have enough data for meaningful learning?
(b) Do my data provide the required diversity to predict across a variety of chemistries?
(c) Is my data set skewed toward certain types of chemistry?
(d) Is my model error artificially low due to overfitting?

At the heart of these questions are two key problems: (i) understanding the error associated with sparse representation of chemical classes, and (ii) recognizing the extent of chemical clustering and how clustering may effect performance. As we seek to understand the role of chemistry in model error, it is best described with a model system.

Consider this preliminary tool[78] built using a model that predicts experimental band gap. The model was trained on 2483 compounds where experimental band gap was known, and the details of the model are reported elsewhere.[79] The first thing that this tool provides is a periodic table (Figure 5), where elemental prevalence in the data set is visualized using a heat map. Sorting the data by elements allows us to not only express elemental prevalence but also demonstrate the error versus number of entries. The overall model may look acceptable, but on closer investigation one can see that certain classes sufferer from systematic error.

Figure 6a provides evidence whether the error in these classes could be reduced by obtaining additional entries in this class. In other words, additional data from compounds containing these elements should be gathered to improve accuracy. This same periodic table could be toggled to have the heat map represent the absolute error for compounds containing each element. Moreover, hovering over and clicking on individual elements could then provide element-specific information.

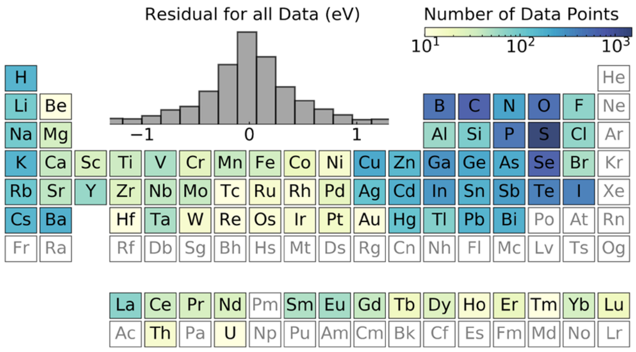

Figure 5. Interactive periodic table allows for quick and efficient exploration of chemical space. The tool is described in detail in ref 78. Such tool will also be generalizable for any machine learning model where chemistries are being explored, not just for bandgap.

In Figure 6b the distribution of residual values for vanadium are shown. It is also possible to display information regarding the average band gap, the variance in band gap, the percent error, or even things like feature values. Extending this approach to include AND/OR logic (formula contains: O, F, and/or Al) is also possible and would allow for a more nuanced analysis. For example, the residual error associated with hydroxides or fluorooxides can be considered as opposed to the broader class of oxides. This allows users to visualize if the error is a function of trends from the periodic table—which chemists already know and understand such as bonding, electronegativity, size, screening, etc.

Interacting with the periodic table to select elements can also allow for a better analysis of residual plots. The current practice of examining outliers that contribute large errors could instead be replaced by examining whole classes of materials at a

DOI: 10.1021/acs.inorgchem.9b01785
Inorg. Chem. 2019, 58, 14939−14980

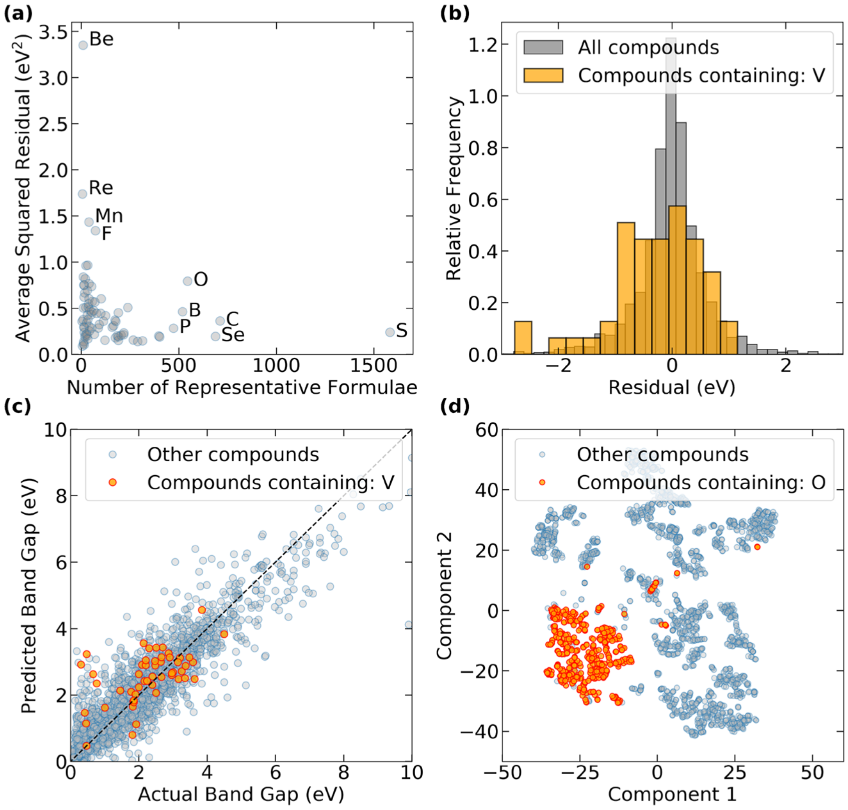

Figure 6. (a) Error decreases as more representative data become available. (b) Residual values allow to explore whether there are patterns in the error associated with compounds containing specific elements. (c) The actual vs predicted values for all experimental band gap values. Compounds containing vanadium highlighted in orange. (d) Extreme example of grouping for compounds containing oxygen on the t-SNE.

time and seeing where their error lies compared to the average model residual error. This can be seen in Figure 6c, where the actual versus predicted band gap of compounds containing vanadium is shown in orange color, while the remaining compounds are shown in blue. This visualization allows a user to easily observe an overprediction trend in this class of materials. This observation is confirmed when the residual error histogram for vanadium versus all compounds is compared in Figure 6b. Furthermore, selecting elements from an interactive periodic table can also provide information about clustering. The dimensionality reduction technique, t-distributed stochastic neighbor embedding (t-SNE),[80] has been used to cluster data together, but determining whether clusters are grouped by chemistry is not straightforward.[81] Users will have to test point-by-point as they seek to establish chemical trends in the clusters.

Visualization of compounds containing specific elements allows for easy identification of which clusters belong to specific chemistries and which chemistries do not cluster. An example is shown in Figure 6d, where the t-SNE plot clearly shows clustering, and one cluster is identified as primarily containing oxides. Is it possible to anticipate that future ML by materials researchers will utilize information from elemental t-SNE diagrams as they select cross-validation training sets to prevent overfitting due to interpolation in overly similar data sets.[81]

4.2. Outlook. As researchers embrace the philosophy of data-driven science, we expect great progress to be made in the materials front. In particular, open-source projects revolving around sharing of materials data could revolutionize how we think about the field of materials science and engineering. Within this paradigm, the training and sharing of ML-based tools has already become popular for the purpose of predicting materials properties. Although this is an exciting prospect, we should be cautious that the data and modeling efforts give appropriate answers. In particular, the types of materials included in these modeling efforts are often skewed toward specific chemistries. This can lead to a systematic error that is otherwise not accounted for in the reported model accuracies. The increased use of data visualization techniques will allow us to probe these models from a domain-driven perspective. Using both materials knowledge and data visualization techniques, we can provide researchers with a strong intuitive feel for how a model performs while also providing a way to visualize and identify common problems that occur in the modeling process.

5. ACCELERATED AB INITIO MOLECULAR DYNAMICS APPLIED TO THE SIMULATION OF HETEROGENEOUS CATALYSIS

The experimental identification of intermediates and surface sites under reaction conditions is challenging. To this purpose, computational approaches based on quantum-chemical calculations have become a fundamental tool to understand reaction mechanisms and investigate active surface sites in heterogeneous catalysis.[82,83] The establishment of DFT as an efficient method to solve the electronic structure problem[84] combined with the development of high-performance computing facilities has fostered the investigation of reaction mechanisms occurring on the solid surfaces.

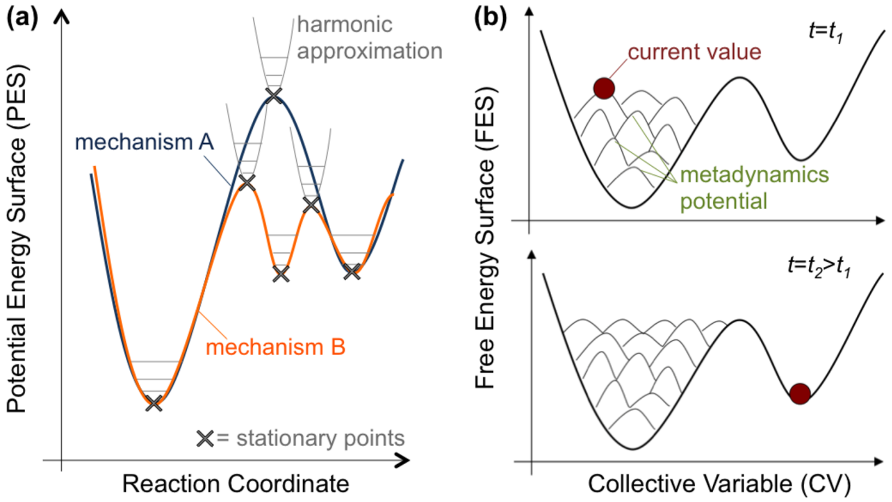

Figure 7. (a) Common approach to evaluate surface reaction mechanisms by DFT calculations: focus on locally harmonic stationary points of PESs corresponding to mechanisms assumed beforehand. (b) AIMD/MetaD approach for reaction mechanism exploration. The history-dependent potential (represented by the Gaussian hills on the FESs in (b)) forces the system to escape from local minima on the FES defined by a set of CVs as the simulation proceeds in time (e.g., t_1 and t_2 shown in (b)).

The evaluation of reaction mechanisms on surfaces based on DFT calculations (Figure 7a) generally consists of (i) the postulation of possible pathways, that is, sequences of bond-forming and -breaking elementary steps that transform reactants into products; (ii) the geometry optimization of selected initial guesses, locating stationary points of the potential energy surfaces (PESs) and calculating the (electronic) energy of minima and transition states along each postulated reaction pathway (at 0 K); and (iii) the estimation of entropic contributions via partition functions, often assuming that the stationary points of the PES are locally harmonic.[85] These procedures allow to obtain the free energy surfaces (FESs) at the reaction temperature. These FESs are then used to discuss the relevance of the different possible reaction mechanisms. In spite of the popularity of such an approach, two severe shortcomings may be associated with it. First, the surface of the catalyst can be highly covered by chemisorbed species under reaction conditions (formation of adlayers), for instance, during the industrially relevant Fischer−Tropsch synthesis and the methanation reactions, among other reactions.[86] For these cases, the energies of reaction intermediates and transition states can be influenced by complex adsorbate−adsorbate interactions. Second, the evaluation of adsorbate entropy by the harmonic oscillator model may be oversimplified when anharmonic,[87−89] translational/rotational,[90−94] or configurational[95] degrees of freedom are relevant for the evaluation of the free energy of minima and transition states. Aside from the above-mentioned standard approaches, it is worth mentioning a recent computational method, namely, *Normal-Modes Transition Approximation*, which rephrases the search of transition paths in terms of eigendisplacements of the dynamical matrix of the system.[96] Such method allows to identify possible reaction paths from the only knowledge of the phonon modes of the stable geometry, showing how to control reaction barriers through a fine-tuning of the eigenfrequencies of the system.

In this section, modeling approaches to evaluate reaction mechanisms in heterogeneous catalysis are based on molecular dynamics (MD). This technique has recently emerged as a promising alternative to overcome the limitations of the PES-based approaches.[97,99]

5.1. Ab Initio Molecular Dynamics. Ab initio molecular dynamics (AIMD)[100,101] is the molecular dynamics method of choice for the study of reaction mechanisms in catalysis. The electronic structure is explicitly included (e.g., at DFT level), allowing the description of bond-breaking and -forming events. During MD simulations, starting from a given initial structure, nuclei positions and velocities are evolved in time subjected to determined thermodynamic boundary conditions. The collection of visited states at finite temperatures (trajectory) can then be used for the calculation of free energy differences. Compared to the common evaluation of discrete points of PESs, the free energies obtained from MD simulations include additional contributions that are fundamental to overcome the limitations of modeling surface reactions on adlayers. The calculation is performed on a large number of configurations explored during the simulation at finite temperature—and not only on selected geometry-optimized structures at 0 K—which increases the chances of capturing relevant adsorbate−adsorbate interactions that affect the energetics of surface reaction mechanisms. Furthermore, the free energy is not calculated using a posteriori correction to the PES, but it is instead obtained on-the-fly during the simulation. This means that the partition functions simultaneously include translational, rotational, and (anharmonic) vibrational degrees of freedom. Despite such benefits, the evaluation of free energy differences by AIMD is computationally demanding. In particular, surface reactions involving energy barriers much higher than thermal energy require relatively long trajectories resulting in prohibitive calculations. This problem can be avoided by coupling the AIMD with the Metadynamics (MetaD) technique.[99,102−106]

5.2. Metadynamics. MetaD consists of the exploration of the phase space using a reduced configurational space defined by a set of selected reaction coordinates, called collective variables (CVs). At regular time intervals during the AIMD simulation, a history-dependent potential (e.g., Gaussian functions) is applied forcing the system to escape from (local) already explored minima on the reduced phase space

DOI: 10.1021/acs.inorgchem.9b01785
Inorg. Chem. 2019, 58, 14939−14980

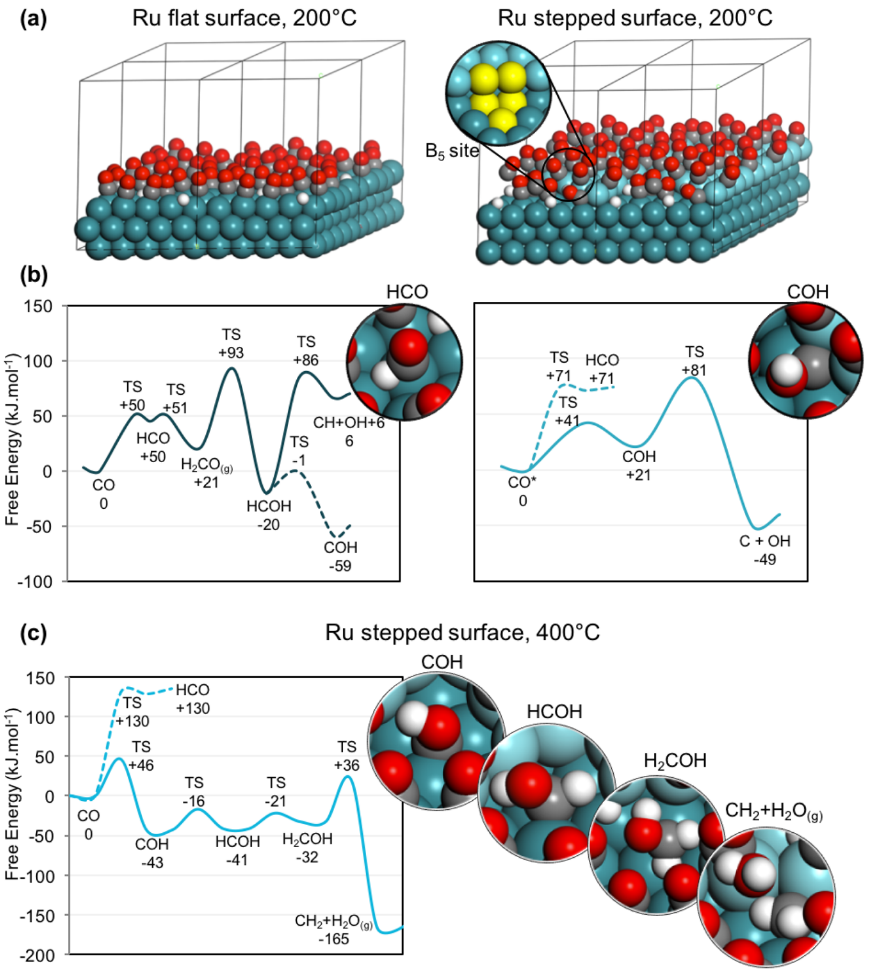

Figure 8. (a) CO activation at Fischer−Tropsch reaction conditions (200 °C) modeled by AIMD/MetaD simulations: Ru flat and stepped model surfaces (containing step-edge sites shown in the inset) covered with CO/H adlayers and (b) FESs for observed mechanisms: HCO vs COH intermediates on the flat and stepped surfaces, respectively (shown in the insets). (c) CO activation at methanation reaction conditions (400 °C) modeled by AIMD/MetaD simulations: FES for mechanism identified on the stepped Ru surface involving multiple hydrogen transfers and water elimination (reaction intermediates shown in the insets). Ru, C, O, and H atoms are shown in blue, gray, red, and white, respectively. The Ru atoms of the top layer in the Ru stepped surface are shown in lighter blue. The simulation cell is shown in black (a 2 × 2 supercell is represented). (a, b) Adapted from ref 97; (c) adapted from ref 99.

(Figure 7b). For sufficiently large simulation times, the applied MetaD potential approximates the FES, and the meta-trajectory follows the minimum free energy pathway. The use of MetaD therefore replaces the need to postulate, beforehand, the detailed sequence of elementary steps. The combination of AIMD with MetaD has been used to unravel the mechanisms of catalytic processes on molecular systems[107] as well as on oxide-supported clusters and metal surfaces.[97,108−110]

5.3. A Case Study: The Fischer−Tropsch Synthesis.

The Fischer−Tropsch synthesis (see eq 8) with $n > 1$, which converts syngas (CO/H_2 mixture) to hydrocarbons, is an example of complex reaction taking place at high adsorbate coverage, whose mechanistic understanding has benefited from the use of AIMD (in this case Born−Oppenheimer MD[100,101]) coupled with MetaD simulations at 200 °C.[97,98] By using ruthenium flat and stepped surface models covered with coadsorbed CO and H species (Figure 8a), the effect of adlayer on the favored reaction mechanisms and the active sites for CO activation, the highly debated key step of the reaction, was addressed.

$$n\mathrm{CO} + (2n + 1)\mathrm{H}_2 \leftrightarrows \mathrm{C}_n\mathrm{H}_{(2n+2)} + n\mathrm{H}_2\mathrm{O}$$

$$\Delta H^\circ_{298} = -167\ \mathrm{kJ/mol} \tag{8}$$

AIMD/MetaD simulations were performed by using a set of three CVs, namely, C−O distance, C−H coordination number, and O−H coordination number. The simulations allowed to capture, simultaneously, several mechanisms involving zero or several hydrogen transfer steps to both C and O ends of the adsorbed CO molecule, in any order, before the actual elementary step of C−O cleavage. It was found that the CO activation mechanism via the formyl intermediate (HCO) is the most likely one on the flat surfaces (Figure 8b), in line with previous proposals.[111] Conversely, in the case of the stepped surface, hydrogen-assisted routes via the COH intermediate are the most favored ones (Figure 8b).[112] This is because adsorbed H preferentially bound to step-edges can be easily transferred to carbon monoxide O end at high coverages. The comparison of the reaction intermediates stability calculated by the evaluation of discrete points of the PES and the AIMD/MetaD approach reveals that the dynamic effects are hardly

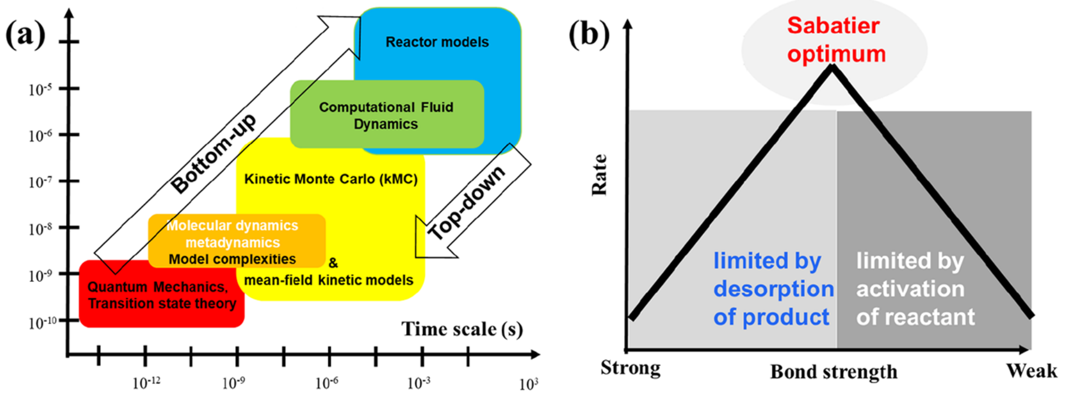

Figure 9. (a) Top-down and bottom-up catalyst development/length and time scales. (b) Sabatier principle, which states that there is an optimum “bond strength” defining the best catalyst for a given reaction (partially based on refs 120 and 147).

captured by the static approach, due to complex adsorbate−adsorbate interactions.

The methanation reaction on ruthenium (eq 8, with $n = 1$) was also studied, using the same models and methodology at a higher temperature (400 °C).[99] The simulations revealed that, in the presence of step-edges, an unusual low-energy mechanism, involving four hydrogen transfer steps and the simultaneous C−O cleavage with the formation of CH_2 species and H_2O, is available on the stepped surface (Figure 8c). This mechanism is entropy-driven, since the C−O bond activation step involves the formation of a water molecule, which readily desorbs from the surface. These results reveal how valuable can be the AIMD/MetaD approach in capturing entropy-driven mechanisms at higher temperatures. Despite the use of MetaD to accelerate the AIMD simulation, the computational effort needed for such simulations, which need the evaluation of the electronic structure at each time step of the MD run, is still high, and some of the limitations of the approach are associated with it. If on one hand the MetaD potential allows crossing of energy barriers, on the other hand the simulation time scale (in the order of ps) is not long enough to allow equilibrating of gas-phase species with the surface. This means that the coverage is fixed during the simulations and needs to be carefully determined beforehand via, for instance, ab initio thermodynamics.[113] The accuracy of FESs calculated by MetaD[103,114] depends on the shape of the biasing potential (Gaussian hill height and width) as well as on the frequency at which it is applied; there is thus a compromise between the accuracy and the length of the simulated time. Larger hill width and height applied more frequently, for instance, will enable quicker exploration of the free energy landscape but will also smear out the details of the FESs and increase the error of the simulation. Another limitation of the MetaD technique is related to the choice of CVs, since mechanisms that are not described by the chosen set cannot be accessed.

5.4. Outlook. The application of the AIMD/MetaD techniques to catalytic processes, occurring on the materials surface, shows its potential to unravel favorable reaction mechanisms in heterogeneous catalysis. Such techniques result to be particularly useful in the case of reactions that occur at high coverages, where adsorbate−adsorbate interactions modulate the preferred pathways. Nevertheless, the high cost of the simulations is still a drawback. The recent development of accurate and less resource-consuming representation of the PES by statistical methods[115] represents a promising alternative to overcome such limitation, which could enable the systematic analysis of reaction networks in heterogeneous catalysis by AIMD simulations.

6. PREDICTIVE DESCRIPTION OF CATALYTIC SYSTEMS USING MICROKINETIC MODELING

Ab initio-derived free energy landscapes embedded within kinetic and Monte Carlo models[116−130] are a recent evolution necessary to bridge the gaps between theory and experiment in catalytic systems modeling (Figure 9a). This gap can either be bridged in a top-down fashion, using parameter fitting and regression analysis, or in a bottom-up fashion, using ab initio data.[120,131]

Within the bottom-up approach, temperature and pressure gaps can be sufficiently bridged by the embedding of a computational reaction network (computational reaction kinetics) within kinetic model and/or Monte Carlo models. However, it remains challenging to make a realistic atomistic model, which should be representative enough for the studied catalyst.

Recently, ab initio-based kinetic and Monte Carlo models have demonstrated their usefulness to get insights into reaction mechanisms onto various catalyst models, such as metal nanoparticles,[132] periodic metal surfaces,[124,125,129] as well as oxides,[126,127] and even metal-oxide interfaces.[123,128,130] The computational catalyst development has frequently used simplified reaction networks by exploitation of scaling relations. These have been known in various subfields of chemistry for several decades as Brønsted relations, Evans−Polanyi relations,[133,134] and Hammett equations.[135] The computational prediction of qualitative structure−activity relationships or QSARs facilitates the development of more active new catalysts. Within the last two decades, Nørskøv and co-workers have focused on the application of DFT on metal surfaces to identify computational activity descriptors.[136−140] Plotting the logarithm of the turnover frequency in function of one or more descriptors allows the construction of one- or multidimensional “volcano-plots” (Figure 9b). A famous example of a descriptor is the N_2 dissociation energy (EN-N) in case of the NH_3 synthesis.[138,139] Besides numerous examples of energy descriptors, for example,[138,139,141,142] there are other frequently used descriptors, such as the d-band center.[136,143,144] The d-band center can, for example, be employed to rank metals for their CO dissociation potential.[145,146] By constructing scaling relations and embed-

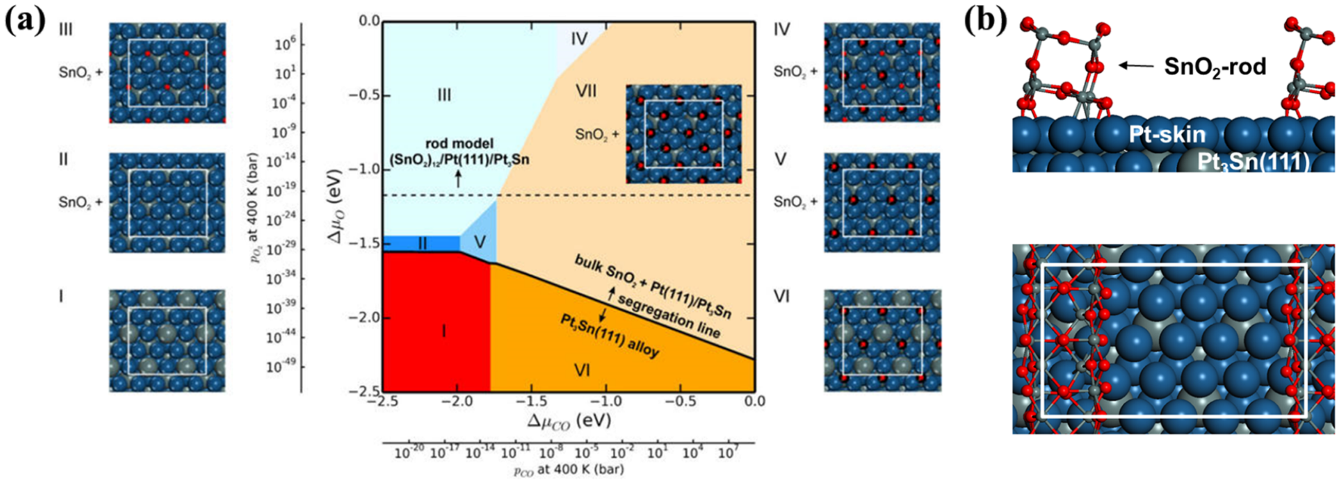

Figure 10. (a) Thermodynamic phase diagram showing the preferred phase [lowest difference in surface energy with respect to $Pt_3Sn(111)$] as a function of differences in chemical potential ($\Delta\mu_i$) for CO and O_2. The solid black line indicates segregation from a $Pt_3Sn(111)$ surface to Pt/$Pt_3Sn(111)$ and bulk SnO_2. Structural models for the phases I–VII are shown. (b) The dotted line shows the conditions, when the formation of the rod model becomes thermodynamically preferred. The surface cells are indicated by white rectangles. Atomic color codes: C in black, O in red, Sn in green, and Pt in blue (based on ref 123).

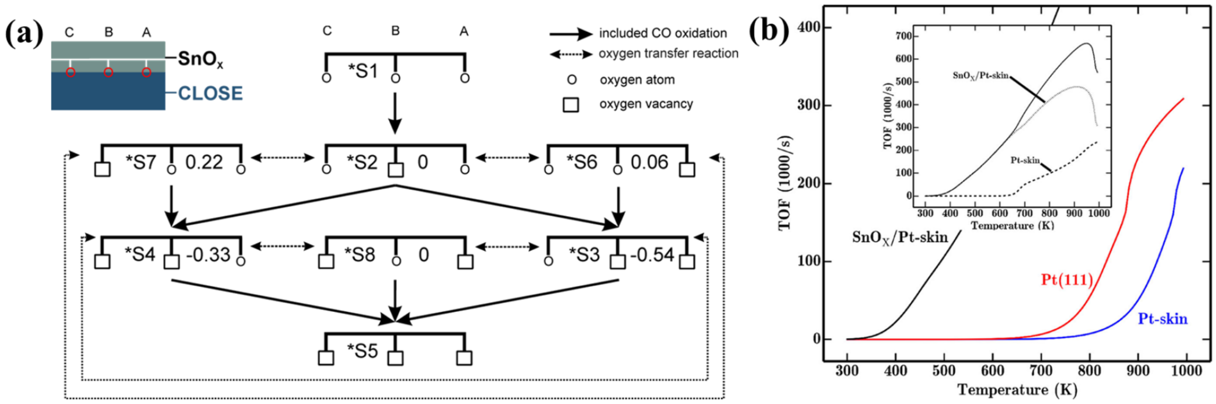

Figure 11. (a) Considered reactions for the SnO_X/metal interface model or $SnO_X/Pt(111)/Pt_3Sn$ model within the mean-field microkinetic model. The energy differences between SnO_X-states with the same number of oxygen atoms are given in electronvolts (displayed green). (b) Comparison of the TOF for Pt(111), $Pt(111)/Pt_3Sn$, and $SnO_X/Pt(111)/Pt_3Sn$ (inset). Different contributions to the total TOF for $SnO_X/Pt(111)/Pt_3Sn$. The partial pressures for CO and O_2 are 11.0 and 21.4 mbar, respectively (On the basis of ref 123).

ding these within ab initio Micro-Kinetic Models (MKM), it is possible to map the catalytic activity onto a 1D or two-dimensional (2D) descriptor space and obtain activity and selectivity maps.[140] The resulting activity maps can be viewed as a quantitative implementation of the classical Sabatier principle.[147] This screening approach is applied frequently to metal surfaces,[147,148] and it allows the selection of optimal metal alloys.

The computational screening approaches that exploit scaling relations between activation energies and reaction energies are also dependent on (i) the reaction mechanism and (ii) the atomistic model.[136−139,149] Furthermore, the simplified scaling approach still lacks complexity and is unable to describe possible catalytic interface effects and support effects, confinement effects, etc. In most cases adsorbate−adsorbate interactions on metallic systems and adsorbate pairing effects on oxides are also neglected when scaling relations are constructed. This explains why most state-of-the-art kinetic models cannot predict catalyst activities and selectivities reliably. It is thus clear that existing microkinetic models can be improved by the addition of more complexities.

6.1. Embedding Complexities within the Microkinetic Modeling on Interface Catalysts: The Case Study of CO Oxidation on PtSn.

Sometimes it happens that the classical reaction route can be circumvented by another reaction route, for example, a route taking place at a catalytic interface. Then, the computational description of interfaces becomes important, since the presence of interfaces creates new reaction mechanisms.

In recent years, a variety of atomistic models and/or computational reaction pathways have been presented describing reactions onto catalytic interfaces, for example, for CO_2 conversions[128,130,150−154] and CO oxidation.[123,155−162] While the reaction networks are studied in detail on these interface catalysts, they are frequently not included within microkinetic models, and even for developed existing ab initio kinetic models[123,128,130] there is still room to implement more complexities.

For CO oxidation on PtSn nanoparticles, the low-temperature CO oxidation activity arises from the presence of a SnO_X/Pt interface.[123] The idea that SnO_X/Pt interfaces were responsible for the catalytic activity was postulated initially by the renowned Somorjai group in 2014.[163] The likelihood to form such SnO_2/Pt interfaces can be studied via ab initio thermodynamics, by ranking different studied phases according to their most stable surface energy in function of the chemical potential ($\Delta\mu_i$) for CO and O_2 (Figure 10).

As chemical potentials are functions of temperature and pressure, it is possible to plot the corresponding pressure axis for each temperature, for example, at 400 K (Figure 10a). At regular operating conditions for CO oxidation, that is, pO_2 and $pCO > 0.01$ bar, the segregated system of a Pt-skin and SnO_2-bulk is thermodynamically more feasible compared to the bare alloy phase. However, a more likely situation is presented in Figure 10, where a bulklike SnO_2 rod is formed that is 0.72 eV/SnO_2 higher in energy compared to bulk SnO_2,[123] the dotted line in Figure 10. Different sites can be present at a SnO_2/Pt-skin interface. Therefore, a representative number of interface sites should be evaluated and included within kinetic and Monte Carlo models.

For the SnO_2 rod (Figure 10b), a reaction scheme can be constructed based on the three different possibilities into which oxygen can react with CO (A, B, and C in Figure 11a). This results in a network containing eight different states of the rod (*Si, where i is the state, Figure 11a), which can be embedded as a microkinetic model with 23 elementary reactions, accounting for regeneration steps as well as transfer steps between states of the rod with the same number of oxygen atoms.[123]

This microkinetic model for CO oxidation at the chosen SnO_2/Pt interface can then be compared with a model for CO oxidation on Pt(111) (Figure 11b). The cocatalytic role of a SnO_2 rim is clearly manifested in an enhanced activity at low temperatures. Furthermore, the interface is even found to solely contribute to the CO oxidation rate below 600 K. To make this kinetical model for CO oxidation work, several complexities need to be included: coverage-dependent adsorption energies and CO oxidation barriers. Moreover, for a mean-field microkinetic model, also a realistic determination of a representative site distribution is required (SnO_2: 12.6%, interface: 15.7%, metal: 71.7%) as well as diffusion possibilities for CO from metal to near (SnO_X/Pt interface)-sites.

6.2. Outlook. Within computational catalysis, there is a trend to validate whether the catalytic model systems are representative at operating conditions based on ab initio thermodynamics. The reaction network is closely related to the type of active sites, and the coupling of various routes within microkinetic models allows to distinguish which routes are more feasible based on rate control analysis, which is a promising technique to evaluate microkinetic and Monte Carlo methods.[164−167] The technique allows to extract the rate-controlling reaction mechanisms, that is, those that contribute most to the turnover frequency.[123,130]

The computational determination of the apparent activation barrier and reaction orders for a given reaction condition remains necessary to achieve a good comparison with the experimentally measured activation barriers and reaction orders.[126] Nevertheless, the type of active sites can vary a lot, especially within model systems describing interfaces, which means that a representative distribution of sites needs to be investigated before a correct activity picture can be constructed.

Catalyst changes during a catalytic run remain hard to describe. No models can yet describe the adsorbate restructuring of metal nanoparticles upon adsorption. Nevertheless, kinetic Monte Carlo methods have been successfully implemented to describe the aggregation of different catalyst particles as a function of temperature.[168] However, it remains a major challenge for the future to describe the restructuring based on adsorbates. For CO oxidation on metal nanoparticles, this restructuring during reaction could include a coordination number and coverage-dependent scaling of adsorption energies and barriers, as successfully implemented for nanoparticles of different shapes.[132] Summarizing, bridging the pressure and temperature gaps becomes feasible via using ab initio microkinetic models or Monte Carlo models, and implementing catalyst dynamics to bridge the materials gaps remains a major challenge for the future.

7. ATOMIC DESIGN PRINCIPLE FOR SAFER BATTERY MATERIALS

One of the main concerns with respect to high-energy batteries is safety. Li-ion batteries exhibit so-called dendrite growth[169] that can lead to short-circuits and to subsequent battery fires.[170,171] The process of dendrite growth is rather complex,[171] and the reasons for its occurrence are not fully understood yet. Interestingly, while Na-ion batteries also show dendrite growth,[172] Mg-ion batteries do not.[173] Unfortunately, existing models for dendrite growth are typically not element-specific and, therefore, are not able to explain why Li and Na exhibit dendrite growth but Mg does not.

7.1. The Dendrite Growth Problem. Growth processes require mass transport, and recently it was suggested that there might be a correlation between the height of diffusion barriers of Li, Na, and Mg and their tendency toward dendrite growth.[174] Indeed, DFT electronic structure calculations found that Mg has a diffusion barrier on its most stable surface termination that is 1 order of magnitude smaller than the corresponding diffusion barriers of Li and Na.[174] On the basis of these results, it was argued that low diffusion barriers lead to a high mobility of the deposited metal atoms so that they can easily attach to existing step edges and lead to the growth of smooth surfaces. In contrast, high diffusion barriers lead to immobile surface atoms, which are the origin of rough surfaces.

Concerning the growth environment of dendrites, it was found in Li deposition experiments that the formation of needles occurs both in an electrochemical environment as well as under vacuum conditions.[175] This indicates that the growth of Li dendrites is an inherent property of lithium itself. Moreover, it is important to note that, for the growth of smooth surfaces also the diffusion barrier across step edges, the so-called Ehrlich-Schwöbel barrier,[176,177] is critical. When metal atoms are deposited on top of an existing island, two-dimensional growth will only result if the atoms are easily able to propagate to the lower terrace. Now, the transfer from the upper to the lower terrace across the step is typically hindered by rather large barriers, as the diffusing atom has to propagate through an energetically very unfavorable low-coordinated configuration. This is illustrated in the upper right panel of Figure 12, which indicates that the diffusion process across the step in the so-called hopping mode is hindered by a large barrier.

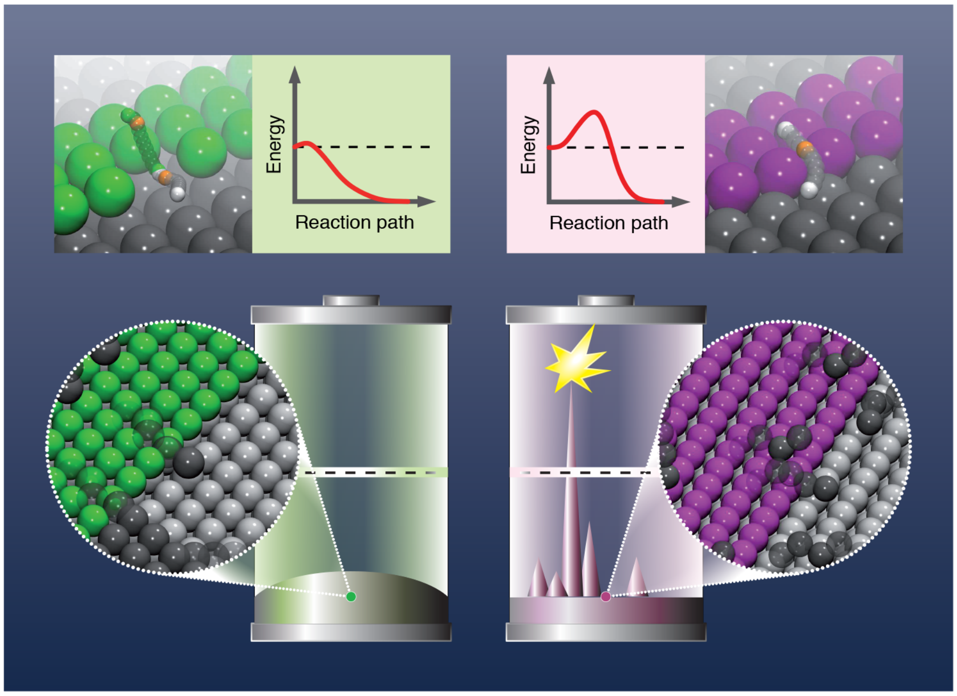

Figure 12. Illustration of the relation between diffusion barriers across step edges and the tendency toward dendrite growth in batteries. The two upper panels depict diffusion paths from the upper to the lower terrace, whereas the two lower panels illustrate the consequences of the diffusion barriers on the growth mode of the deposited metal atoms. (right panels) If diffusion from the upper to the lower terrace occurs in the hopping mode, large barriers result. Thus, the deposited metal atoms tend to stay on upper terraces and islands, leading to rough surfaces and eventually dendrite growth. (left panels) Diffusion across the step in the exchange mode is usually associated with small barriers. Thus, deposited metal atoms can easily move to the lower terraces leading to the growth of smooth flat surfaces thus prohibiting dendrite growth.

In a recent DFT study, diffusion barriers of Li, Na, and Mg across steps, as illustrated in the upper panels of Figure 12, were considered.[178] Furthermore, the study was extended to the diffusion of zinc and aluminum, which correspond to promising beyond-Li battery systems.[179−181] On the one hand, these calculations confirmed the previous findings, showing that the Li and Na body-centered cubic (bcc) metals also exhibit relatively large barriers for diffusion across steps. On the other hand, on the hexagonal close-packed (hcp) metal Mg, propagation across steps is facilitated through the exchange mechanism,[182] which is illustrated in the upper left panel of Figure 12. Instead of hopping from the upper terrace to the lower terrace across the step through a low-coordinated configuration, as shown in the upper right panel of Figure 12, the adatom from the upper terrace pushes a step atom away from the step onto the lower terrace thereby replacing it. Although in this mechanism two atoms have to move, they maintain a high coordination number along the minimum energy path making it energetically favorable. The lower panels of Figure 12 illustrate the consequences of these two different mechanisms. On the one hand, if the barriers to propagate from an upper terrace to a lower terrace are large, then atoms deposited on upper terraces or islands will remain there, which will lead to rough surfaces. These could then act as nuclei for the dendrite growth, which can cause short-circuits in the batteries and thus battery fires, as indicated in the right panels of Figure 12. If, on the other hand, the diffusion barrier to propagate to the lower terrace are rather small, then atoms deposited on the upper terraces will easily leave these upper terraces, attach to the step edges at the lower terrace, and thus lead to the growth of smooth surfaces, as illustrated in the left panels of Figure 12.

Diffusion on aluminum and zinc, whose most favorable surface terminations like Mg correspond to densely packed hexagonal structures, is also only hindered by rather small barriers. However, it is well-known that the growth of dendrites in Zn-based batteries is a serious issue.[183] Thus, on the one hand, it seems that there is an inconsistency between Al and Mg on the one side and Zn on the other side, as far as the correlation between the height of the diffusion barriers and the tendency toward dendrite growth is concerned. On the other hand, it has been shown that, in fact, the conversion of Zn to ZnO during battery discharge is critical for the occurrence of dendrites in Zn-air batteries.[180,181] Typical Zn anodes are made of loosely connected Zn powder and polymer binder. Upon discharge, resistive ZnO forms between the particles interrupting the interparticle conductivity, which has been proposed to lead to dendrite formation.[180] Zn dendrite growth can in fact been suppressed, if the Zn anode is kept metallic by using a spongelike Zn anode with interconnected continuous Zn domains.[180,181] This indicates that dendrite growth is caused by the formation of ZnO needles, that is, by the loss of metallic properties. Consequently, it does not correspond to an inherent property of Zn, as also suggested by the calculations presented above. Thus, from the theoretical considerations together with the experimental observations, a design principle for dendrite-free metal anodes can be derived, as illustrated in Figure 12. It will help to select a metal with low self-diffusion barriers, thus preventing the dendrite growth, and to maintain the metallic properties during charging and discharging.[178]

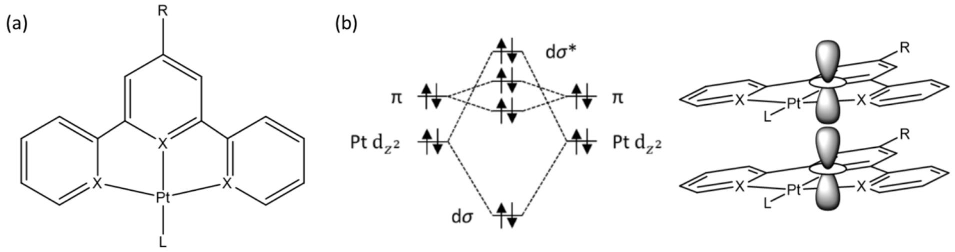

Figure 13. (a) Structure of a general Pt(II)-"pincer" complex, where the symbol X may represent N^C^N, N^N^C, or C^N^C depending on the chosen ligand skeleton. (b) Vertical stacking through supramolecular assembly or in the solid state leads to overlap of the Pt d_{z^2} orbitals, producing a new metal–metal dσ* orbital higher in energy than the pincer-based π orbitals.

7.2. Outlook. Note that, in the study described above,[178] no full theory of dendrite growth was presented. Rather a correlation has been found between a property of the considered material, the height of self-diffusion barriers, and an observable related to this material, namely, its tendency toward dendrite growth. Hence the height of the diffusion barriers can be used as a descriptor for possible dendrite growth. The concept of descriptors has been discussed in detail in Section 3 of this work. There it was shown how descriptors can be learned from gathered data of materials in a machine learning approach. Here the descriptor has been rather proposed based on physical reasoning. Independent of how the descriptor has been identified, it represents a very powerful tool for improving materials properties. A very first selection of promising materials does not need to be based on a full study of its desired properties but rather on whether the materials value of the descriptor for the desired property falls in the desired range. Furthermore, it also provides a design principle for materials with the desired properties. In the case of dendrite growth in batteries considered here, the results presented above suggest that diffusion of metal atoms deposited on the electrode should be kept facile.

Still it should be kept in mind that here no simulations of dendrite growth have been reported. Note that also for Mg the formation of dendrites during electrodeposition has been observed,[184] although it is typically assumed that Mg does not exhibit dendrite growth.[173] Hence further theoretical studies are required to clarify the connection between self-diffusion properties and the tendency toward dendrite growth,[185] taking the electrochemical environment at the interface between electrode and electrolyte more realistically into account.[186]

8. RESPONSIVE MOLECULAR SOLIDS

Molecular solids are an attractive prospect for low-to-medium temperature device applications,[187−189] because molecular design can access virtually limitless chemical diversity and can tap into the large body of knowledge on synthetic routes, structure–property relationships, supramolecular assembly and crystal engineering to match the properties to the application. Many molecular materials are amenable to solution processing, providing flexibility for incorporating them into device structures, and can meet increasingly important practical concerns such as being nontoxic and prepared by environmentally friendly chemical processes from earth-abundant elements and sustainable chemical feedstocks.

Quantum-chemical modeling has long been instrumental to understanding structure–property relationships in molecules, and advances in techniques for modeling periodic systems and the capabilities of high-performance computing (HPC) have led to an explosion in theoretical screening studies on inorganic solids.[190] The generally larger and lower-symmetry crystal structures formed by molecular solids pose a bigger challenge, but capabilities are rising to meet demand. As we will see, modeling studies play an increasingly valuable role in understanding the link between the molecular species, solid-state structure, and physical properties of functional molecular solids, and they are particularly powerful when combined with state-of-the-art experimental techniques.

Two example classes of responsive molecular solids are reviewed here, with a particular focus on highlighting the interplay between experiment and theory that has led to a fundamental understanding of their behavior and properties.

8.1. Vapochromism in Pt-"Pincer" Complexes. Cyclometalated square-planar Pt(II) complexes based around tridentate "pincer" ligands (Figure 13a) are widely studied for their tunable luminescence[191−193] and have applications as organic light-emitting diode (OLED) emitters and biological imaging agents.[187−194]

Stacking of the planar molecules through supramolecular assembly in solution or in the solid state causes the occupied Pt d_{z^2} orbitals to interact, producing a frontier molecular orbital (MO) above the π MOs on the aromatic ligand (Figure 13b).[189] This results in strong metal–metal ligand charge-transfer (MMLCT) optical absorptions that in the solid state are highly sensitive to the crystal packing.[195] The stacking also produces channels allowing small molecules to diffuse into the crystal and interact with functional groups, either on the pincer scaffold or the ancillary ligand at the fourth Pt coordination site,[196−198] which modulates the energies of the frontier orbitals, widens or narrows the energy gap, and shifts the onset of absorption.[196]

There are several examples in the literature of pincer complexes exhibiting vapochromic responses to small-molecule analytes. $[PtCl\{C_6H_2(CH_2NMe_2)_2\text{-}2,6\text{-}OH\text{-}4\}]$ undergoes a reversible solid-state reaction with SO_2 gas on the time scale of minutes, which is accompanied by a change from colorless to orange.[199] $[Pt(Me_2bzimpy)Cl]Cl\cdot 2H_2O$ ($Me_2bzimpy$ = 2,6-bis(1-methylbenzimidazol-2-yl)pyridine) changes from yellow to red on exposure to methanol, chloroform, ethanol, and acetonitrile, while the corresponding PF_6^- salt shows a selective color change from yellow to violet when exposed to acetonitrile.[195] A similar response is also shown by the dimethylformamide (DMF) solvate $[Pt(Me_2bzimpy)Cl](PF_6)\cdot DMF$.[200]

Recently, a new vapochromic system was identified based on the 1,3-di(2-pyridyl)benzene (N^C^N) pincer skeleton with R = C(O)OMe and L = CN^-.[196] Quantum-chemical calculations were used to screen potential ancillary ligands, from which the cyanide complex (Figure 14a) was selected based on (1) a high-energy Pt d_{z^2} orbital, placing the solid-state MMLCT band within the visible spectrum (Figure 13b), and (2) the high polarity and potential to form strong hydrogen bonds to guest molecules in the crystal structure. Microcrystalline thin films coated on glass or impregnated flexible polymer films showed selective subsecond responses to dry gases, water, and methanol, changing between a yellow empty structure, a red hydrate, and a blue methanolic form (Figure 14b).

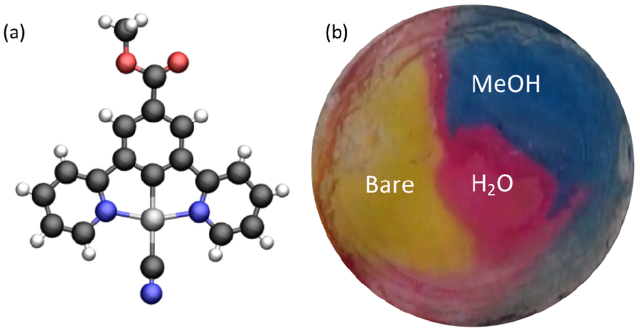

Figure 14. (a) Molecular structure of the Pt complex reported in ref 196, taken from the X-ray structure without guest molecules (CCDC: GEJTOH). (b) Image of a microcrystalline thin film of the compound showing the desolvated ("bare") yellow form and the vapochromic responses to H_2O (red) and MeOH (blue).

With synchrotron radiation, high-quality single-crystal X-ray structures of the dry (yellow) form and the hydrate and methanol solvate (red/blue) were obtained, allowing the electronic structures to be modeled. The calculations confirmed the conceptual picture in Figure 13, with the highest-occupied crystal orbitals (HOCOs) being degenerate chains of antiphase Pt d_{z^2} MOs and the lowest-unoccupied crystal orbitals (LUCOs) being pincer-based π MOs supporting strong MMLCT absorptions. By comparing the empty and solvated crystal structures, it was shown that the different patterns of H-bonding between the solvents and ancillary CN ligand changed the Pt−Pt distances and the offset between the Pt centers, modulating the degree of orbital overlap and the resulting HOCO energy. The calculations also revealed secondary interactions between LUCOs which led to a further cooperative reduction in the gap and red-shifted absorption with increasing overlap.

This study highlights the role of modeling both at the molecular-design phase and in understanding the links between solid-state structure and properties, and it also illustrates the strong synergy between experiment and theory.

8.2. Photoactivated Linkage Isomerization. Linkage isomers are coordination complexes where one or more ligands display several distinct binding modes to the metal centers.

Reports of linkage isomerism date at least as far back as the 1900s, when the color difference between the yellow and red forms of the Co complex $[Co(NH_3)_5(NO_2)]Cl_2$ was explained by the nitrite (NO_2^-) ligand coordinating to the metal through either N or O (Figure 15a). ^{18}O-Labeling experiments showed that the ONO-coordinated isomer was a kinetic product and converted to the more stable NO_2 isomer via an intramolecular rearrangement.[201] By using spectroscopic techniques, it was also shown that the isomerization occurs both in solution and in the solid state.[202] The isomerization between both forms can also be effected photochemically by irradiating at an appropriate wavelength.[203]

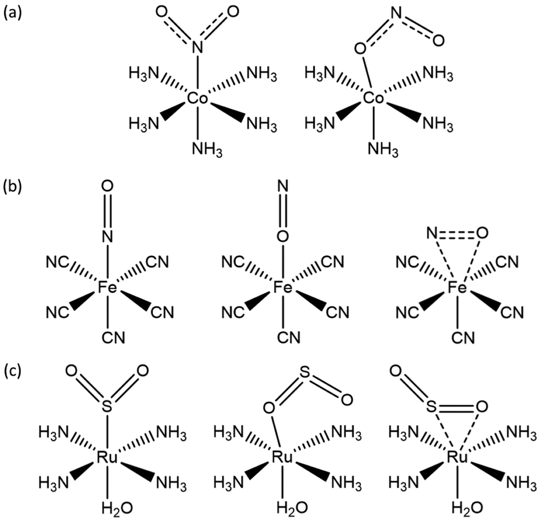

Figure 15. Examples of linkage-isomer complexes: (a) NO_2 binding modes in $[Co(NH_3)_5(NO_2)]^{2+}$; (b) NO binding modes in $[Fe(CN)_5(NO)]^{2-}$ (nitroprusside); and (c) SO_2 binding modes in $[Ru(NH_3)_4(H_2O)(SO_2)]^{2+}$.

Photoswitchable materials are of interest for a number of applications. The photoexcitation in $[Nd(dmf)_4(H_2O)_3(\mu\text{-}CN)Fe(CN)_5]\cdot H_2O$ is accompanied by a change in magnetic susceptibility, raising the possibility of optically switched and magnetically read molecular data storage.[204] Photochromic materials have also been investigated for data storage and have a wide range of other potential uses including as optical switches and photocontrolled catalysts.[205] More recently, a linkage-isomer system was identified where the photoactivated isomerization induces rotation of a neighboring benzene ring, thus acting as a transducer between solar energy and mechanical motion.[206]

In the solid state, linkage isomerism results in the movement of whole atoms and typically proceeds without loss of crystallinity, allowing the process to be followed with single-crystal X-ray diffraction. Pioneering "photocrystallography" experiments conducted by Coppens et al.,[207] in which single crystals were irradiated in situ on the diffractometer and the fractional occupations of the ground and metastable isomer(s) refined from the data, conclusively identified three NO binding modes in sodium nitroprusside $Na_2[Fe(CN)_5(NO)]\cdot 2H_2O$ (SNP; Figure 15b), and the technique has remained of huge importance to the field since then.[208]

Following the seminal work on SNP, several families of organometallic linkage isomers have been identified and characterized, including systems based on nitrite (NO_2^-),[209−211] sulfur dioxide (SO_2; Figure 15c),[206,212,213] and (di)nitrogen (N_2) ligands.[214] Key material parameters are the speed and extent of the photoconversion and the thermal stability of the metastable state. Earlier studies focused on maximizing photoconversion, and in 2009 Warren et al. demonstrated 100% conversion in $[Ni(dppe)(NO_2)Cl)]$ (dppe = 1,2-bis(diphenylphosphino)ethane) by using the bulky dppe ligand to engineer a large "reaction cavity" to facilitate the isomerization.[215] More recently, attention has turned to increasing the so-called metastable limit—the temperature above which spontaneous decay of the metastable state can be observed—toward room temperature, with a view to eventual device applications, and a limit of 240 K was recently achieved with $[Pd(Bu_4dien)(NO_2)]BPh_4$ (Bu_4dien = *N*,*N*,*N′*,*N′*-tetrabutyldiethylenetriamine, BPh_4 = tetraphenylborate).[216]

Computational modeling is regularly employed alongside experimental measurements on linkage isomers to study the energetics of the isomerization and to identify possible conversion pathways and the associated activation energies.[217,218] A recent study on the $[Ni(Et_4dien)(\eta^2\text{-O,ON})(\eta^1\text{-NO}_2)]$ linkage-isomer complex used time-dependent density-functional theory (TD-DFT) to examine the photochemical conversion between the ground-state NO_2 and metastable-state ONO binding modes.[217] Redistribution of electron density, due to low-lying metal-to-ligand charge-transfer (MLCT) absorption bands, was found to populate antibonding states and reduce the activation barrier to isomerization. However, as this particular system also shows thermal isomerization, which was studied using molecular-dynamics simulations,[217] it is also possible that strong vibronic coupling could promote isomerization by leaving the system in a vibrational "hot" ground state after de-excitation.

Another area where modeling plays an important role is in studying the isomerization kinetics. Improvements in X-ray sources and detector technology, particularly at synchrotron facilities, have made it feasible to probe the kinetics of the forward (excitation) and reverse (decay) isomerization processes with time-resolved X-ray diffraction experiments.[208,219] At low temperatures, the metastable isomer is sufficiently long-lived that the sample can be cooled, photoexcited, and warmed, and the decay can be monitored by collecting sequential single-crystal data sets. A similar procedure can be followed for the ground → metastable excitation by interspersing light pulses with data collections at temperatures below the metastable limit. At higher temperatures, the balance of excitation and decay leads to a temperature-dependent steady-state population of the metastable isomer, which can be probed by collecting structures while the sample is under continuous illumination. One could also envisage using synchrotron radiation and fast detectors to perform pump−probe X-ray diffraction experiments, although such experiments have so far been confined to measurements of carefully chosen Bragg reflections rather than complete data sets.[220]

It is typically found that the population of the metastable state $\alpha_{MS}(t)$ during excitation and decay follows Johnson-Mehl-Avrami-Kolmogorov (JMAK) kinetics:

$$\alpha_{MS} = \alpha_{MS}^{\infty} + (\alpha_{MS}^{0} - \alpha_{MS}^{\infty})e^{-kt^n} \tag{9}$$

where α_{MS}^0 and α_{MS}^∞ are the initial and final metastable state populations, respectively, k is the rate constant, and n is the Avrami exponent, which is usually close to integer and related to the dimensionality of the growth of the incipient phase by $D = 1 - n$ (i.e., $n = 4$ implies three-dimensional (3D) growth, and $n = 1$ implies homogeneous conversion throughout the bulk with no cooperativity). It is further found that the decay rate is strongly temperature-dependent and follows an Arrhenius law with an activation energy E_A, that is

$$k(T) = Ae^{-E_A/RT} \tag{10}$$

where R is the gas constant, and the prefactor A relates to the attempt frequency and is assumed to be temperature-independent. By combining the JMAK and Arrhenius equations and assuming a 100% initial population of the metastable isomer (i.e., $\alpha_{MS}^0 = 1$), an analytical expression for the half-life of the decay can be derived as[219]

$$t_{0.5}(T) = \left[-\frac{1}{A}\ln\left(\frac{1}{2}\right)e^{E_A/RT}\right]^{1/n} \tag{11}$$

Taking the $[Pd(Bu_4dien)NO_2]BPh_4$ linkage isomer studied in ref 219 as an example, the measured activation energy of 60 kJ mol^{-1} corresponds to half-lives from 10^5 s (>24 h) to 1 s over a temperature range from 200 to 300 K. The predictable variation of the metastable-state lifetime with temperature makes these systems very well-suited to the fundamental development of time-resolved spectroscopic methods that could then be adapted to other photoactive systems of interest such as photocatalysts.

8.3. Outlook. In this section, two classes of responsive materials have been discussed. Pt-pincer complexes show solid-state vapochromic responses to small-molecule analytes, and the solvent selectivity and color change can be controlled directly through the chemistry of the molecule and indirectly through the crystal packing in the solid state. Photoactivated linkage isomerism is a canonical example of a single-crystal-to-single-crystal phase transition, and the ability to study the isomerization using single-crystal X-ray diffraction and to control the lifetime of the metastable state with temperature provides the scope to develop novel time-resolved techniques for studying photochemical reactions in molecular solids.

Both examples demonstrate the utility of modeling at all stages of the material "lifecycle", from selecting an initial synthetic target to providing complementary insight into spectroscopic measurements and suggesting material modifications to optimize physical properties toward the intended application. Atomistic simulations using, for example, electronic-structure methods such as DFT are particularly powerful and are becoming increasingly commonplace, but more "phenomenological" modeling, such as using empirical rate laws fitted to experimental data to predict kinetics, remains an important complementary technique. As first-principles modeling and advanced spectroscopic techniques continue to become more widely available, tighter integration between theory and experiment will be a key factor in establishing new insights that will ultimately yield novel functional molecular materials with tunable properties to meet contemporary challenges.

9. MATERIALS FOR NUCLEAR REACTORS

The first electricity-generating nuclear power plant, with an experimental breeder reactor, began operation in 1951 in the United States; since then, a lot of effort has been spent toward improved efficiency and safety.[221−224] Most common challenges are the effects of radiation and temperature on the structural materials, which are key elements for containment of nuclear fuel and the fission products. During fission, α particles are emitted becoming helium particles by capturing electrons from the surrounding structural materials. Initially He radiation damage appears in the form of local defects; however, these defects quickly agglomerate and interact with the underlying structure causing undesired effects such as blistering.[225−227] Helium atoms can rapidly diffuse through interstitial sites even below the room temperature.[228] Usually, they form bubbles, which cause embrittlement within the material, resulting in degradation of its mechanical, thermal, and electronic properties. Several classes of structural materials have been proposed[229] to guarantee the successful operation, maintenance, and long life span of the reactor; nonetheless, defect-induced blistering and helium embrittlement are still issues to be handled.

9.1. Nanoscale Metallic Multilayer Composites. It has been known for decades that surfaces, grain boundaries, and interphase boundaries act as sinks for radiation-induced point defects and traps for He.[230] However, the detailed mechanisms at the level of the atomic structure of an interface, which enable a nanocomposite to be stable under high irradiation flux or high concentration of He, are only just started to be clarified through studies of model systems, where ion irradiation is integrated with atomistic modeling.[231] The emergence of new concepts using nanoscience in the design of bulk structural materials shows promise to provide the breakthroughs needed for future nuclear energy systems. In particular, the design and control of interfaces and complex defect structures could lead to self-healing materials with extremely low sensitivity to radiation damage. Such a concept has the potential to make radiation damage a much less critical factor in technical design and opens new horizons for nuclear energy sector.

Nanoscale metallic multilayer composites (NMMC), which contain many interfaces between different types of metals, represent a step-change in the design of nuclear materials, with the potential to overcome limitations of existing technologies. Recently, a promising heterophase interface design approach was proposed, where interfaces could be produced to act as efficient sinks for irradiation-induced vacancy-interstitial (Frenkel) pairs, leading to their enhanced recombination and thus restoring part of the material to its undamaged state.[232] Such concept has been illustrated using a Cu/Nb nanolayered system.[231,233−241]

A Cu/Nb multilayer composite is produced using magnetron sputtering technique and is shown in Figure 16a,b as an example. The combination of such interface with a multilaminate material design concept[231,232] has been shown to produce nanostructured materials exhibiting ultrahigh strengths (hardness ~5−7 GPa for Cu/Nb) and enhanced radiation damage tolerance.[232,242−244] The unique ability of Cu/Nb interfaces to trap and recombine Frenkel pairs created during irradiation-induced collision cascades can be traced back to the unusual properties of interfacial point defects in Cu/Nb multilayer composites. One of the most noticeable differences between the behavior of such defects and the ones present in perfect crystalline environments of the corresponding element is the greatly reduced formation energy of interfacial point defects compared to the latter. For example, in the Cu/Nb system, vacancy formation energy drops from 1.3 to 0.3 eV for Cu and from 2.8 to 1.1 eV for Nb,[237,238] while in the Zr/Nb system, the same energy drops from 2.0 to 0.8 eV for Zr[245] as the vacancy migrates to the interface. Vacancies and interstitials that migrate to the Cu/Nb interfaces are effectively trapped there and undergo accelerated recombination due to the enhanced diffusivity and effective size of interfacial point defects.[232,233,240,241,246,247]

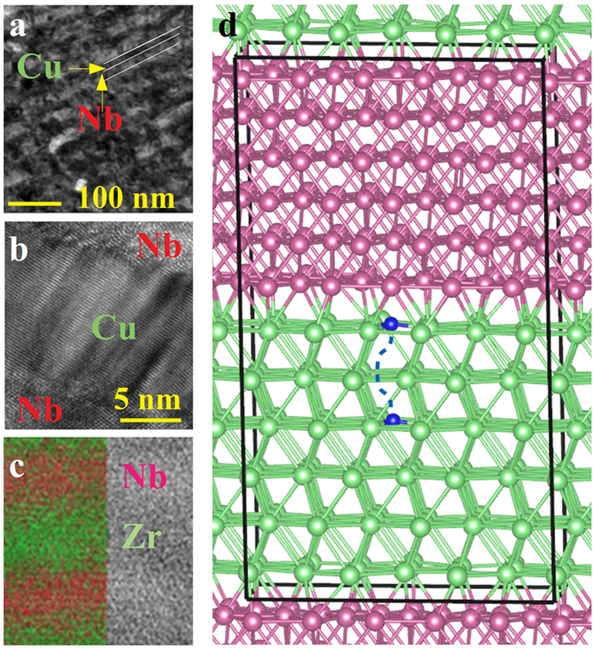

Figure 16. Various NMMCs produced using magnetron sputtering method (a) Cu/Nb, (b) Cu/Nb enlarged, (c) Zr/Nb systems. (d) The unit cell used in DFT calculations to model the system in (c): pink, green, and blue spheres represent Nb, Zr, and He atoms, respectively. The blue line represents the migration path of He atom (from right to left) toward the interface.

Unlike vacancies and interstitials, helium atoms cannot be annihilated via recombination, thus remaining as impurities within the material. Two prospective interfaces are mostly studied including irradiation testing: Cu/Nb[247−253] and Cu/W[254−257] both experimentally and computationally. In copper-based systems, relevant mechanisms governing the He dynamics seem to be identified,[230] and the total amount of He atoms that can be trapped at the interface is obtainable by considering two key quantities: the misfit dislocation intersections (MDIs) density, which depends on geometrical and chemical parameters and finally identify the availability of nucleation sites, and the maximum number of He atoms that can be accommodated into a cavity preventing a "platelet-to-bubble" transition to occur. Furthermore, these systems also show promising properties in the sequestration and arrest of He bubble growth.[248,253] Structural analyses on implanted samples showed interfaces decorated by He bubbles thus underlying the key role also played by Cu/X interfaces. However, Cu exhibits significantly lower energy barrier with respect to X for vacancy formation (0.5 eV for Cu and 2.18 eV for W at the interface) and migration (vacancy migration barrier of 1.07 eV inside Cu and 1.79 eV inside W) in Cu/W multilayer system, and self-diffusion barrier (0.7 eV/atom for Cu and 1.2 eV/atom for Nb) in Cu/Nb multilayer system.[254,258] In combination with lower Cu homologous temperature, He bubbles formation occurs exclusively in Cu layers.[255] The unbalanced He bubbles distribution between constituent elements is accompanied by development of complex residual stress distributions in W layers and leads to the degradation of mechanical and functional properties already at ambient temperature. Moreover, in generation IV reactors, temperatures greater than 500 °C are expected; unfortunately, this strongly limits the use of copper, since temperature-driven recrystallization and crystal growth already occur at ~300 °C.[259−261] On top of that, at high temperatures, functional properties (hardness, toughness) of Cu/Nb[262] and Cu/W[263] films drop significantly. Because of the issues mentioned above, although Cu/X is profoundly studied as a model material to understand the role of interfaces in radiation environments, its employment in nuclear industry would be rather limited. This appealed for the selection of other materials with suitable thermal and structural stability. It was evident that Cu is a weak point in the interface design; substitution of Cu by Zr could indeed represent the key solution allowing for a prompt introduction of this class of materials in the future of nuclear industry. Among various systems, the Zr/Nb one has been identified[245,255,264−267] as appropriate from mechanical and thermal stability point of view. Zr/Nb system outperforms mechanical properties of Cu/Nb and W/Cu above 300 °C; indeed Zr−Nb alloys are currently used in CANDU-type reactor.[268] Zr/Nb interfaces have recently been prepared[255,264−267] in a multilayer architecture using magnetron sputtering method (Figure 16c). The results indicate that the Zr/Nb system retains high hardness (reaching as high as 13 GPa) even at 400 °C and shows remarkable resistance to γ[266] and heavy Si ion[267] radiation. High interface-to-volume ratio due to small crystallites is expected to have exceptional positive effects on the self-healing properties of the materials subjected to radiation damage.

DFT calculations[245] indicate Zr/Nb multilayer systems retain most of the mechanical properties of their bulk forms, thus becoming promising candidates for nuclear applications. The electronic structure calculations further reveal that He atom prefers to sit at the low electron density region within the material. He atom is either trapped by a vacancy or is drawn to the Zr side of the interface, due to the charge transfer at the interface, which makes Zr side positively charged. The unit cell for this calculation and the migration path for He toward the interface is shown in Figure 16. Similarly, it is energetically favorable when the vacancy within the material is in the Zr side of the interface, so as to minimize the stress that is generated by the presence of the vacancy in the first place. Therefore, both He atom and the vacancy are drawn to the Zr side of the interface, although due to different reasons. To sum up, evolution of nuclear technology allows us today to harvest energy from nuclear reactions by means of nuclear power stations in a controlled and safe way. However, there are still problems related to the structural components of the reactors limiting the harvested energy and life span of the reactors themselves. Although many of these issues can be resolved through the use of proper materials, defect-induced blistering and He embrittlement have yet to be worked out. Recently proposed NMMCs can be a solution to these final problems.[231] So far, Zr/Nb multilayer composites appear to be a great candidate, but still further research is required.

9.2. Outlook. Several possible NMMCs can be designed. For example, Mg/Ti (hcp/hcp) interface, similar to Zr/Nb, could be an interesting candidate owing to the mutual immiscibility of the constituent elements, which may lead to high thermal and compositional stability.[269] The lattice mismatch and consequently misfit strain (∼8.6%) between Mg and Ti would give birth to a misfit dislocation network well acting as a sink for helium atoms. Moreover, the high mechanical stiffness-to-weight ratio makes this combination also particularly suitable where high specific strength is required.[270] Even if the He atoms are attracted to the interface, a way to prevent their accumulation and hence bubble formation must be identified.

It has been shown[245] that He atoms follow the lower electron density regions inside the material. Therefore, by manipulating the charge density within the material, it might be possible to lead He atoms out of the system, thus taking the He embrittlement part of the problem totally out of the picture.

10. NOVEL MECHANISMS FOR IMPROVED OXIDE THERMOELECTRICS EXPLORED FROM FIRST PRINCIPLES

Transition-metal oxides where electronic correlations play an important role[271,272] are an attractive materials class for thermoelectric applications. They exhibit a substantial chemical and thermal stability and are generally environmentally friendly. Considerable experimental and computational[273,274] effort aims at finding oxide thermoelectrics with improved performance, usually by maximizing the electronic contribution to the thermoelectric figure of merit $ZT = \sigma S^2 T/(\kappa_{\mathrm{el}} + \kappa_{\mathrm{ph}})$, namely, the electrical conductivity σ and the Seebeck coefficient S at temperature T. At the same time, electronic and lattice contributions to the thermal conductivity, κ_{el} and κ_{ph}, need to be as small as possible.

In bulk materials, *n*- and *p*-type thermoelectric response is commonly attained by doping,[275−277] a prominent example being La-doped $SrTiO_3$ (STO) single crystals,[278] or epitaxial films.[279,280] A different route is to utilize the impact of epitaxial strain on the electronic structure. Specifically, the delafossite $PtCoO_2$ exhibits a remarkable change in thermopower when varying from tensile to compressive strain.[281] This is related to a reconstruction of the Fermi surface topology, that is, a strain-induced shift of additional bands through the Fermi energy. An alternative strategy is to exploit heterostructuring and dimensional confinement,[282,283] a concept that is not only applied to oxides[284−292] but also used in Heusler/oxide magnetic tunnel junctions[293] or Heusler/metal hybrid systems.[294−296] This is based on the recent ability to grow transition-metal oxide superlattices (SLs) with atomic precision.[297−299]

Next, three different approaches to design thermoelectric properties are described, which go beyond the initial proposal by Hicks and Dresselhaus.[282] Such approaches rely on the insight that can be obtained from atomistic simulations within the framework of DFT combined with Boltzmann transport theory. The focus is on the correlated metal $LaNiO_3$ (LNO) heterostructured with the band insulators STO[290] or $LaAlO_3$ (LAO),[291,292] materials that can be grown epitaxially "cube-on-cube" in their natural perovskite ABO_3 structure,[300−304] as well as in the form of Ruddlesden−Popper/perovskite hybrid structures.[299,305,306] While LNO and STO result in polar interfaces, the LNO/LAO materials combination is nonpolar but, nonetheless, shows intriguing properties concerning confinement and strain. A discussion and an outlook on the influence of the phonon system close this section.

10.1. Impact of the Interface Polarity on the Thermoelectric Response. An efficient thermoelectric energy conversion requires both n- and p-type materials that are structurally and electronically compatible. It has been recently shown that this can be realized in oxide SLs by exploiting the interface polarity.[290] In particular, the mechanisms of electronic reconstruction at polar oxide interfaces[307,308] have attracted significant interest in the past decade.

In LNO/STO(001) SLs, variation of the stacking sequence at the interface generates different types of SLs, particularly an electron-doped one with n-type $(LaO)^+/(TiO_2)^0$ interfaces (IF-*n*), or a hole-doped one with $(NiO_2)^-/(SrO)^0$ interfaces (IF-*p*). The resulting stoichiometries for SLs with three layers of each material are $(LNO)_{3.5}/(STO)_{2.5}$ for the n-type SL and

$(LNO)_{2.5}/(STO)_{3.5}$ for the p-type SL. Both structures are displayed in Figure 17a. DFT+U calculations show that the charge mismatch at the interfaces is exclusively accommodated in the nickelate region by shifting upward/downward the Fermi level for the SL with n-/p-type interfaces, while STO is rather a spectator. This is in sharp contrast to the much-studied LAO/STO(001) system, where the Ti 3d states are involved.[308,309] Transport calculations within Boltzmann theory show that the distinct band alignment between LNO and STO in the two stacking sequences leads to either n- or p-type thermoelectric response of the SL in cross-plane direction (Figure 17b). While in the n-type case the electronic transport involves tunneling through the insulating STO region, the particular position of the STO valence band maximum directly below the Fermi level in the p-type SL strongly boosts the thermoelectric response with a Seebeck coefficient of +135 μV/K at room temperature.

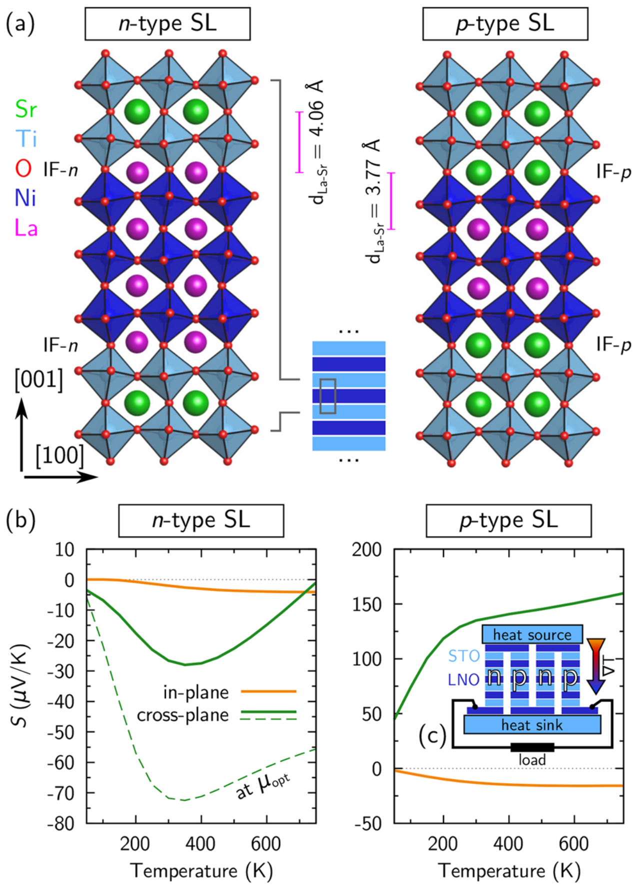

Figure 17. (a) Side views of the optimized geometry of LNO/STO(001) SLs with interfaces of opposite polarity (IF-n or IF-p) grown on STO. The La−Sr distance d_{La-Sr} across the interface acts as a fingerprint of the interface type, being elongated for an electron-doped SL and compressed for a hole-doped SL. In both cases, significant octahedral tilts are induced in the STO part. (b) Thermoelectric response of the SLs. The sign of the cross-plane Seebeck coefficient S is consistent with the polarity of the interfaces (negative/positive for n-/p-type). Additional doping (μ_{opt}, see ref 290) enhances the performance. (c) Illustration of a thermoelectric generator based on n- and p-type SL legs composed of the same materials combination (Adapted from ref 290).

We note that a related concept was proposed by Botana et al.[310] for CrN/MgO(111) SLs, which however differs in the strong charge mismatch at the interface (formal charge of the layers at the interface: $2^-/3^+$) that may drive the formation of compensating defects, and the fact that the voltage builds up perpendicular to the thermal gradient. Since polar interfaces occur also in many other systems, for instance, in group IV/III−V semiconductor heterostructures such as Ge/GaAs,[311] the outlined concept is not restricted to oxides but may be relevant for other classes of materials.

10.2. Epitaxial Strain as Control Parameter in a System with Confinement-Induced Metal-to-Insulator Transition.

In doped bulk materials or epitaxial films,[278−280] the carrier concentration is used as control parameter to maximize the power factor PF = σS^2. The highest power factor is usually found in the intermediate regime between semiconducting and metallic behavior, which provides the best tradeoff between Seebeck coefficient (which reflects the transmission asymmetry near the chemical potential μ and thus benefits from the band gap in a semiconductor) and electrical conductivity (which is largest in a metal). In the following, it is shown that epitaxial strain can take on a similar role in artificial transition-metal oxides.

Nonpolar LNO/LAO(001) SLs are an intensely studied system.[300,304,312,313] In the ultrathin limit, epitaxial strain together with quantum confinement drive a metal-to-insulator transition in $(LNO)_1/(LAO)_1(001)$ SLs (Figure 18a).[291,312] The emerging band gap for tensile strain (~0.3 eV for a_{STO}) leads to a strong enhancement of the thermoelectric response, as one can infer from Figure 18. A particularly interesting aspect of this system is that the short-period SL design in the [001] direction (cross-plane) considerably improves the *in-plane* thermoelectric performance. Consequently, the in-plane power factor outperforms the cross-plane one due to the much higher in-plane conductivity. Comparing the conductivity obtained from DFT+U for $(LNO)_3/(LAO)_3(001)$ SLs with experiment,[304] the relaxation time at room temperature was estimated to be $\tau \approx 4$ fs. This results in in- and cross-plane Seebeck coefficients of ±600 μV/K and an in-plane power factor of 11 $\mu W/K^2$ cm at approximately room temperature, making the system comparable to some of the best-performing oxide systems such as La-doped STO[278−280] or layered cobaltates.[314] Further increase of the epitaxial strain (e.g., as induced by a $DyScO_3$ substrate) does not lead to an additional enhancement, but on the contrary it reduces the power factor again due to a decrease of the in-plane conductivity at the edges of the further increased band gap.[291]

Increasing the thickness of both constituents to three layers each in $(LNO)_3/(LAO)_3(001)$ SLs deteriorates the thermoelectric performance due to the two-dimensional metallic nature of the LNO region and the too-thick large-band-gap LAO spacer layer, irrespective of the epitaxial strain. This underlines the key role of quantum confinement.

It is then concluded that a significant enhancement of the thermoelectric properties can be obtained in oxide SLs such as $(LNO)_1/(LAO)_1(001)$ at the verge of a metal-to-insulator transition.

10.3. Transport Resonances Tuned by Strain Engineering of the Orbital Polarization.

Above it has been discussed that n- and p-type thermoelectric response can be induced in polar oxide SLs by a selective design of the stacking sequence at the polar interfaces.[290] In the following, it is shown

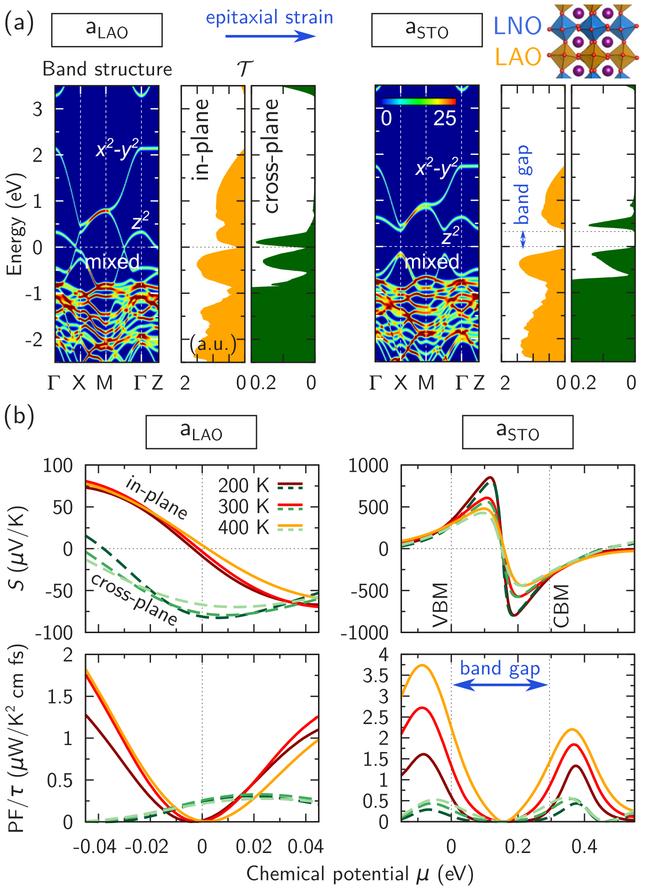

Figure 18. (a) In ultrathin $(LNO)_1/(LAO)_1(001)$ SLs, increasing the substrate lattice constant from a_{LAO} (compressive strain) to a_{STO} (tensile strain) drives a metal-to-insulator transition,[312] as one can see from the band structure diagrams and the corresponding transmission $\mathcal{T}$. (b) This is accompanied by a drastic enhancement of the thermoelectric response (Seebeck coefficient S and power factor PF), both in-plane and cross-plane. Further increase of strain was found to be counterproductive.[291] Adapted from ref 291.

that the same goal can be achieved in nonpolar SLs by strain engineering of the orbital polarization.[292]

Designing the thermoelectric response of a system necessitates quantum control over the asymmetry of its spectral transmission function $\mathcal{T}$ around the Fermi energy.[293,315] Mathematically, it has been shown decades ago that transport resonances are attractive for thermoelectric applications.[316] Nevertheless, the explicit use of these resonances has been limited to model studies.[317,318] To pursue this route, (i) a transmission function $\mathcal{T}$ exhibiting sharp resonances must be designed, and (ii) a mechanism that allows for a precise tuning of the transport resonances with respect to the Fermi energy is required.

This concept has been demonstrated on the basis of first-principles calculations in $(LNO)_3/(LAO)_1(001)$ SLs,[292] which are displayed in Figure 19. The confinement of three layers of LNO separated by a single LAO spacer layer induces the formation of distinct Ni $3d_{x^2-y^2}$- and $3d_{z^2}$-derived quantum well (QW) states, while at the same time permitting cross-plane electronic transport through the single LAO spacer layer. This leads to the emergence of sharp cross-plane $3d_{z^2}$-derived transport resonances (Figure 19b). Epitaxial strain strongly impacts the orbital polarization in this system and thus the relative energy and occupation of the $3d_{x^2-y^2}$- and $3d_{z^2}$-derived QW states (Figure 19a). Because of this charge redistribution mechanism, the $3d_{z^2}$-derived transport resonances can be shifted with high precision relative to the Fermi energy. Thereby, considerable n- and p-type thermoelectric response (ca. −60 to +100 μV/K at approximately room temperature) can be obtained in one and the same materials combination by moderately varying the control parameter epitaxial strain between −1.5 and −2.8% (Figure 19c). It has been shown that this concept is robust with respect to the formation of oxygen vacancies.[292]

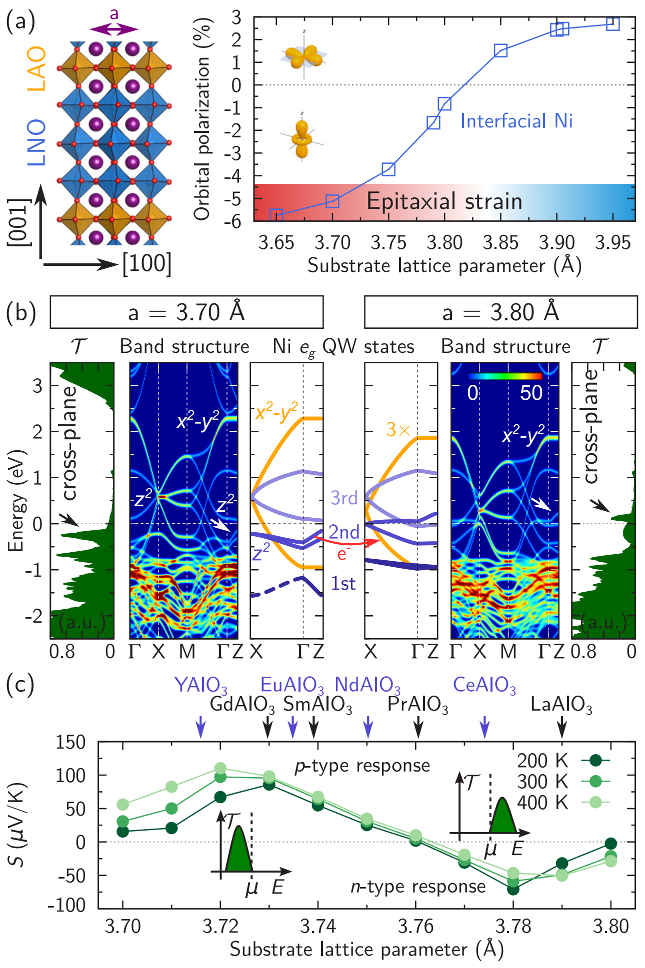

Figure 19. (a) Side view of the optimized geometry of a nonpolar $(LNO)_3/(LAO)_1(001)$ SL (a = 3.79 Å), together with the Ni e_g orbital polarization in the interfacial LNO layers as a function of the substrate lattice parameter a that varies from −6% (compressive strain, red shaded) to ca. +3% (tensile strain, blue shaded). (b) Confining three layers of LNO separated by a single LAO spacer layer leads to the formation of distinct QW states with Ni e_g character. Their relative occupation (and thus the orbital polarization) can be precisely tuned by epitaxial strain. In particular, resonances emerge in the cross-plane transmission $\mathcal{T}$ (black arrows) that are associated with the $3d_{z^2}$-derived QW states (white arrows) and can be shifted with respect to the Fermi energy by moderately varying the degree of strain. (c) With this strain engineering of the orbital polarization, considerable n- and p-type thermoelectric response can be achieved in the system. Exemplarily, some (rare-earth) aluminate substrates are marked. Adapted from ref 292.

This work exemplifies how the thermoelectric properties of oxide heterostructures can be controlled and optimized by varying layer thickness, quantum confinement, and epitaxial strain. Moreover, it manifests an application for the control of orbital polarization, which is intensively pursued in artificial transition-metal oxides.[312,319−322]

10.4. Outlook: The Role of Phonons. On the one hand, the focus of most theoretical studies lies on improving the electronic contribution to the thermoelectric figure of merit *ZT*, that is, optimizing conductivity σ and Seebeck coefficient *S*. On the other hand, the impact of phonons, which affect (i) the relaxation time τ and (ii) the lattice contribution to the thermal conductivity κ_{ph}, is often neglected. Both quantities can be obtained from first-principles: The relaxation times have been calculated very recently for bulk Si[323] and for elemental noble metals,[324] employing a combination of DFT and many-body perturbation theory. On the one hand, because of the high numerical demand, this approach has not been applied so far to more complex systems such as the oxide SLs discussed here. The thermal transport, on the other hand, has been calculated recently for bulk MgO by a complete solution of the linearized Boltzmann transport equation.[325] Larger systems such as Fe/MgO/Fe(001) magnetic tunnel junctions have been treated within a Green's function framework.[326]

Exploiting interface scattering of phonons by heterostructuring is a viable strategy to reduce the lattice thermal conductivity.[283,327−329] In SLs, the periodicity has a strong impact, and it has been demonstrated experimentally that at the crossover point between incoherent to coherent phonon scattering in oxide SLs the lattice thermal conductivity exhibits a minimum.[330] However, the parameters corresponding to this optimal point have to be determined in each specific case. High crystalline quality is beneficial for electronic properties, but simultaneously it can lead to coherent phonon heat conduction, and it has been shown for GaAs/AlAs(001) SLs that the thermal conductivity can even increase with the number of layer repeats.[331] In short-period SLs the thermal conductivity can exceed that of the constituent materials, as has been demonstrated for Si/Ge(001) SLs.[332] This highlights that further effort is required to explore the influence of heterostructuring on the phonon system from first principles.

11. POLAR, FERROELECTRIC, AND MULTIFERROIC METALS: THREE CASE STUDIES

Here, case studies of polar,[333] ferroelectric,[334] and multiferroic[335] metals are discussed, where polar symmetry—and in some cases, polarization itself, is actually realized in metals. The idea of ferroelectric metals harkens back to a suggestion by Anderson and Blount[336] that some metals may possess, or acquire, polar symmetry, that is, one compatible with the existence of electric polarization. Whether a polarization and attendant phenomena, would actually materialize as a consequence was left unspecified, and this is one of the issues being investigated, mostly theoretically so far.

It is appropriate to have a checklist for the definition of a ferroelectric metal: it should

(i) be a metal.
(ii) have polar symmetry.
(iii) have a measurable or computable zero-field polarization *P*.
(iv) optionally support a polarization-induced depolarizing electric field when cast in finite form (e.g., thin film), which would imply the actual switchability of *P*.

The last requirement is optional, because even bona fide ferroelectrics often do not satisfy it: a large polarization in a film causes a large depolarizing field, which destroys the polar distortion and, ultimately, the polarization itself.

11.1. Metascreening in Metalized Ferroelectrics. Polar metals should satisfy the (i) and (ii) requirements. A further distinction can be made between metals that are or can be rendered polar and polar insulators, which are made robustly metallic. Among the former, let us briefly mention $LiOsO_3$ and related composite systems, which stands out in both experiment and theory,[337−339] and the general guidelines laid out for their search.[340]

In this section, the mechanism that causes metalized ferroelectrics to conserve polar distortions, that is, to become polar metals, is discussed. Figure 20 shows the amplitude of the polar distortion as a function of free charge density of either sign, normalized to the value at zero added charge, for a limited selection of the materials discussed in ref 333. Evidently, all materials exhibit stable polar distortions as a function of charge density of both signs, except three of them whose distortion dies out at high n-type density.

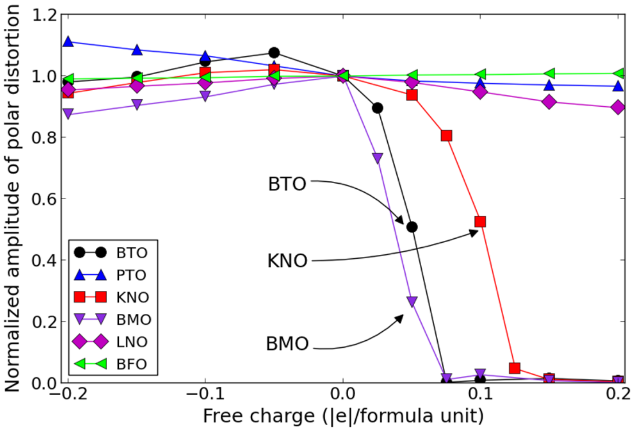

Figure 20. Normalized polar amplitude vs carrier density for a sample of metalized ferroelectrics. In the legend, $BaTiO_3$, $PbTiO_3$, $KNbO_3$, $BaMnO_3$, $LiNbO_3$, and $BaFeO_3$ compounds are represented by the element initials, respectively. For example, 0.1 |e|/formula unit are 1.5 × 10^{21} cm^{-3} in BTO. Figure adapted from ref 333.

$BaTiO_3$ (BTO) is an interesting case, as it allows to monitor the transition from polar to nonpolar phase. As detailed in ref 333, in an 80 Å long supercell of cubic BTO perturbed by a dipolar displacement of a plane of Ti atoms, it is found that free charge screens out long-range interactions over a typical length scale of less than 10 Å from the perturbation. Doping produces a concurrent short-range effect (referred as *metascreening*) that enhances the distorting forces on the atoms in the immediate vicinity of the perturbation; specifically, a lattice distortion near the perturbation accommodates the screening electrons or holes, and it is essentially indistinguishable from the original polar distortion in the undoped case.

To prove that this effect is not a consequence of incomplete screening but indeed due to short-range effects, one can calculate the stiffness constant for the soft ferroelectric mode $\mathcal{S} = \mathbf{s}^T \cdot \mathbf{F} \cdot \mathbf{s}$, with $\mathbf{F}$ the force constant matrix calculated at the Γ point and $\mathbf{s}$ the soft-mode eigenvector. Another stiffness $\mathcal{S}_{sr}$ is calculated, just the same way as $\mathcal{S}$, except that the force constants between neighboring Ti atoms are always those of the undoped case, independently of the doping level: the shortest-range interactions are thus frozen into the undoped configuration. On the one hand, as Figure 21 reports, $\mathcal{S}$ is negative for all free carrier densities up to ca. +0.05 |e|/formula unit, predicting a polar distortion in accordance with Figure 20; on the other hand, $\mathcal{S}_{sr}$ is always positive, corresponding to stability against polar distortion, except in the undoped case. This shows directly that the metascreening short-range forces are the key enabler of the survival of the distortion in the doped system.

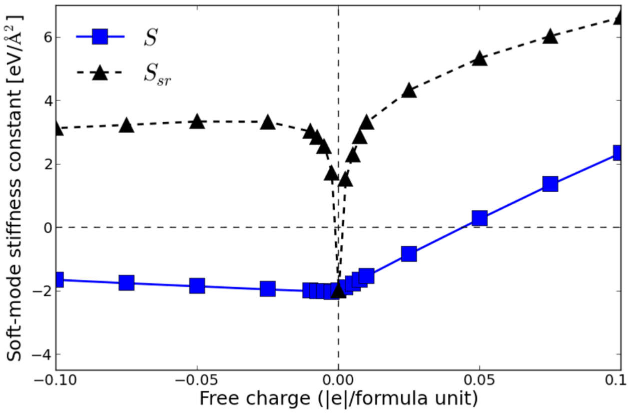

Figure 21. Force constants vs carrier density for metalized $BaTiO_3$. Negative values of the stiffness indicate the occurrence of a polar distortion, while positive values correspond to stability against polar distortion.

11.2. A Ferroelectric Metal.

A proper ferroelectric metal obeying all the requirements in the checklist has been found[334] in a different, and so far unique in this respect, class of materials: the layered perovskites of the $A_nX_nO_{3n+2}$ class, which features prominently $n = 4$ ferroelectrics and multiferroics such as $La_2Ti_2O_7$ and $La_2Mn_2O_7$.[341] The $n = 5$ class is trivially metallic from electron counting with a density of ∼3×10^{21} cm^{-3}, but the ferroelectric mechanism active in $n = 4$ materials[342] does not apply. Luckily, it turns out that $Bi_5Ti_5O_{17}$ (BTO-5517 below) has polar symmetry $Pm2_1n$, with polar axis equal to the stacking direction b, due to local chemical Bi−O dipoles (analogous to $BiFeO_3$), and, thus, BTO-5517 is a polar metal in agreement with points (i) and (ii).

The computability of zero-field polarization P, point (iii), is potentially contentious, because the Berry phase polarization[343] is ill-defined in its original form if the number of occupied bands change along the k integration direction (parallel to P itself), as expected in metallic conduction bands. The conduction bands in BTO-5517, however, are very flat along P (i.e., $k_{\|}$) direction; thus, for all numerical intents and purposes, the number of occupied bands will not change along $k_{\|}$, and a convergent P will be obtained as usual on a finite grid made up of string parallel to the P direction. To cure the unavoidable occasional crossings (the bands are not perfectly flat), P is calculated as the 2D average of a renormalized phase subject to a charge conservation constraint.[334] Physically, this corresponds to Fermi surface sections that are quasi-1D lines when projected on the $k_{\perp}$ plane (i.e., with zero measure in that plane, perpendicular to the integration direction) as is the case in BTO-5517 or to conduction charge that is strongly localized within the blocks and not very mobile. The latter view suggests to also estimate the polarization simply as the dipole of a single block. The modified Berry approach and the block-dipole approximation give similar values for the conduction band, ∼5 $\mu C/m^2$; summing up the dominant valence and ionic contributions, a large total $P = 35$ $\mu C/m^2$ is obtained, in the same league as ferroelectrics such as $BaTiO_3$.

To complete point (iii) and address point (iv) in the checklist, it is here demonstrated that the material can support a depolarizing field (i.e., the polarization can be switched). To this end, a BTO-5517 layer is cladded with the insulator $Ba_2Zr_2O_7$; this configuration is an open circuit with no current flow, which will instead occur if BTO-5517 is contacted directly. In Figure 22, showing the electrostatic potential difference of the polar and nonpolar superlattice, the metallic layer screens only partially the polarization-induced depolarizing field. The polarization will thus switch, as in ferroelectrics, upon application of a field exceeding the depolarizing field (i.e., the finite screening ability of the layer). The free-charge response in the finite system is limited by the small amount and localization of the mobile charges, and the screening ends up being incomplete; the multilayer is in effect a dielectric medium with finite low-frequency, low-wavevector dielectric function in agreement with recent results on sub-nanometer metal−air multilayers.[344]

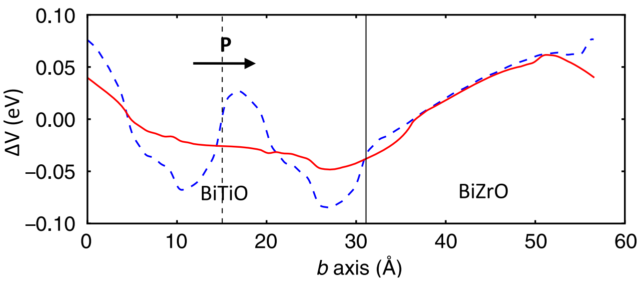

Figure 22. Potential difference of the polar and nonpolar BiTiO-5517/BiZrO-227 SL, exhibiting the sawtooth shape due to interface polarization charge. The two lines correspond to two different running-average filters. Figure adapated from ref 334.

Single-domain BTO-5517, not only polarized but also sustaining a polarization-generated depolarizing field, contradicts the usual assumption that a large polarization cannot survive its own depolarization field in a thin film.

In this respect, BTO-5517 is unlike other ferroelectrics precisely because of the self-screening mechanism that cancels in part the depolarizing field, while not destroying the chemically driven polar distortion. In this context, BTO-5517 behaves as a limiting case of hyper-ferroelectric,[345] and it might be dubbed a self-screened hyper-ferroelectric metal.

11.3. A Three-Order-Parameter Multiferroic Metal.

Thinking along the same lines as for BTO-5517, a natural extension is to look[335] for possible multiferroicity in $Bi_5Mn_5O_{17}$ (BMO henceforth), where magnetism is expected due to Mn ions and metallicity. The result is partially analogous to BTO-5517, in that Bi−O dipoles again cause ionic polarization; the symmetry is the same as in BTO-5517, but the polar axis is now c, the (110)-like axis orthogonal to the stacking axis. The total polarization, calculated in the same way as before, is ∼5 $\mu C/cm^2$; the conduction contribution is minor, ∼0.05 $\mu C/cm^2$; the Fermi surface is indeed flat, sheetlike, and closely parallel to the c axis.

As hinted above, due to the Mn ions interacting via double exchange, BMO is a ferromagnet with average moment 3.2 μ_B. In fact, it is a half-metallic ferromagnet, with a metallic majority spin channel and insulating minority (with a gap of ∼3 eV using self-interaction corrections). Interestingly, the polarization is nonzero in both spin channels and larger in the majority than the minority spin channel by roughly a 3 to 1 ratio.[346] A definite point of interest in the O-rich layered phase BMO is that, according to the calculations,[335] it is thermodynamically favored over the known BiMnO$_3$ normal perovskite phase in a sizable window of O chemical potential, favoring the synthesis of BMO unlike that of BTO-5517, which has not been achieved yet.

Demonstrating the existence of a depolarizing field in BMO is trickier than in BTO-5517, because there is no natural way of stacking BMO and an insulator along *c*. Eventually, cladding BMO with the *n* = 5 compound BaLa$_4$Zr$_5$O$_{17}$ (with a gap of ∼2 eV) ended up doing the trick. Again, as in the case of BTO-5517, there is a charge monopole at the metal−insulator interfaces and a residual field inside both the metal and the insulator. The screened-field energy density is much lower than the stabilization energy of the polar distortion (which is a bit larger than that of BaTiO$_3$, suggesting thermal stability up to at least 400 K), so the distortion is not affected by the depolarizing fields. Hence BMO checks all the boxes in the checklist and qualifies as a ferromagnetic ferroelectric metal.

Actually there is more to the story: BMO turns out to also have ferrotoroidic order; that is, its magnetic symmetry allows for a nonzero toroidal moment **T**, a polar vector that inverts under time reversal. The symmetry group is the only one such that **T**, **P**, and **M** are all mutually orthogonal, and since noncollinear magnetic calculations show that the magnetization **M** points along *a*, it eventually turns out that $\mathbf{T} \approx \mathbf{P} \times \mathbf{M}$ in this case. Both time reversal *and* inversion breaking are needed for a nonzero **T**, which implies that **T** would be nonzero even if **P** were suppressed by electronic screening, as long as the symmetry remains polar. Finally, magnetoelectric coupling also occurs in BMO; it happens to be off-diagonal (i.e., cross-field), and its value seems rather large.

11.4. Outlook. The just-discussed work on metalized ferroelectrics, especially layered perovskites, has revealed a wealth of unexpected effects. Among the open issues, the possible existence of energy-degenerate ferroelectric and antiferroelectric states, and the related (probably unusual, if not exotic) properties and dynamics of domain boundaries appear worth addressing, while waiting for experimental endeavor to prove predictions about metallic ferroelectricity in general.

12. ELECTRIC MAGNETO-OPTICAL PROPERTIES IN MULTIFUNCTIONAL HYBRID MATERIALS

Hybrid organic−inorganic perovskites (HOIPs) are similar to inorganic perovskites in terms of their ABX$_3$ topology, although the combination of organic and inorganic components provides for greater compositional flexibility.[347] In common perovskites,[348] A and B are cations, and X is an anion that is coordinated to B. The A atoms are normally larger than the B atoms, and the B cation is sixfold coordinated with the X atoms to form BX$_6$ octahedron (Figure 23). The resulting octahedra are corner-shared to form a three-dimensional framework in which the A site cations are located inside the framework cavities. In addition to their physical properties, many of their functionalities are controllable with external stimuli—for instance, magnetic field, pressure, electric field, and light.

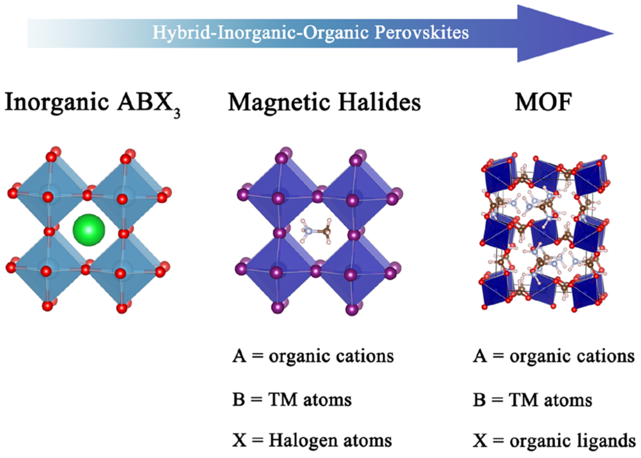

Figure 23. Starting from an inorganic ABX$_3$ perovskite: magnetic halides and metal−organic frameworks (TM: transition metal).

Hybrid organic−inorganic materials have emerging applications as multiferroics, photovoltaics, gas sensors, and transparent conductors.[347] HOIPs have a number of advantages compared to perovskite oxides. First and foremost, the A and/or X sites are occupied by organic cations and/or organic linkers, respectively (Figure 23).[349−351] At the same time, molecule-based HOIPs often have overall lower energy scales than their corresponding oxides. Quantum phase transitions—driven by magnetic field, pressure, and electric field—can thus occur at experimentally realizable conditions and be more easily controlled. These materials are also well-suited for the development of structure−property relations. For instance, the variations of the organic and inorganic components offer wide possibilities to create innovative and promising HOIPs in accordance with the generalized Goldschmidt tolerance factor.[352] This can serve as a guide for the rational design and synthesis of new HOIPs using compositions with desired functionalities and dimensionalities.[352,353] The metal−organic frameworks (MOFs) are a particularly interesting class of HOIPs (Figure 23). Here, the metal ions are linked together by organic bridging ligands, for example, carboxylate ligand (HCOO$^-$).[354] As a result, they have complex hydrogen-bonding networks that can be adjusted as a function of temperature. These materials display diverse properties including electrical, magnetic, catalytic, optical properties, multiferroic behavior, that is, coexistence of electric and magnetic ordering,[355−366] and magnetoelectric behavior,[355−366] that is, the coupling between the two long-range orderings. Like many other quantum materials, the MOFs are tunable in magnetic and electric fields.

Another emerging class of HOIPs is *hybrid halide perovskites* based on the semiconductive methylammonium (MA) lead halide MAPbX$_3$, where X = Cl, Br, I.[15,367−373] The replacement of the inorganic cation (A) by an isoelectronic organic moiety such as MA$^+$ (CH$_3$NH$_3$)$^+$ provides a unique way of tuning the chemical bonding and consequently also the optical and electronic response.[374−381]

The hybrid perovskite is a very versatile family of compounds with a large catalog of chemical components for the A and B sites.[353] For example, (i) for the A site: (NH$_2$)$_2$CH$^+$, CH$_3$NH$_3^+$, NH$_2$NH$_3^+$, (CH$_3$)$_2$NH$_2^+$, CH$_3$CH$_2$NH$_3^+$,

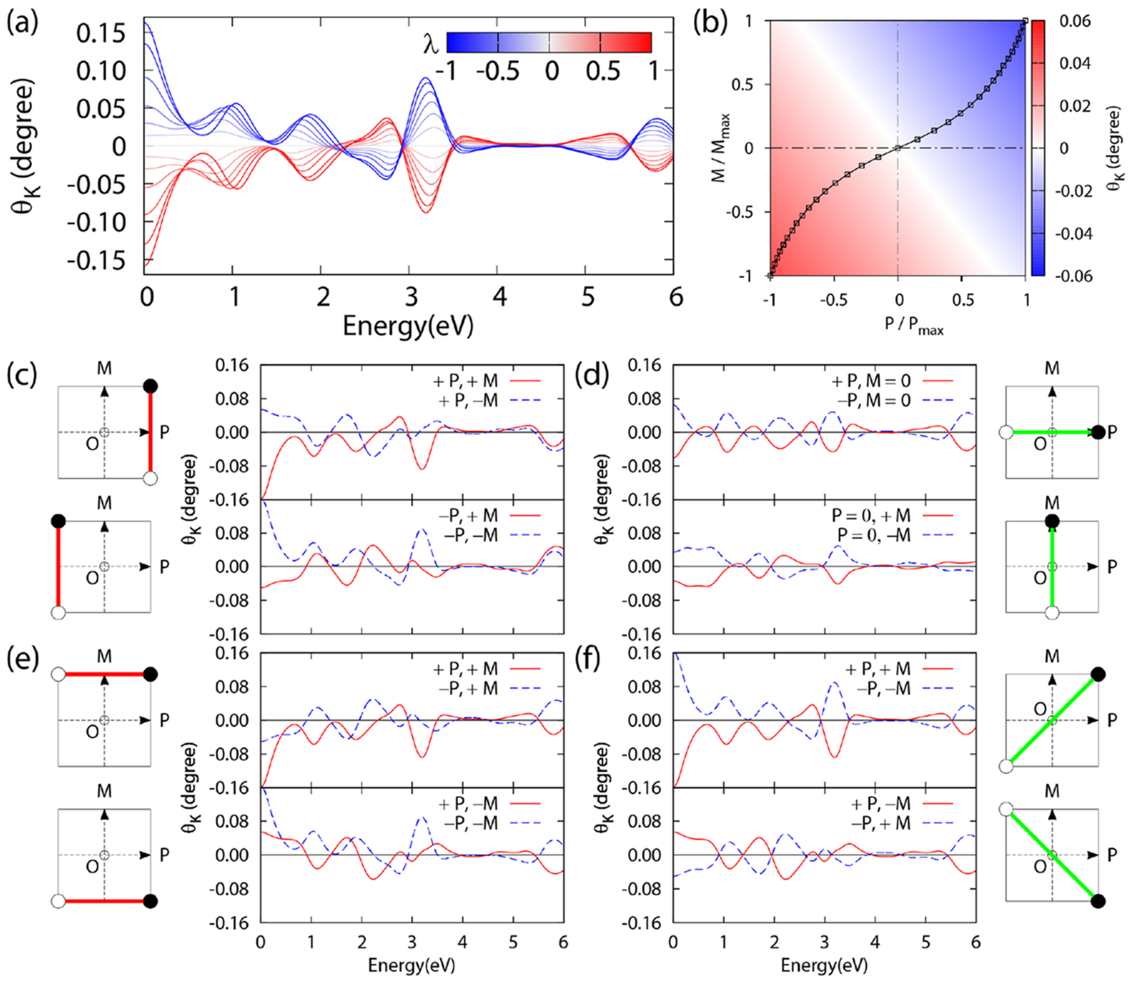

Figure 24. (a) θ_K as a function of the incident photon energy for different value of normalized amplitude of the polar distortion λ from −1 to +1. (b) Color scheme representation of different points in (P,M) space. Black curve represents the magneto-electric states, while the green line represents the locus of points with zero Kerr angle for the selected energy 3.8 eV. (c−f) Switching properties of the Kerr angle for different states in (P,M) space: green (red) lines connect states for which the Kerr angle does (not) switch.[392] The results are shown for the $[C(NH_2)_3]Cr(HCOO)_3$ MOF.

$C_3N_2H_5^+$, $C(NH_2)_3^+$, $(CH_2)_3NH_2^+$, $(CH_3)_3NH^+$, $(CH_3)_4N^+$;[352,353] (ii) for the B site: Cr^{2+}, Cu^{2+}, Fe^{2+}, Mn^{2+}, Co^{2+}, Ni^{2+};[352,353] and (iii) for X site: I^-, Br^-, Cl^-, CN^-, $HCOO^-$, N_3^-, $[N(CN)_2]^-$.

Moreover, the possibility to reduce the dimensionality by considering novel hybrid 2D materials appears an interesting direction to explore. For example, very recently, a novel magnetic 2D hybrid compound has been synthesized based on chromium-chloride-pyrazine, that is, $CrCl_2(pyrazine)_2$.[382−385] Organic molecules and magnetic metal ions can be used as molecular building blocks for synthesizing novel types of 2D materials exhibiting both electrical and magnetic properties, possibly cross-coupled to magneto-optical properties. Magnetic hybrid 2D materials are now at their infancy, and there is certainly room for new interesting physics to explore.

12.1. Symmetry Breaking and Physical Properties of Materials. *12.1.1. Multiferroicity and Magnetoelectricity.* Breaking of time-reversal (T) and inversion symmetry (I) leads to interesting changes in physical properties of crystals. If both symmetries are broken, the compound may have coexisting magnetic and ferroelectric order (multiferroicity).[386−388] It may happen that the two order parameters, that is, magnetization (M) and electric polarization (P), are coupled (magnetoelectricity)[386−388] with the possibility to tune the electric polarization by an external magnetic field and, vice versa, to tune the magnetization by an external electric field.[386−388] It is interesting to explore the unique effects of cross-coupling of ferroelectric and magnetic orders, which leads to the aforementioned multifunctional properties, on magneto-optical properties.[389−392]

12.1.2. Magneto-Optical Kerr Effect: Tunable and Switching Properties. The magneto-optical Kerr effect (MOKE) describes the change of linearly polarized light when reflected from the surface of a magnetic material. The change consists of two parts: a rotation of the polarization plane, the so-called *Kerr rotation* θ_K, and a phase difference between the electric field components perpendicular and parallel to the plane of the incident light, the so-called *Kerr ellipticity* η_K.[393] The Kerr rotation can be exploited to read suitably magnetic stored information by optical means in modern high-density data storage technology[394−397] or to probe the magnetic behavior of two-dimensional systems.[398]

The Kerr effect is described by the Kerr angle φ_K, a complex number defined as

$$\varphi_K = \theta_K + i\eta_K = \frac{-\sigma_{xy}}{\sigma_{xx}\sqrt{1 + \left(\frac{4\pi}{\omega}\right)\sigma_{xx}}} \tag{12}$$

where the complex numbers σ_{xx} and σ_{xy} are the diagonal and the off-diagonal elements of the conductivity tensor, respectively.[399,400] Equation 12 is widely used in literature and is valid only in the polar geometry, for compounds with higher than threefold rotational symmetry.[399,400] The conductivity tensor can be calculated from the electronic structure of the solid, and, therefore, Kerr effect can be evaluated based on density functional theory.[400] In a system possessing inversion symmetry *I*, linear magneto-optical activity (Kerr effect) arises from breaking time reversal (*T*), like in a ferromagnet. If the system is anti-ferromagnetically ordered, the material is expected to be magneto-optical inactive. Despite this expectation, a multiferroic MOF has been recently found,[392] with chemical formula $[C(NH_2)_3]M[(HCOO)_3$, where M = Cu^{2+} or Cr^{2+}, exhibiting magneto-optical activity even in its anti-ferromagnetic state. This result suggests that a magnetic compound may become magneto-optically active when the combined *TI* symmetry is broken.

If the system is invariant under *T* and *I* symmetry,[401−403] it does not have either magnetic or ferroelectric ordering. Breaking of *T* gives rise to magnetic ordering, while breaking of *I* is necessary for ferroelectricity. Breaking both *T* and *I* is necessary for a system to be multiferroic and/or magnetoelectric. When breaking the *TI* symmetry, the compound may be magneto-optical active.[401−404]

Moreover, in MOFs the Kerr angle can be tuned not only by *M*, as a common belief, but also by the ferroelectric polarization (*P*).[392] This raises the exciting possibility that the Kerr rotation angle could be controlled by *M*, *P*, or both—depending on the circumstances. This is an under-explored avenue for achieving the combination of functional behavior needed for logic and information storage in magnetic materials and nanostructures.

12.1.3. Switching Properties of Magneto-Optic Kerr Effect.

As a proof of principle, a series of Kerr spectra calculations on a MOF compound showing ferroelectric and magnetic ordering have been performed.[392]

Figure 24a shows the variation of the Kerr rotation θ_K as a function of the incident photon energy (*E*) for different values of the normalized amplitude of the polar atomic distortion (λ). $\lambda = 0$ represents the paraelectric state (centrosymmetric), while $\lambda = \pm 1$ represents two ferroelectric states with opposite electric polarization. The parameter λ smoothly changes from −1 to +1 through zero, and it is codified by a color scheme from blue to red through white: by changing λ, θ_K changes continuously, and the switching occurs when λ changes sign. Since λ is proportional to *P* in the material, this leads to the interesting conclusion that *Kerr angle can be tuned by P and switches its sign when switching P*. These results have been derived in the case of a magnetoelectric compound:[392] one would naively expect that this ultimately recovers the standard case of $\theta_K \propto M$, since $P \propto M$. However, as shown below, calculations can be generalized by considering *M* and *P* as independent variables:

$$\theta_K = \alpha P + \beta M \tag{13}$$

θ_K can be expressed as linear function of both *P* and *M* as reported in eq 13. In Figure 24b, $\theta_K(P,M;\, E = 3.8\ \text{eV})$ is shown as a color code. The coordinates were normalized to P_{max} and M_{max}, respectively. For each point in (*P*,*M*) space, a color that corresponds to a well-defined value of the Kerr angle is associated. Figure 24b represents the following property by a color code in (*P*,*M*) space: $\theta_K(P,M;\, E) = -\theta_K(-P,\, -M;\, E)$, that is, θ_K can be switched only when both *P* and *M* change sign. This property is more general and can be extended to other ferroelectric and magnetic compounds—even in absence of a net magnetization.

In Figure 24c−f, simulations considering *P* and *M* as independent variables in the calculations are shown. According to eq 13, θ_K cannot be switched if only *M* or *P* is reversed when both *M* and *P* are different from zero. This is shown in Figure 24c,e: in (c) +*P* (or −*P*) state is considered, and +*M* switched to −*M*; in (e) +*M* (or −*M*) state is considered, and +*P* switched to −*P*. On the one hand, no switching occurs. On the other hand, when $M = 0$ (e.g., anti-ferromagnet), θ_K changes its sign when reversing *P*. This leads to the important result that θ_K can be tuned and reversed by *P* in ferroelectric anti-ferromagnets (see Figure 24d, upper panel). When $P = 0$ (e.g., nonpolar compound), θ_K can be tuned and reversed by *M*.[392] This would correspond to the standard case of a centrosymmetric ferromagnet (Figure 24d, lower panel). In general, *θ_K can be switched only when reversing both P and M* as shown in Figure 24f. Results can be summarized in the (*P*,*M*) space. Each couple of states considered in the panels (c−f) are shown as black and white circles in this space. The black and white circles are connected by a green or red line representing the switchability or nonswitchability of the Kerr angle between them. In summary, these results suggest that (i) the Kerr angle can be modified not only by *M* but also by *P*; (ii) θ_K changes its sign only when switching both *P* and *M*; (iii) it may be possible to tune and switch the Kerr angle in antiferromagnetic compounds; (iv) it could be possible to design novel memory devices, where the information is stored by the direction of the local ferroelectric domain, and the read-out is performed by exploiting the Kerr rotation depending on the direction of the dipole. On the basis of these predictions, it will certainly be interesting to explore the emerging class of hybrid organic−inorganic quantum materials with the potential of cross-coupling magnetic and electric order to the magneto-optical properties for active tunable photonics.

12.2. Outlook.

It is important to design general principles from which material properties can be rationalized and qualitatively predicted, by focusing on the dimensionality, composition, and functional groups—by assessing their effects on the relevant properties such as *P* and *M*, which are expected to be cross-coupled to the MOKE in the materials outlined here. The Bilbao Crystallographic Server (BCS, http://www.cryst.ehu.es/) is useful for analyzing the magneto-optically activity (MTENSOR tool in BCS). The multilinear relation $\theta_K = \alpha P + \beta M$ requires (i) the evaluation of the two α, β parameters for a specific material, together with their dependence on the functional groups (A,B,X) of HOIPs[392] and (ii) understanding the microscopic mechanism of the switching properties of θ_K in terms of the underlying electronic structure, symmetry, and structural properties.[405] This will open new directions in magneto-optical Kerr engineering in complex functional materials in connection with antiferromagnetic spintronics[405−411] and topological quantum materials.[412−416]

13. TRIBOLOGY AS A NOVEL FIELD FOR ELECTRICITY GENERATION

Tribology is defined as the study of interacting surfaces in relative motion.[417] It involves various and complex phenomena, such as friction, wear, and corrosion, and it has severe implications for energy saving. It has been estimated that ∼23% of the world's total energy consumption originates from tribological contacts;[418] fortunately, several progresses have been achieved in the last decades regarding the comprehension and control of microscopic mechanisms related to friction, partly due to the advances made in simulation techniques.[419]

Despite the fact that one of the main goals of tribology is energy saving, an emerging topic is the conversion of friction into usable work. The importance of the latter becomes clear when considering the increasing demand of energy production in sustainable ways and is therefore discussed below. More specifically, the focus will now be on the production of energy through a clever control of the triboelectric effect.

In the past years, with the quick growth of electronic miniaturization, a remarkable number of novel devices (e.g., sensors, actuators, wireless transmitters) have been invented and introduced in many different fields, among which are health care, environmental and structural monitoring, the Internet of things, wireless transmission, security, and nanorobotics, among others.[420,421] These devices generally require only small-scale power (μW to mW)[422] and traditional approaches (i.e., batteries) but present several drawbacks, including the problematic implementation of wireless sensor networks with a huge number of distributed sensor nodes[423] or issues related to recycling.[421,424] This directly calls for the development of sustainable, maintenance-free and self-sufficient power generators that can ideally harvest energy from the environment and be integrated into such devices.

Almost every environment has an abundance of all sorts of energy: thermal, mechanical, solar, chemical, etc. Among these, mechanical vibrations may exist in most of the environments in which a power generator can be placed. Conventional power production is obtained through electromagnetic alternators based on Faraday's law of induction. However, these types of power generation technologies can only harvest high-frequency mechanical energies efficiently.[425] This means that a broad range of energy sources in the environment (e.g., water waves, human body motion, thermal vibrations) cannot be effectively exploited through conventional electromagnetic generators (EMGs).[422]

To effectively convert these different small-scale energies into an electrical output, Wang and Song proposed the first nanogenerator (NG) in 2006.[426] The idea behind this device was based on the piezoelectric effect (i.e., the accumulation of electric charge in response to an applied mechanical stress), and it was made of a zinc oxide nanowire array. A few years later, Wang and co-workers presented the first NG based on the triboelectric effect.[420] The triboelectric effect (or triboelectric charging) is a phenomenon that leads to the formation of charge separation between certain materials after they come into frictional contact. This effect is very common in everyday life and has been known for a long time (almost everybody has felt a small electrical shock after walking across a carpet and then touching a metallic surface). In general, both in scientific and in technological applications, this effect is considered to be negative.

The operation of triboelectric nanogenerators (TENGs) is based on triboelectrification and electrostatic induction, described by Maxwell's displacement current and change in surface polarization.[427] The power density of TENGs is related to the charge density produced in tribological conditions; this led researchers to investigate the role that bulk and surface structural composition and geometry have in the tribocharge formation, together with the related dynamic features. The distinct abilities for attracting electrons of the two triboelectric surfaces result in a transfer of electrostatic charges from one surface to the other. When one triboelectric layer is displaced, the movement of charges breaks the original electrostatic balance, resulting in a potential difference being built between the two electrodes. A current through an external load can then be driven by such potential difference to rebalance the electrostatic status. Therefore, under periodical mechanical triggering, an alternating current (AC) output can be obtained via the TENG, and its functionality is characterized by the voltage between the electrodes, the charge transferred between electrodes, and the relative displacement between triboelectric layers.

13.1. Available Setups for Triboelectric Nanogenerators.

Currently, four different working modes have been identified:[422,423] vertical contact separation (CS), lateral sliding (LS), single electrode (SE), and freestanding triboelectric layer (FT).

All modes are schematically represented in Figure 25. CS-mode TENGs are triggered by the process of contact and separation of two triboelectric layers,[420] while TENGs operating in LS mode exploit the relative sliding between layers.[428] They basically differ in the kind of tribological contact exploited (vertical vs sliding). Both modes suffer from the common disadvantage that the triboelectric layers must be interconnected with an external circuit. Such a configuration might limit the application of TENGs, when one aims to harvest energy from free-moving objects. To solve this issue, SE- and FT-mode TENGs have been proposed, in which a tribolayer is simply replaced by an electrode.[429] In particular, the FT mode has been used for various high-output TENGs with record both in the maximum power output and energy conversion efficiency.[430]

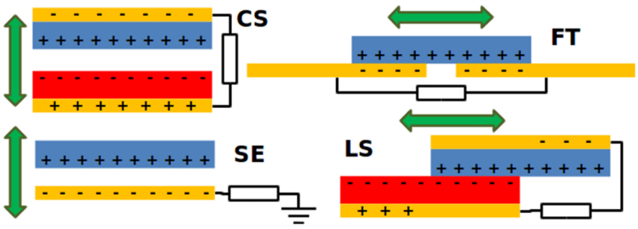

Figure 25. Four basic operation modes for TENGs: contact separation (CS), freestanding triboelectric-layer (FT), single electrode (SE), and lateral sliding (LS). Blue and red boxes represent the tribolayers, while electrodes are drawn in yellow.

The intensity of the triboelectric effect is ruled by the nature of the materials that come into contact. So far, polymers (which contain a naturally present dipole[422]) have been mostly used as tribolayers,[431] especially in implantable TENGs for biomedical applications.[432] Common examples of polymer materials are poly(dimethylsiloxane) (PDMS),[433] poly(tetrafluoroethylene),[428] poly(vinylidene fluoride),[431] fluorinated ethylene propylene,[434] polyimide,[435] and lignin.[436] Typical values of output voltage and current density for such materials are in the order of 1−10 V and from 10^{-3} to 10^{-1} A·m^{-2}, respectively.[423] Recently, graphene has also been used as triboelectric material in TENGs, reporting values for output voltage and current of 5 V and 5×10^{-3} A·m^{-2}, respectively.[437] In addition to this, two-dimensional materials have also gained attention as triboactive candidates for TENGs.[422,437,438]

Nowadays, the choice of materials for novel TENG setups is made easier thanks to the availability of empirical lists of materials ordered by their capability of becoming tribocharged (the so-called *triboelectric series*).[439] Unfortunately, the studies on triboelectric series are sparse, and they do not provide an absolute assessment of the material performance. Making current triboelectric series both quantitative and more extended would be a welcomed progress. For achieving this aim, large-scale databases and computational resources (e.g., NOMAD[440] and AiiDA[441]) may be of crucial importance. Moreover, since the process of charge transfer in TENGs is an interfacial phenomenon, it is obvious that the characteristics of the surface are critical for the performance of the device. The effects on the signal output of the presence of impurities and/or oxides, the surface roughness, the geometry of the contact surfaces, or even the type of pretreatment during fabrication have already been highlighted.[442] This means that materials that are considered identical according to bulk analysis may display completely different microscopic surface properties. Attempts have already been made for enhancing the surface charge density by plasma[443] and laser treatment.[444]

By design, TENGs are meant to be used to harvest energy in various environments. It is therefore crucial to know the effect that the tribological conditions (e.g., contact pressure, temperature, sliding speed) can have on the TENG performance. For example, SE and FT modes can operate in open air and, thus, are subject to different pressures and atmosphere compositions. It was found that, under the same mechanical excitation, the generated charge of a PDMS-based TENG increased more than 20% when the relative humidity was decreased from 90% to 10% at ambient pressure. However, the interpretation of such an effect is not trivial, since a worsening of the performance is observed when the air pressure decreases from atmospheric pressure to 50 Torr in dry conditions.[445] In other studies, the influence of the temperature on the output performance of TENGs was investigated experimentally and supported by atomistic simulations.[446]

13.2. Triboelectric Nanogenerator Upscale. Recently, efforts have also been devoted to upscaling triboelectric nanogenerators, mainly by integrating single TENG units into a network. This was done to harvest low-frequency wave energy in oceans (the so-called blue energy), as a rich resource for large-scale clean-energy generation.[422,424,447] However, as mentioned before, harsh environmental conditions, such as humidity, have shown to significantly affect the performance of NGs.[448] One method that has proven to be promising is a hybrid approach in which conventional principles (i.e., EMGs) are combined with NGs, leading to the so-called *packaging*.[449] More specifically, in this approach the TENG is made waterproof by placing it within an isolating device, thus preventing any unwanted environmental interactions. Subsequently, an EMG is wrapped around, creating an indirect driving force on the mobile part of the TENG using its magnets. It has been shown that this approach can significantly improve the performance of TENGs.[447] First of all, this is because EMG and TENG operate in different frequency ranges, and, by combining both, one can significantly enlarge the working range.[449] Second, both vibrations and rotational motions can now be exploited for the generation of electricity. This is especially relevant for harvesting blue energy, which is characterized by a high irregularity and broad ranges of both frequencies and amplitudes. This novel design principle allows one to up-scale and go beyond the current efficiency of energy harvesting of these multivariate types of energies.[447]

13.3. Back to Nanoscale. A common issue of the above-mentioned TENGs is that frictional energy is converted into an AC output, which is unsuitable for large-impact applications such as light-emitting diodes, electronic watches, and mobile phones. Current rectification is achieved by a supplementary technological effort: switching circuits, combining TENGs with storage systems, rotating-disk configurations, or double-wheel designs have to be used to convert alternating to direct current (DC).[424] Moreover, the current density is limited due to the high impedance, if polymer-based systems are used.[450]

Recently, it has been shown that a DC current can be generated by direct sliding of a platinum-coated silicon AFM tip over a molybdenum disulfide thin film deposited on a substrate.[451] In addition, this setup also produced a maximum value of current density that is several orders of magnitude greater than the usually achievable range. In such a system, carrier flow is attributed to the direct electronic excitation at the interface followed by diffusion-drift conduction;[438] such excitation produces electron−hole pairs, triboluminescence, and exolectrons under tribological conditions.[452] However, no relation among the chemical composition of the frictional surfaces, the tribological conditions (i.e., temperature, normal load, and sliding velocity), and the current density and voltage have been clearly identified yet.

To conclude this section on TENGs, it is worth mentioning the Kelvin probe force microscopy (KPFM),[453] an experimental technique that can provide unique information about the tribocharging of materials at the nanoscale. Only recently researchers started to use this technique in combination with AFM for studying phenomena and properties related to the triboelectric effect.[454] However, it is expected that, in the coming years, the impact of this combination of techniques will bring significant contributions to the field. Another benefit of the KPFM/AFM approach is that the accessible time and size scales match very well with those available in classical molecular dynamics simulations.[455] Such computational tools are in fact suitable for interpreting experimental data, and especially for characterizing the effect of the tribological conditions and/or the nanostructure of the tribosurfaces. Despite the fact that classical tools can successfully simulate system sizes up to hundreds of thousands of atoms on the microsecond time scale, they cannot provide direct information about the electronic structure. However, hybrid (also called multiscale) approaches can be employed. For example, one can perform classical molecular dynamics simulations, to assess the tribological response of the material, and then use the configurations sampled in tribological conditions for a subsequent deeper analysis by means of ab initio techniques. Another promising tool is represented by the hybrid quantum mechanics/molecular mechanics (QM/MM) scheme, where the two levels of description are actually accessible at the same time within a single simulation.

13.4. Outlook. From the brief review given above, one can understand that, even though the computational tools for deepening our understanding of the phenomena are already in place, there is still a huge amount of work to be done. In particular, studies so far mainly dealt with polymer materials and the employment of nanostructures such as nanowires (the latter mostly for piezoelectric-based devices).[456] Moreover, the effect of the normal load on the TENG output performance has not yet been extensively studied.[457] The analysis of the hysteretic behavior of the output showed that a low contact force applied before a high one can enhance the charge transfer and consequently the performance of the device. This result is due to a dependence of the charge generation on the history of the forces applied, and such a phenomenon might be exploited to improve the operational performance of TENGs. Yet, the influence of ambient parameters such as humidity, temperature, and pressure on the hysteresis behavior needs to be further analyzed, if one wants to find ways to customize TENGs in various environments.

Important questions related to these aspects are still open. For example, how do tribological conditions affect the surface charge density, considered as the golden standard for assessing the overall performance of any NG?[448] Or how can the choice for certain materials improve durability but also reduce toxicity?

To sum up, we presented an emerging topic that directly links tribology and energy harvesting. It is expected that advances in this field will have a significant socioeconomic impact. Thanks to simulation approaches, we expect to see a vast enlargement of the list of materials used within the coming years. Because of their superior mechanical properties, inorganic materials are promising candidates for the selection of novel triboactive materials. This, in our opinion, is particularly likely to happen, considering the preliminary results already available in the literature.[437,438,451,458−463]

14. SUMMARY

The fast advance of the contemporary technology requires the improvement of existing materials and the discovery of new ones. In this perspective, nanostructured materials are the promising future for the creation of the next-generation technology. First-principle calculations are the basic starting point to obtain a good estimation of fundamental properties such as electronic configurations, magnetic orderings, structural characteristics, optical properties, and eventual coupling among these. Massive automation of such simulations would help to build a high-quality materials database to be exploited in “smart” systems (e.g., machine learning, neural networks), capable to identify existing or new materials with selected properties. However, a common standard that ensures the reliability of the results without loss of accuracy is still missing. The main effort to determine maps of materials properties (i.e., databases) is the identification of multiparameters descriptors. Despite SISSO being a valid engine to determine such descriptors, the approach is currently limited to scalar features, and the next step is to develop a systematic strategy to build environment-dependent features to be used as candidates in the feature space. Open-source projects that share materials data are the most effective means to obtain a rapid expansion of the databases. Machine-learning-based tools have already become popular for the purpose of predicting materials properties, thanks to the sharing paradigm. However, the quality of the database is crucial to obtain appropriate answers: unbalanced number of members in a family of materials could lead to systematic errors that must be accounted for. Data visualization techniques could help to identify such errors and guide the correction of the predicting model.

Besides high-throughput simulation machineries, massive ab initio molecular dynamics and meta-dynamics techniques are another efficient tool to explore and design material properties, especially when chemical reactions are to be taken into account. Nevertheless, the high cost of such kinds of simulations is still a drawback, and statistical methods like Monte Carlo-based ones represent a promising alternative to overcome such limitation. Another opportunity is the use of ad hoc descriptors, which can facilitate the characterization of specific processes and go at the same pace with the extension of existing theoretical frameworks or the development of new ones. This is the case of the specific applications discussed here such as the dendrite growth in batteries, vapochromic responses to small-molecule analytes, photoactivated linkage isomerism, prevention of He embrittlement in containment materials in nuclear reactors, thermoelectric figure of merit, metalized ferroelectrics, magneto-optical Kerr effect, and tribocharge generation. In these cases, the descriptors have been proposed based on physical reasoning rather than from statistical observations of gathered data.

From our perspective, atomistic simulations, automated modeling, and experimental techniques are rapidly developing and becoming more and more widely available. The mutual integration between theory and experiment turns out to be mandatory to significatively boost the advance of the scientific knowledge and to unveil new physical insights, which will ultimately lead to the design of novel functional materials with tunable properties meeting contemporary challenges.

■ AUTHOR INFORMATION

Corresponding Authors

*E-mail: danilo.puggioni@northwestern.edu. (D.P.)
*E-mail: remedios.cortese@unipa.it. (R.C.)
*E-mail: cammaant@fel.cvut.cz. (A.C.)

ORCID

Aleix Comas-Vives: 0000-0002-7002-1582
Naresh S. Dalal: 0000-0002-9996-6918
Alessio Filippetti: 0000-0002-9144-7005
Cesare Franchini: 0000-0002-7990-2984
Luca M. Ghiringhelli: 0000-0001-5099-3029
Axel Groß: 0000-0003-4037-7331
Shunbo Hu: 0000-0003-0472-0999
Janice L. Musfeldt: 0000-0002-6241-823X
Paolo Nicolini: 0000-0003-1324-7566
Rossitza Pentcheva: 0000-0002-4423-8980
Wei Ren: 0000-0001-7317-3867
Francesco Ricci: 0000-0002-2677-7227
Andrea Urru: 0000-0002-5602-3063
Paolo Vavassori: 0000-0002-4735-6640
Danilo Puggioni: 0000-0002-2128-4191
Remedios Cortese: 0000-0002-7232-8916
Antonio Cammarata: 0000-0002-5691-0682

Present Address

◀A.U.: International School for Advanced Studies (SISSA), Via Bonomea 265, 34136 Trieste, Italy.

Author Contributions

The present Viewpoint was written thanks to the contribution of all authors. Here in the following, the name of each section together with the initials of the authors contributing to it are reported for reader's convenience. "Predicting the band gap of complex materials: computational methods and procedures": C.F. "Data-driven materials science: building maps of materials properties": L.M.G. "Identifying error in machine learning models": T.D.S., K.K. "Accelerated ab initio molecular dynamics applied to the simulation of heterogeneous catalysis": L.F., A.C.-V. "Predictive description of catalytic systems using microkinetic modeling": M.V. "Atomic design principle for safer battery materials": A.G. "Responsive molecular solids": J.M.S. "Materials for nuclear reactors": T.P., H.S.S. "Novel mechanisms for improved oxide thermoelectrics explored from first-principles": B.G., R.P. "Polar, ferroelectric and multiferroic metals: three case studies": V.F., A.F., A.U., H.J.Z., J.I. "Electric Magneto-Optical properties in multi-functional hybrid materials": K.Y., F.F., S.H., W.R., F.R., P.V., J.M., N.D., H.W., A.S. "Tribology as a novel field for electricity generation": P.N., A.C., F.B., V.E.P.C. Finally, A.C., R.C., and D.P. conceptualized the work, composed the manuscript, and supervised the merging of all the contributions.

Notes

The authors declare no competing financial interest.

Biographies

Remedios Cortese collaborates with the University of Palermo and is part of the Group of Computational Chemistry of Palermo. She got degree in Chemistry and a Ph.D. in Chemical Science, both at the University of Palermo. Her scientific research is focused on the modellization, with DFT-based methods, of catalyzed reaction mechanisms concerning industrially relevant substrates.

Danilo Puggioni is an Assistant Research Professor in the Materials Science and Engineering Department at the Northwestern University. He holds a Laurea in Physics and a Ph.D. in Condensed Matter Physics, both from Università di Cagliari, Italy. Danilo joined the Northwestern University after completing postdoctoral work at Drexel University. Danilo uses first-principles theoretical techniques to understand the structural, electronic, magnetic, and optical properties of complex oxides.

After obtaining his Ph.D. in Physics at the Università degli Studi di Palermo (Italy), Antonio Cammarata moved to Philadelphia (U.S.) to work as a postdoctoral researcher at Drexel University. He then joined the Advanced Materials Group at the Department of Control Engineering of Czech Technical University in Prague (Czech Republic), where he is currently appointed as an Assistant Professor. His research interests include energy production in fuel cells, charge-ordering in perovskites, hybrid-improper ferroelectricity, nonlinear optically active materials, nanotribology, and electron−phonon and phonon−phonon coupling, among others.

■ ACKNOWLEDGMENTS

A.C., P.N., and H.S.S. acknowledge support of this work by the Czech Science Foundation (Project Nos. 17-24164Y, 16-11516Y, and 17-17921S), by Novel nanostructures for engineering applications No. CZ.02.1.01/0.0/0.0/16_026/0008396, and by The Ministry of Education, Youth and Sports from the Large Infrastructures for Research, Experimental Development and Innovations project "IT4Innovations National Supercomputing Center−LM2015070". The work of A.G. contributes to the research performed at Center for Electrochemical Energy Storage Ulm-Karlsruhe. J.M.S. is grateful to the UK Engineering and Physical Sciences Research Council for support (Grant Nos. EP/K004956/1 and EP/P007821/1) and to the Univ. of Manchester for the award of a Presidential Fellowship. Work at Tennessee (J.L.M.) is supported by NSF DMR-1707846. C.F. thanks P. Liu, J. He, and G. Kresse for the long-standing collaboration on the topic discussed in this contribution. This work was supported by the Austrian Science Fund (FWF) within the SFB ViCoM (Grant No. F41) and by the joint Indian Department of Science and Technology-FWF Project INDOX (I1490−N19). T.D.S. and S.K.K. gratefully acknowledge support from National Science Foundation through CAREER Award No. 1651668. D.P. was supported by the Army Research Office under W911NF-15-1-0017. The work of F.B. and V.E.P.C. has received funding from the European Union's Horizon 2020 research and innovation programme under Grant No. 721642: SOLUTION. L.M.G. acknowledges M. Scheffler, the main driving force behind all the works and activities presented in this contribution and all the people that contributed to the specific projects. For the SISSO development: R. Ouyang, E. Ahmetcik, and S. Curtarolo. For the perovskite classification: C. J. Bartel, C. Sutton, B. R. Goldsmith, and C. B. Musgrave. L.M.G. also acknowledges all the PIs that made the NOMAD Laboratory possible, besides M. Scheffler who is the coordinator of the Centre of Excellence: A. Rubio, R. Nieminen, F. Illas, D. Frenkel, C. Draxl, A. De Vita, K. Thygesen, K. Koski, S. Heinzel, J. M. Cela, D. Kranzlmüller, C. Clissman. The SISSO project has received funding from the European Union's Horizon 2020 research and innovation program (No. 676580: The NOMAD Laboratory—a European Center of Excellence and No. 740233: TEC 1p) and from the Berlin Big-Data Center (BBDC, No. 01IS14013E). B.G. and R.P. acknowledge funding by the German Research Foundation (Deutsche Forschungsgemeinschaft, DFG) within CRC/TRR 80, Project No. G8, and computing time at magnitUDE granted by the Center for Computational Sciences and Simulation of the Univ. of Duisburg-Essen (DFG Grant Nos. INST 20876/209-1 FUGG and No. INST 20876/243-1 FUGG). V.F. acknowledges support by Univ. di Cagliari, Fondazione di Sardegna, Regione Autonoma Sardegna via Progetto biennale di ateneo 2016 *Multiphysics approach to thermoelectricity*, and by CINECA via ISCRA grants. T.P. acknowledges support by the Centre for Advanced Photovoltaics (CZ.02.1.01/0.0/0.0/15_003/0000464). A.S. thanks the High End Foreign Expert program, Shanghai Eastern Scholar Chair Professor program, and Y. Qi for kind help in making the figures. P.V. acknowledges support from the Spanish Ministry of Economy, Industry and Competitiveness under the Maria de Maeztu Units of Excellence Programme−MDM-2016-0618. A.C.-V. acknowledges the financial support from the Spanish MEC and the European Social Fund (Grant RyC-2016-19930). L.F. thanks ETH Zurich (Research Grant ETH42 14-1) for financial support. A.F. thanks "Progetti biennali d'Ateneo Finanziati dalla Fondazione di Sardegna 2017" (project n. F71I17000170002), and Project PRIN 2017 "TOPSPIN", funded by Italian Ministry of University and Research. A.C., D.P., and R.C. thankfully acknowledge the DiFC of the University of Palermo for funding the "Atomic-scale design protocols towards energy, electronic, catalysis and sensing applications" Symposium of the EMRS 2018 Fall meeting.

■ REFERENCES

(1) Rogers, C.; Barker, D.; Jaeger, C. Introduction to Smart Materials and Structures, Proceedings of U.S. Army Research Office Workshop on *Smart Materials, Structures and Mathematical Issues*; Rogers, C. A., Ed.; Virginia Polytechnic Institute & State University. Technomic Publishing Co., Inc., September 15−16, 2016; pp 17−28.

(2) Hohenberg, P.; Kohn, W. Inhomogeneous Electron Gas. *Phys. Rev.* **1964**, *136*, B864.

(3) Kohn, W.; Sham, L. J. Self-Consistent Equations Including Exchange and Correlation Effects. *Phys. Rev.* **1965**, *140*, A1133.

(4) Hubbard, J.; Flowers, B. H. Electron correlations in narrow energy bands. *Proceedings of the Royal Society of London. Series A. Mathematical and Physical Sciences* **1963**, *276*, 238.

(5) Heyd, J.; Scuseria, G. E.; Ernzerhof, M. Hybrid functionals based on a screened Coulomb potential. *J. Chem. Phys.* **2003**, *118*, 8207−8215.

(6) Kim, K.; Jordan, K. D. Comparison of Density Functional and MP2 Calculations on the Water Monomer and Dimer. *J. Phys. Chem.* **1994**, *98*, 10089−10094.

(7) Stephens, P. J.; Devlin, F. J.; Chabalowski, C. F.; Frisch, M. J. Ab Initio Calculation of Vibrational Absorption and Circular Dichroism Spectra Using Density Functional Force Fields. *J. Phys. Chem.* **1994**, *98*, 11623−11627.

(8) Aryasetiawan, F.; Gunnarsson, O. The GW method. *Rep. Prog. Phys.* **1998**, *61*, 237.

(9) Salpeter, E. E.; Bethe, H. A. A Relativistic Equation for Bound-State Problems. *Phys. Rev.* **1951**, *84*, 1232.

(10) He, J.; Franchini, C. Assessing the performance of self-consistent hybrid functional for band gap calculation in oxide semiconductors. *J. Phys.: Condens. Matter* **2017**, *29*, 454004.

(11) Nunes, R. W.; Gonze, X. Berry-phase treatment of the homogeneous electric field perturbation in insulators. *Phys. Rev. B: Condens. Matter Mater. Phys.* **2001**, *63*, 155107.

(12) Ergönenc, Z.; Kim, B.; Liu, P.; Kresse, G.; Franchini, C. Converged GW quasiparticle energies for transition metal oxide perovskites. *Phys. Rev. Materials* **2018**, *2*, No. 024601.

(13) Chen, W.; Miceli, G.; Rignanese, G.-M.; Pasquarello, A. Nonempirical dielectricdependent hybrid functional with range separation for semiconductors and insulators. *Phys. Rev. Materials* **2018**, *2*, No. 073803.

(14) Grüneis, A. In *Handbook of Materials Modeling*; Andreoni, W., Yip, S., Eds.; Springer International Publishing, 2018; DOI: 10.1007/978-3-319-42913-7_90-2.

(15) Bokdam, M.; Sander, T.; Stroppa, A.; Picozzi, S.; Sarma, D.; Franchini, C.; Kresse, G. Role of polar phonons in the photo excited state of metal halide perovskites. *Sci. Rep.* **2016**, *6*, 28618.

(16) Sander, T.; Maggio, E.; Kresse, G. Beyond the Tamm-Dancoff approximation for extended systems using exact diagonalization. *Phys. Rev. B: Condens. Matter Mater. Phys.* **2015**, *92*, No. 045209.

(17) Liu, P.; Kim, B.; Chen, X.-Q.; Sarma, D. D.; Kresse, G.; Franchini, C. Relativistic GW+BSE study of the optical properties of Ruddlesden-Popper iridates. *Phys. Rev. Materials* **2018**, *2*, No. 075003.

(18) Hirata, S.; Head-Gordon, M. Time-dependent density functional theory within the Tamm−Dancoff approximation. *Chem. Phys. Lett.* **1999**, *314*, 291.

(19) https://materials.springer.com.

(20) Jain, A.; Hautier, G.; Moore, C. J.; Ong, S. P.; Fischer, C. C.; Mueller, T.; Persson, K. A.; Ceder, G. A high-throughput infrastructure for density functional theory calculations. *Comput. Mater. Sci.* **2011**, *50*, 2295−2310.

(21) Curtarolo, S.; Hart, G. L. W.; Setyawan, W.; Mehl, M. J.; Jahnátek, M.; Chepulskii, R. V.; Levy, O.; Morgan, D. *AFLOW: software for high-throughput calculation of material properties*, http://materials.duke.edu/aflow.html 2010.

(22) Saal, J. E.; Kirklin, S.; Aykol, M.; Meredig, B.; Wolverton, C. Materials Design and Discovery with High-Throughput Density Functional Theory: The Open Quantum Materials Database (OQMD). *JOM* **2013**, *65*, 1501−1509.

(23) Wilkinson, M. D.; et al. The FAIR Guiding Principles for scientific data management and stewardship. *Sci. Data* **2016**, *3*, 160018.

(24) Ghiringhelli, L. M.; Carbogno, C.; Levchenko, S.; Mohamed, F.; Huhs, G.; Lüders, M.; Oliveira, M.; Scheffler, M. Towards efficient data exchange and sharing for big-data driven materials science: metadata and data formats. *npj Computational Materials* **2017**, *3*, 46.

(25) Draxl, C.; Scheffler, M. NOMAD: The FAIR concept for big data-driven materials science. *MRS Bull.* **2018**, *43*, 676−682.

(26) Bartók, A.; Payne, M. C.; Kondor, R.; Csányi, G. Gaussian approximation potentials: The accuracy of quantum mechanics, without the electrons. *Phys. Rev. Lett.* **2010**, *104*, 136403.

(27) Behler, J. Atom-centered symmetry functions for constructing high-dimensional neural network potentials. *J. Chem. Phys.* **2011**, *134*, No. 074106.

(28) Carrete, J.; Mingo, N.; Wang, S.; Curtarolo, S. Nanograined Half-Heusler Semiconductors as Advanced Thermoelectrics: An Ab Initio High-Throughput Statistical Study. *Adv. Funct. Mater.* **2014**, *24*, 7427−7432.

(29) Rajan, K. Materials informatics: The materials "gene" and big data. *Annu. Rev. Mater. Res.* **2015**, *45*, 153−169.

(30) Mueller, T.; Kusne, A. G.; Ramprasad, R. *Reviews in Computational Chemistry;* John Wiley & Sons, Inc, 2016; pp 186−273.

(31) Kim, C.; Pilania, G.; Ramprasad, R. From organized high-throughput data to phenomenological theory using machine learning: the example of dielectric breakdown. *Chem. Mater.* **2016**, *28*, 1304−1311.

(32) Faber, F. A.; Lindmaa, A.; von Lilienfeld, O. A.; Armiento, R. Machine Learning Energies of 2 Million Elpasolite (ABC_2D_6) Crystals. *Phys. Rev. Lett.* **2016**, *117*, 135502.

(33) Takahashi, K.; Tanaka, Y. Materials informatics: a journey towards material design and synthesis. *Dalton Trans.* **2016**, *45*, 10497−10499.

(34) Bartók, A.; De, S.; Poelking, C.; Bernstein, N.; Kermode, J.; Csányi, G.; Ceriotti, M. Machine learning unifies the modeling of materials and molecules. *Sci. Adv.* **2017**, *3*, 1701816.

(35) Goldsmith, B. R.; Boley, M.; Vreeken, J.; Scheffler, M.; Ghiringhelli, L. M. Uncovering structure-property relationships of materials by subgroup discovery. *New J. Phys.* **2017**, *19*, No. 013031.

(36) Pham, T. L.; Nguyen, N. D.; Nguyen, V. D.; Kino, H.; Miyake, T.; Dam, H. C. Learning structure-property relationship in crystalline materials: A study of lanthanide−transition metal alloys. *J. Chem. Phys.* **2018**, *148*, 204106.

(37) Ziletti, A.; Kumar, D.; Scheffler, M.; Ghiringhelli, L. M. Insightful classification of crystal structures using deep learning. *Nat. Commun.* **2018**, *9*, 2775.

(38) Sutton, C.; Ghiringhelli, L. M.; Yamamoto, T.; Lysogorskiy, Y.; Blumenthal, L.; Hammerschmidt, T.; Golebiowski, J.; Liu, X.; Ziletti, A.; Scheffler, M. NOMAD 2018 Kaggle Competition: Solving Materials Science Challenges Through Crowd Sourcing. *arXiv preprint arXiv:1812.00085*, 2018.

(39) Ghiringhelli, L. M.; Vybiral, J.; Levchenko, S. V.; Draxl, C.; Scheffler, M. Big data of materials science: Critical role of the descriptor. *Phys. Rev. Lett.* **2015**, *114*, 105503.

(40) Candès, E. J.; Wakin, M. B. An introduction to compressive sampling. *IEEE Signal Proc. Mag.* **2008**, *25*, 21−30.

(41) Nelson, L. J.; Hart, G. L. W.; Zhou, F.; Ozoliņš, V. Compressive sensing as a paradigm for building physics models. *Phys. Rev. B: Condens. Matter Mater. Phys.* **2013**, *87*, No. 035125.

(42) Ghiringhelli, L. M.; Vybiral, J.; Ahmetcik, E.; Ouyang, R.; Levchenko, S. V.; Draxl, C.; Scheffler, M. Learning physical descriptors for materials science by compressed sensing. *New J. Phys.* **2017**, *19*, No. 023017.

(43) Guyon, I.; Elisseeff, A. An introduction to variable and feature selection. *J. Mach. Learn. Res.* **2003**, *3*, 1157−1182.

(44) Ouyang, R.; Curtarolo, S.; Ahmetcik, E.; Scheffler, M.; Ghiringhelli, L. M. SISSO: A compressed-sensing method for identifying the best low-dimensional descriptor in an immensity of offered candidates. *Phys. Rev. Mater.* **2018**, *2*, No. 083802.

(45) Fan, J.; Lv, J. Sure independence screening for ultrahigh dimensional feature space. *J. R. Statist. Soc. B* **2008**, *70*, 849−911.

(46) Tibshirani, R. Regression shrinkage and selection via the lasso. *J. R. Statist. Soc. B* **1996**, *58*, 267−288.

(47) Tropp, J. A.; Gilbert, A. C. Signal recovery from random measurements via orthogonal matching pursuit. *IEEE Trans. Inf. Theory* **2007**, *53*, 4655−4666.

(48) Pati, Y. C.; Rezaiifar, R.; Krishnaprasad, P. S. *The Twenty-Seventh Asilomar Conference: Signals, Systems and Computers;* IEEE, 1993; Vol. *1*, pp 40−44.

(49) Bartel, C. J.; Sutton, C.; Goldsmith, B. R.; Ouyang, R.; Musgrave, C. B.; Ghiringhelli, L. M.; Scheffler, M. New tolerance factor to predict the stability of perovskite oxides and halides. *Science Advances* **2019**, *5*, No. eaav0693.

(50) Ghiringhelli, L. https://th.fhi-berlin.mpg.de/movies/?m=nomadbat, 2017.

(51) Regler, B. https://analytics-toolkit.nomad-coe.eu/tutorial-periodic-table, 2017.

(52) Acosta, C. M.; Ouyang, R.; Fazzio, A.; Scheffler, M.; Ghiringhelli, L. M.; Carbogno, C. Analysis of Topological Transitions in Two-dimensional Materials by Compressed Sensing. *arXiv:1805.10950* 2018.

(53) Bartel, C. J.; Millican, S. L.; Deml, A. M.; Rumptz, J. R.; Tumas, W.; Weimer, A. W.; Lany, S.; Stevanović, V.; Musgrave, C. B.; Holder, A. M. Physical descriptor for the Gibbs energy of inorganic crystalline solids and temperaturedependent materials chemistry. *Nat. Commun.* **2018**, *9*, 4168.

(54) Hwang, J.; Rao, R. R.; Giordano, L.; Katayama, Y.; Yu, Y.; Shao-Horn, Y. Perovskites in catalysis and electrocatalysis. *Science* **2017**, *358*, 751−756.

(55) Duan, C.; Tong, J.; Shang, M.; Nikodemski, S.; Sanders, M.; Ricote, S.; Almansoori, A.; O'Hayre, R. Readily processed protonic ceramic fuel cells with high performance at low temperatures. *Science* **2015**, *349*, 1321−1326.

(56) Cohen, R. E. Origin of ferroelectricity in perovskite oxides. *Nature* **1992**, *358*, 136−138.

(57) Yi, T.; Chen, W.; Cheng, L.; Bayliss, R. D.; Lin, F.; Plews, M. R.; Nordlund, D.; Doeff, M. M.; Persson, K. A.; Cabana, J. Investigating the Intercalation Chemistry of Alkali Ions in Fluoride Perovskites. *Chem. Mater.* **2017**, *29*, 1561−1568.

(58) Correa-Baena, J.-P.; Saliba, M.; Buonassisi, T.; Grätzel, M.; Abate, A.; Tress, W.; Hagfeldt, A. Promises and challenges of perovskite solar cells. *Science* **2017**, *358*, 739−744.

(59) Kovalenko, M. V.; Protesescu, L.; Bodnarchuk, M. I. Properties and potential optoelectronic applications of lead halide perovskite nanocrystals. *Science* **2017**, *358*, 745−750.

(60) Kirkpatrick, S.; Gelatt, C. D.; Vecchi, M. P. Optimization by simulated annealing. *Science* **1983**, *220*, 671−680.

(61) Doye, J. P.; Wales, D. J. Thermodynamics of global optimization. *Phys. Rev. Lett.* **1998**, *80*, 1357.

(62) Goedecker, S. Minima hopping: An efficient search method for the global minimum of the potential energy surface of complex molecular systems. *J. Chem. Phys.* **2004**, *120*, 9911−9917.

(63) Oganov, A. R.; Lyakhov, A. O.; Valle, M. How Evolutionary Crystal Structure Prediction Works−and Why. *Acc. Chem. Res.* **2011**, *44*, 227−237.

(64) Curtarolo, S.; Hart, G. L.; Nardelli, M. B.; Mingo, N.; Sanvito, S.; Levy, O. The high-throughput highway to computational materials design. *Nat. Mater.* **2013**, *12*, 191.

(65) Goldschmidt, V. M. Die gesetze der krystallochemie. *Naturwissenschaften* **1926**, *14*, 477−485.

(66) Li, W.; Wang, Z.; Deschler, F.; Gao, S.; Friend, R. H.; Cheetham, A. K. Chemically diverse and multifunctional hybrid organic−inorganic perovskites. *Nature Reviews Materials* **2017**, *2*, 16099.

(67) Zhang, H.; Li, N.; Li, K.; Xue, D. Structural stability and formability of ABO_3-type perovskitecompounds. *Acta Crystallogr., Sect. B: Struct. Sci.* **2007**, *63*, 812−818.

(68) Li, C.; Lu, X.; Ding, W.; Feng, L.; Gao, Y.; Guo, Z. Formability of ABX_3 (X = F, Cl, Br, I) Halide Perovskites. *Acta Crystallogr., Sect. B: Struct. Sci.* **2008**, *64*, 702−707.

(69) Travis, W.; Glover, E.; Bronstein, H.; Scanlon, D.; Palgrave, R. On the application of the tolerance factor to inorganic and hybrid halide perovskites: a revised system. *Chemical Science* **2016**, *7*, 4548−4556.

(70) Mansouri Tehrani, A.; Oliynyk, A.; Parry, M.; Rizvi, Z.; Couper, S.; Lin, F.; Miyagi, L.; Sparks, T.; Brgoch, J. Machine learning directed search for ultraincompressible, superhard materials. *J. Am. Chem. Soc.* **2018**, *140*, 9844−9853.

(71) Gaultois, M. W.; Oliynyk, A.; Mar, A.; Sparks, T.; Mulholland, G. J.; Meredig, B. Perspective: Web-based machine learning models forreal-times creening of thermoelectric materials properties. *APL Mater.* **2016**, *4*, No. 053213.

(72) Sparks, T.; Gaultois, M. W.; Oliynyk, A.; Brgoch, J.; Meredig, B. Data mining our way to the next generation of thermoelectrics. *Scr. Mater.* **2016**, *111*, 10−15.

(73) Kauwe, S.; Graser, J.; Vazquez, A.; Sparks, T. Machine learning prediction of heat capacity for solid inorganics. *Integrating Materials and Manufacturing Innovation* **2018**, *7*, 43−51.

(74) Graser, J.; Kauwe, S.; Sparks, T. Machine learning and energy minimization approaches for crystal structure predictions: A review and new horizons. *Chem. Mater.* **2018**, *30*, 3601−3612.

(75) Lemonick, S. Is machine learning overhyped? *Chem. Eng. News* **2018**, *96*, 16−20.

(76) Seshadri, R.; Sparks, T. D. Perspective: Interactive material property databases through aggregation of literature data. *APL Mater.* **2016**, *4*, No. 053206.

(77) Michel, K.; Meredig, B. Beyond bulk single crystals: a data format for all materials structure-property-processing relationships. *MRS Bull.* **2016**, *41*, 617.

(78) Kauwe, S.; Yang, Y.; Sparks, T. VIsualization Tool for Atomic modeLs (VITAL): A simple visualization tool for materials predictions. *ChemRxiv* 2019, https://chemrxiv.org/s/cea9ca4196730fae1677.

(79) Kauwe, S. K.; Welker, T.; Sparks, T. D. Extracting Knowledge from DFT: Experimental Band Gap Predictions Through Ensemble Learning. *ChemRXiv* **2018**, DOI: 10.26434/chemrxiv.7236029.v1.

(80) Maaten, L.; Hinton, G. Visualizing data using t-SNE. *Journal of machine learning research* **2008**, *9*, 2579−2605.

(81) Meredig, B.; Antono, E.; Church, C.; Hutchinson, M.; Ling, J.; Paradiso, S.; Blaiszik, B.; Foster, I.; Gibbons, B.; Hattrick-Simpers, J.; Mehta, A.; Ward, L. Can machine learning identify the next high-temperature superconductor? Examining extrapolation performance for materials discovery. *Mol. Syst. Des. Eng.* **2018**, *3*, 819−825.

(82) Nørskov, J. K.; Bligaard, T.; Rossmeisl, J.; Christensen, C. H. Towards the computational design of solid catalysts. *Nat. Chem.* **2009**, *1*, 37.

(83) Nørskov, J. K.; Abild-Pedersen, F.; Studt, F.; Bligaard, T. Density functional theory in surface chemistry and catalysis. *Proc. Natl. Acad. Sci. U. S. A.* **2011**, *108*, 937−943.

(84) Michaelides, A.; Scheffler, M. *Surface and Interface Science;* John Wiley & Sons, Ltd, 2014; pp 13−72 DOI: 10.1002/9783527680535.ch2.

(85) Dumesic, J. *The Microkinetics of heterogeneous catalysis;* ACS professional reference book; American Chemical Society, 1993.

(86) Comas-Vives, A.; Furman, K.; Gajan, D.; Akatay, M. C.; Lesage, A.; Ribeiro, F. H.; Copéret, C. Predictive morphology, stoichiometry and structure of surface species in supported Ru nanoparticles under H_2 and CO atmospheres from combined experimental and DFT studies. *Phys. Chem. Chem. Phys.* **2016**, *18*, 1969−1979.

(87) Piccini, G.; Sauer, J. Effect of Anharmonicity on Adsorption Thermodynamics. *J. Chem. Theory Comput.* **2014**, *10*, 2479−2487.

(88) Piccini, G.; Alessio, M.; Sauer, J. Ab Initio Calculation of Rate Constants for Molecule−Surface Reactions with Chemical Accuracy. *Angew. Chem., Int. Ed.* **2016**, *55*, 5235−5237.

(89) Alessio, M.; Bischoff, F. A.; Sauer, J. Chemically accurate adsorption energies for methane and ethane monolayers on the MgO(001) surface. *Phys. Chem. Chem. Phys.* **2018**, *20*, 9760−9769.

(90) Li, H.; Paolucci, C.; Schneider, W. F. Zeolite Adsorption Free Energies from ab Initio Potentials of Mean Force. *J. Chem. Theory Comput.* **2018**, *14*, 929−938.

(91) Sprowl, L. H.; Campbell, C. T.; Árnadóttir, L. Hindered Translator and Hindered Rotor Models for Adsorbates: Partition Functions and Entropies. *J. Phys. Chem. C* **2016**, *120*, 9719−9731.

(92) Campbell, C. T.; Sprowl, L. H.; Árnadóttir, L. Equilibrium Constants and Rate Constants for Adsorbates: Two-Dimensional (2D) Ideal Gas, 2D Ideal Lattice Gas, and Ideal Hindered Translator Models. *J. Phys. Chem. C* **2016**, *120*, 10283−10297.

(93) Bajpai, A.; Mehta, P.; Frey, K.; Lehmer, A. M.; Schneider, W. F. Benchmark First Principles Calculations of Adsorbate Free Energies. *ACS Catal.* **2018**, *8*, 1945−1954.

(94) Jorgensen, M.; Grönbeck, H. Adsorbate Entropies with Complete Potential Energy Sampling in Microkinetic Modeling. *J. Phys. Chem. C* **2017**, *121*, 7199−7207.

(95) Sun, G.; Jiang, H. Ab initio molecular dynamics with enhanced sampling for surface reaction kinetics at finite temperatures: $CH_2 \rightleftharpoons CH + H$ on Ni(111) as a case study. *J. Chem. Phys.* **2015**, *143*, 234706.

(96) Cammarata, A.; Polcar, T. Overcoming nanoscale friction barriers in transition metal dichalcogenides. *Phys. Rev. B: Condens. Matter Mater. Phys.* **2017**, *96*, No. 085406.

(97) Foppa, L.; Iannuzzi, M.; Copéret, C.; Comas-Vives, A. Adlayer Dynamics Drives CO Activation in Ru-Catalyzed Fischer−Tropsch Synthesis. *ACS Catal.* **2018**, *8*, 6983−6992.

(98) Foppa, L.; Iannuzzi, M.; Copéret, C.; Comas-Vives, A. Facile Fischer−Tropsch Chain Growth from CH2 Monomers Enabled by the Dynamic CO Adlayer. *ACS Catal.* **2019**, *9*, 6571−6582.

(99) Foppa, L.; Iannuzzi, M.; Copéret, C.; Comas-Vives, A. CO methanation on ruthenium flat and stepped surfaces: Key role of H-transfers and entropy revealed by ab initio molecular dynamics. *J. Catal.* **2019**, *371*, 270−275.

(100) Marx, D.; Hutter, J. *Ab Initio Molecular Dynamics: Basic Theory and Advanced Methods;* Cambridge University Press, 2009.

(101) *Modern Methods and Algorithms of Quantum Chemistry: Proceedings;* NIC series; John-von-Neumann-Inst. for Computing, 2000.

(102) Laio, A.; Parrinello, M. Escaping free-energy minima. *Proc. Natl. Acad. Sci. U. S. A.* **2002**, *99*, 12562−12566.

(103) Laio, A.; Rodriguez-Fortea, A.; Gervasio, F. L.; Ceccarelli, M.; Parrinello, M. Assessing the Accuracy of Metadynamics. *J. Phys. Chem. B* **2005**, *109*, 6714−6721.

(104) Barducci, A.; Bonomi, M.; Parrinello, M. Metadynamics. *Wiley Interdisciplinary Reviews: Computational Molecular Science* **2011**, *1*, 826−843.

(105) Iannuzzi, M.; Laio, A.; Parrinello, M. Efficient Exploration of Reactive Potential Energy Surfaces Using Car-Parrinello Molecular Dynamics. *Phys. Rev. Lett.* **2003**, *90*, 238302.

(106) Ensing, B.; De Vivo, M.; Liu, Z.; Moore, P.; Klein, M. L. Metadynamics as a Tool for Exploring Free Energy Landscapes of Chemical Reactions. *Acc. Chem. Res.* **2006**, *39*, 73−81.

(107) Comas-Vives, A.; Stirling, A.; Lledós, A.; Ujaque, G. The Wacker Process: Inneror Outer-Sphere Nucleophilic Addition? New Insights from Ab Initio Molecular Dynamics. *Chem. - Eur. J.* **2010**, *16*, 8738−8747.

(108) Martínez-Suárez, L.; Siemer, N.; Frenzel, J.; Marx, D. Reaction Network of Methanol Synthesis over Cu/ZnO Nanocatalysts. *ACS Catal.* **2015**, *5*, 4201−4218.

(109) Cheng, T.; Xiao, H.; Goddard, W. A. Full atomistic reaction mechanism with kinetics for CO reduction on Cu(100) from ab initio molecular dynamics free-energy calculations at 298 K. *Proc. Natl. Acad. Sci. U. S. A.* **2017**, *114*, 1795−1800.

(110) Gurdal, Y.; Hutter, J.; Iannuzzi, M. Insight into (Co)Pyrphyrin Adsorption on Au(111): Effects of Herringbone Reconstruction and Dynamics of Metalation. *J. Phys. Chem. C* **2017**, *121*, 11416−11427.

(111) Loveless, B. T.; Buda, C.; Neurock, M.; Iglesia, E. CO Chemisorption and Dissociation at High Coverages during CO Hydrogenation on Ru Catalysts. *J. Am. Chem. Soc.* **2013**, *135*, 6107−6121.

(112) Ciobica, I. M.; van Santen, R. A. Carbon Monoxide Dissociation on Planar and Stepped Ru(0001) Surfaces. *J. Phys. Chem. B* **2003**, *107*, 3808−3812.

(113) Reuter, K.; Scheffler, M. Composition, structure, and stability of $RuO_2(110)$ as a function of oxygen pressure. *Phys. Rev. B: Condens. Matter Mater. Phys.* **2001**, *65*, No. 035406.

(114) Micheletti, C.; Laio, A.; Parrinello, M. Reconstructing the Density of States by History-Dependent Metadynamics. *Phys. Rev. Lett.* **2004**, *92*, 170601.

(115) Behler, J. Perspective: Machine learning potentials for atomistic simulations. *J. Chem. Phys.* **2016**, *145*, 170901.

(116) James, A. D. *The Microkinetics of heterogeneous catalysis;* American Chemical Society: Washington, DC, 1993.

(117) Broadbelt, L. J.; Snurr, R. Q. Applications of molecular modeling in heterogeneous catalysis research. *Appl. Catal., A* **2000**, *200*, 23−46.

(118) Stoltze, P. Microkinetic simulation of catalytic reactions. *Prog. Surf. Sci.* **2000**, *65*, 65−150.

(119) Raimondeau, S.; Vlachos, D. G. Recent developments on multiscale, hierarchical modeling of chemical reactors. *Chem. Eng. J.* **2002**, *90*, 3−23.

(120) Salciccioli, M.; Stamatakis, M.; Caratzoulas, S.; Vlachos, D. G. A review of multiscale modeling of metal-catalyzed reactions: Mechanism development for complexity and emergent behavior. *Chem. Eng. Sci.* **2011**, *66*, 4319−4355.

(121) Vlachos, D. G. Multiscale modeling for emergent behavior, complexity, and combinatorial explosion. *AIChE J.* **2012**, *58*, 1314−1325.

(122) Stamatakis, M.; Vlachos, D. G. Unraveling the Complexity of Catalytic Reactions via Kinetic Monte Carlo Simulation: Current Status and Frontiers. *ACS Catal.* **2012**, *2*, 2648−2663.

(123) Vandichel, M.; Moscu, A.; Gronbeck, H. Catalysis at the Rim: A Mechanism for Low Temperature CO Oxidation over Pt_3Sn. *ACS Catal.* **2017**, *7*, 7431−7441.

(124) Jorgensen, M.; Gronbeck, H. First-Principles Microkinetic Modeling of Methane Oxidation over Pd(100) and Pd(111). *ACS Catal.* **2016**, *6*, 6730−6738.

(125) Heard, C. J.; Siahrostami, S.; Gronbeck, H. Structural and Energetic Trends of Ethylene Hydrogenation over Transition Metal Surfaces. *J. Phys. Chem. C* **2016**, *120*, 995−1003.

(126) Bossche, M. V. d.; Gronbeck, H. Methane Oxidation over PdO(101) Revealed by First-Principles Kinetic Modeling. *J. Am. Chem. Soc.* **2015**, *137*, 12035−12044.

(127) Choksi, T.; Greeley, J. Partial Oxidation of Methanol on MoO_3 (010): A DFT and Microkinetic Study. *ACS Catal.* **2016**, *6*, 7260−7277.

(128) Hus, M.; Kopac, D.; Stefancic, N. S.; Jurkovic, D. L.; Dasireddy, V. D. B. C.; Likozar, B. Unravelling the mechanisms of CO_2 hydrogenation to methanol on Cu-based catalysts using first-principles multiscale modelling and experiments. *Catal. Sci. Technol.* **2017**, *7*, 5900−5913.

(129) Foppa, L.; Silaghi, M.-C.; Larmier, K.; Comas-Vives, A. Intrinsic reactivity of Ni, Pd and Pt surfaces in dry reforming and competitive reactions: Insights from first principles calculations and microkinetic modeling simulations. *J. Catal.* **2016**, *343*, 196−207.

(130) Foppa, L.; Margossian, T.; Kim, S. M.; Muller, C.; Copéret, C.; Larmier, K.; Comas-Vives, A. Contrasting the Role of Ni/Al_2O_3 Interfaces in Water−Gas Shift and Dry Reforming of Methane. *J. Am. Chem. Soc.* **2017**, *139*, 17128−17139.

(131) Borght, K.; Toch, K.; Galvita, V. V.; Thybaut, J. W.; Marin, G. B. Information-Driven Catalyst Design Based on High-Throughput Intrinsic Kinetics. *Catalysts* **2015**, *5*, 1948−1968.

(132) Jorgensen, M.; Gronbeck, H. The Site-Assembly Determines Catalytic Activity of Nanoparticles. *Angew. Chem., Int. Ed.* **2018**, *57*, 5086−5089.

(133) Bell, R. P. The Theory of Reactions Involving Proton Transfers. *Proceedings of the Royal Society of London A: Mathematical, Physical and Engineering Sciences* **1936**, *154*, 414−429.

(134) Evans, M. G.; Polanyi, M. Further considerations on the thermodynamics of chemical equilibria and reaction rates. *Trans. Faraday Soc.* **1936**, *32*, 1333−1360.

(135) Hammett, L. P.; Paul, M. A. The Relation between the Rates of Some Acid Catalyzed Reactions and the Acidity Function, H0. *J. Am. Chem. Soc.* **1934**, *56*, 830−832.

(136) Hammer, B.; Norskov, J. K. Why gold is the noblest of all the metals. *Nature* **1995**, *376*, 238.

(137) Liu, P.; Norskov, J. K. Ligand and ensemble effects in adsorption on alloy surfaces. *Phys. Chem. Chem. Phys.* **2001**, *3*, 3814−3818.

(138) Jacobsen, C. J. H.; Dahl, S.; Clausen, B. S.; Bahn, S.; Logadottir, A.; Norskov, J. K. Catalyst Design by Interpolation in the Periodic Table: Bimetallic Ammonia Synthesis Catalysts. *J. Am. Chem. Soc.* **2001**, *123*, 8404−8405.

(139) Norskov, J. K.; Bligaard, T.; Rossmeisl, J.; Christensen, C. H. Towards the computational design of solid catalysts. *Nat. Chem.* **2009**, *1*, 37−46.

(140) Medford, A. J.; Shi, C.; Hoffmann, M. J.; Lausche, A. C.; Fitzgibbon, S. R.; Bligaard, T.; Norskov, J. K. CatMAP: A Software Package for Descriptor-Based Microkinetic Mapping of Catalytic Trends. *Catal. Lett.* **2015**, *145*, 794−807.

(141) Stroppa, A.; Mittendorfer, F.; Andersen, J. N.; Parteder, G.; Allegretti, F.; Surnev, S.; Netzer, F. P. Adsorption and Dissociation of CO on Bare and Ni-Decorated Stepped Rh(553) Surfaces. *J. Phys. Chem. C* **2009**, *113*, 942−949.

(142) Schimka, L.; Harl, J.; Stroppa, A.; Gruneis, A.; Marsman, M.; Mittendorfer, F.; Kresse, G. Accurate surface and adsorption energies from many-body perturbation theory. *Nat. Mater.* **2010**, *9*, 741.

(143) Hammer, B.; Norskov, J. K. Electronic factors determining the reactivity of metal surfaces. *Surf. Sci.* **1995**, *343*, 211−220.

(144) Greeley, J.; Norskov, J. K. A general scheme for the estimation of oxygen binding energies on binary transition metal surface alloys. *Surf. Sci.* **2005**, *592*, 104−111.

(145) Stroppa, A.; Kresse, G. The shortcomings of semi-local and hybrid functionals: what we can learn from surface science studies. *New J. Phys.* **2008**, *10*, No. 063020.

(146) Stroppa, A.; Mittendorfer, F. Tuning the CO Dissociation Barriers by Low Dimensional Surface Alloys. *J. Phys. Chem. C* **2011**, *115*, 21320−21323.

(147) Medford, A. J.; Vojvodic, A.; Hummelshoj, J. S.; Voss, J.; Abild-Pedersen, F.; Studt, F.; Bligaard, T.; Nilsson, A.; Norskov, J. K. From the Sabatier principle to a predictive theory of transition-metal heterogeneous catalysis. *J. Catal.* **2015**, *328*, 36−42.

(148) Filot, I. A. W.; van Santen, R. A.; Hensen, E. J. M. The Optimally Performing Fischer−Tropsch Catalyst. *Angew. Chem., Int. Ed.* **2014**, *53*, 12746−12750.

(149) Busch, M.; Wodrich, M. D.; Corminboeuf, C. Linear scaling relationships and volcano plots in homogeneous catalysis - revisiting the Suzuki reaction. *Chemical Science* **2015**, *6*, 6754−6761.

(150) Rodriguez, J.; Graciani, J.; Evans, J.; Park, J.; Yang, F.; Stacchiola, D.; Senanayake, S.; Ma, S.; Pérez, M.; Liu, P.; Sanz, J.; Hrbek, J. Water-Gas Shift Reaction on a Highly Active Inverse CeOx/Cu(111) Catalyst: Unique Role of Ceria Nanoparticles. *Angew. Chem., Int. Ed.* **2009**, *48*, 8047−8050.

(151) Yang, F.; Graciani, J.; Evans, J.; Liu, P.; Hrbek, J.; Sanz, J. F.; Rodriguez, J. A. CO Oxidation on Inverse CeOx/Cu(111) Catalysts: High Catalytic Activity and Ceria-Promoted Dissociation of O2. *J. Am. Chem. Soc.* **2011**, *133*, 3444−3451.

(152) Schott, V.; Oberhofer, H.; Birkner, A.; Xu, M.; Wang, Y.; Muhler, M.; Reuter, K.; Wöll, C. Chemical Activity of Thin Oxide Layers: Strong Interactions with the Support Yield a New Thin-Film Phase of ZnO. *Angew. Chem., Int. Ed.* **2013**, *52*, 11925−11929.

(153) Kattel, S.; Yan, B.; Yang, Y.; Chen, J. G.; Liu, P. Optimizing Binding Energies of Key Intermediates for CO_2 Hydrogenation to Methanol over Oxide-Supported Copper. *J. Am. Chem. Soc.* **2016**, *138*, 12440−12450.

(154) Reichenbach, T.; Mondal, K.; Jager, M.; Vent-Schmidt, T.; Himmel, D.; Dybbert, V.; Bruix, A.; Krossing, I.; Walter, M.; Moseler, M. Ab initio study of CO_2 hydrogenation mechanisms on inverse ZnO/Cu catalysts. *J. Catal.* **2018**, *360*, 168−174.

(155) Huber, B.; Koskinen, P.; Hakkinen, H.; Moseler, M. Oxidation of magnesia-supported Pd-clusters leads to the ultimate limit of epitaxy with a catalytic function. *Nat. Mater.* **2006**, *5*, 44−47.

(156) Song, W. Y.; Su, Y. Q.; Hensen, E. J. M. A DFT Study of CO Oxidation at the Pd-CeO_2(110) Interface. *J. Phys. Chem. C* **2015**, *119*, 27505−27511.

(157) Vayssilov, G. N.; Lykhach, Y.; Migani, A.; Staudt, T.; Petrova, G. P.; Tsud, N.; Skala, T.; Bruix, A.; Illas, F.; Prince, K. C.; Matolin, V.; Neyman, K. M.; Libuda, J. Support nanostructure boosts oxygen transfer to catalytically active platinum nanoparticles. *Nat. Mater.* **2011**, *10*, 310−315.

(158) Kozlov, S. M.; Neyman, K. M. Effects of electron transfer in model catalysts composed of Pt nanoparticles on CeO2(111) surface. *J. Catal.* **2016**, *344*, 507−514.

(159) Sun, D.; Gu, X.-K.; Ouyang, R.; Su, H.-Y.; Fu, Q.; Bao, X.; Li, W.-X. Theoretical Study of the Role of a Metal−Cation Ensemble at the Oxide−Metal Boundary on CO Oxidation. *J. Phys. Chem. C* **2012**, *116*, 7491−7498.

(160) Pan, Q.; Weng, X.; Chen, M.; Giordano, L.; Pacchioni, G.; Noguera, C.; Goniakowski, J.; Shaikhutdinov, S.; Freund, H.-J.

Enhanced CO Oxidation on the Oxide/Metal Interface: From Ultra-High Vacuum to Near-Atmospheric Pressures. *ChemCatChem* **2015**, *7*, 2620−2627.

(161) Vandichel, M.; Gronbeck, H. CO Oxidation at SnO_2/$Pt_3Sn(111)$ Interfaces. *Top. Catal.* **2018**, *61*, 1458−1464.

(162) Vandichel, M.; Gronbeck, H. A dimer path for CO dissociation on PtSn. *Catal. Sci. Technol.* **2019**, *9*, 695.

(163) Michalak, W. D.; Krier, J. M.; Alayoglu, S.; Shin, J. Y.; An, K.; Komvopoulos, K.; Liu, Z.; Somorjai, G. A. CO oxidation on PtSn nanoparticle catalysts occurs at the interface of Pt and Sn oxide domains formed under reaction conditions. *J. Catal.* **2014**, *312*, 17−25.

(164) Campbell, C. T. The Degree of Rate Control: A Powerful Tool for Catalysis Research. *ACS Catal.* **2017**, *7*, 2770−2779.

(165) Stegelmann, C.; Andreasen, A.; Campbell, C. T. Degree of Rate Control: How Much the Energies of Intermediates and Transition States Control Rates. *J. Am. Chem. Soc.* **2009**, *131*, 8077−8082.

(166) Campbell, C. T. Micro- and macro-kinetics: their relationship in heterogeneous catalysis. *Top. Catal.* **1994**, *1*, 353−366.

(167) Jorgensen, M.; Gronbeck, H. Connection between macroscopic kinetic measurables and the degree of rate control. *Catal. Sci. Technol.* **2017**, *7*, 4034−4040.

(168) Dietze, E. M.; Abild-Pedersen, F.; Plessow, P. N. Comparison of Sintering by Particle Migration and Ripening through First-Principles-Based Simulations. *J. Phys. Chem. C* **2018**, *122*, 26563−26569.

(169) Groß, A. Fundamental Challenges for Modeling Electrochemical Energy Storage Systems at the Atomic Scale. *Top. Curr. Chem.* **2018**, *376*, 17.

(170) Xu, W.; Wang, J.; Ding, F.; Chen, X.; Nasybulin, E.; Zhang, Y.; Zhang, J.-G. Lithium metal anodes for rechargeable batteries. *Energy Environ. Sci.* **2014**, *7*, 513−537.

(171) Wu, F.; Yuan, Y.-X.; Cheng, X.-B.; Bai, Y.; Li, Y.; Wu, C.; Zhang, Q. Perspectives for restraining harsh lithium dendrite growth: Towards robust lithium metal anodes. *Energy Storage Mater.* **2018**, *15*, 148−170.

(172) Medenbach, L.; Bender, C. L.; Haas, R.; Mogwitz, B.; Pompe, C.; Adelhelm, P.; Schröder, D.; Janek, J. Origins of Dendrite Formation in Sodium−Oxygen Batteries and Possible Countermeasures. *Energy Technol.* **2017**, *5*, 2265−2274.

(173) Aurbach, D.; Cohen, Y.; Moshkovich, M. The Study of Reversible Magnesium Deposition by In Situ Scanning Tunneling Microscopy. *Electrochem. Solid-State Lett.* **2001**, *4*, A113.

(174) Jäckle, M.; Groß, A. Microscopic properties of lithium, sodium, and magnesium battery anode materials related to possible dendrite growth. *J. Chem. Phys.* **2014**, *141*, 174710.

(175) Steiger, J.; Richter, G.; Wenk, M.; Kramer, D.; Mönig, R. Comparison of the growth of lithium filaments and dendrites under different conditions. *Electrochem. Commun.* **2015**, *50*, 11−14.

(176) Ehrlich, G.; Hudda, F. G. Atomic view of surface self-diffusion: tungsten on tungsten. *J. Chem. Phys.* **1966**, *44*, 1039.

(177) Schwoebel, R. L.; Shipsey, E. J. Step motion on crystal surfaces. *J. Appl. Phys.* **1966**, *37*, 3682.

(178) Jäckle, M.; Helmbrecht, K.; Smits, M.; Stottmeister, D.; Groß, A. Self-diffusion barriers: possible descriptors for dendrite growth in batteries? *Energy Environ. Sci.* **2018**, *11*, 3400−3407.

(179) Elia, G. A.; Marquardt, K.; Hoeppner, K.; Fantini, S.; Lin, R.; Knipping, E.; Peters, W.; Drillet, J.-F.; Passerini, S.; Hahn, R. An Overview and Future Perspectives of Aluminum Batteries. *Adv. Mater.* **2016**, *28*, 7564−7579.

(180) Parker, J. F.; Chervin, C. N.; Nelson, E. S.; Rolison, D. R.; Long, J. W. Wiring zinc in three dimensions re-writes battery performance-dendrite-free cycling. *Energy Environ. Sci.* **2014**, *7*, 1117−1124.

(181) Parker, J. F.; Chervin, C. N.; Pala, I. R.; Machler, M.; Burz, M. F.; Long, J. W.; Rolison, D. R. Rechargeable nickel-3D zinc batteries: An energy-dense, safer alternative to lithium-ion. *Science* **2017**, *356*, 415−418.

(182) Lin, X.; Dasgupta, A.; Xie, F.; Schimmel, T.; Evers, F.; Groß, A. Exchange processes in the contact formation of Pb electrodes. *Electrochim. Acta* **2014**, *140*, 505−510.

(183) Wang, K.; Pei, P.; Ma, Z.; Chen, H.; Xu, H.; Chen, D.; Wang, X. Dendrite growth in the recharging process of Zinc−air batteries. *J. Mater. Chem. A* **2015**, *3*, 22648−22655.

(184) Davidson, R.; Verma, A.; Santos, D.; Hao, F.; Fincher, C.; Xiang, S.; Van Buskirk, J.; Xie, K.; Pharr, M.; Mukherjee, P.; Banerjee, S. Formation of Magnesium Dendrites during Electrodeposition. *ACS Energy Lett.* **2019**, *4*, 375−376.

(185) Gaissmaier, D.; Fantauzzi, D.; Jacob, T. First principles studies of self-diffusion processes on metallic lithium surfaces. *J. Chem. Phys.* **2019**, *150*, No. 041723.

(186) Magnussen, O. M.; Groß, A. Toward an Atomic-Scale Understanding of Electrochemical Interface Structure and Dynamics. *J. Am. Chem. Soc.* **2019**, *141*, 4777−4790.

(187) Xu, L.; Ho, C.-L.; Liu, L.; Wong, W.-Y. Molecular/polymeric metallaynes and related molecules: Solar cell materials and devices. *Coord. Chem. Rev.* **2018**, *373*, 233−257.

(188) Evans, R. C.; Douglas, P.; Winscom, C. J. Coordination complexes exhibiting room-temperature phosphorescence: Evaluation of their suitability as triplet emitters in organic light emitting diodes. *Coord. Chem. Rev.* **2006**, *250*, 2093−2126.

(189) Kato, M. Luminescent Platinum Complexes Having Sensing Functionalities. *Bull. Chem. Soc. Jpn.* **2007**, *80*, 287−294.

(190) Jain, A.; Ong, S. P.; Hautier, G.; Chen, W.; Richards, W. D.; Dacek, S.; Cholia, S.; Gunter, D.; Skinner, D.; Ceder, G.; Persson, K. A. Commentary: The Materials Project: A materials genome approach to accelerating materials innovation. *APL Mater.* **2013**, *1*, No. 011002.

(191) Williams, J. A. G.; Beeby, A.; Davies, E. S.; Weinstein, J. A.; Wilson, C. An Alternative Route to Highly Luminescent Platinum(II) Complexes: Cyclometalation with N^C^N-Coordinating Dipyridylbenzene Ligands. *Inorg. Chem.* **2003**, *42*, 8609−8611.

(192) Williams, J. A. G. The coordination chemistry of dipyridylbenzene: N-deficient terpyridine or panacea for brightly luminescent metal complexes? *Chem. Soc. Rev.* **2009**, *38*, 1783−1801.

(193) Fuertes, S.; Brayshaw, S. K.; Raithby, P. R.; Schiffers, S.; Warren, M. R. New C^N^C Bis-Cyclometalated Platinum(II) Complexes: Synthesis, Structures, and Photophysical Properties. *Organometallics* **2012**, *31*, 105−119.

(194) Botchway, S. W.; Charnley, M.; Haycock, J. W.; Parker, A. W.; Rochester, D. L.; Weinstein, J. A.; Williams, J. A. G. Time-resolved and two-photon emission imaging microscopy of live cells with inert platinum complexes. *Proc. Natl. Acad. Sci. U. S. A.* **2008**, *105*, 16071−16076.

(195) Grove, L. J.; Rennekamp, J. M.; Jude, H.; Connick, W. B. A New Class of Platinum(II) Vapochromic Salts. *J. Am. Chem. Soc.* **2004**, *126*, 1594−1595.

(196) Bryant, M. J.; et al. A rapidly-reversible absorptive and emissive vapochromic Pt(II) pincer-based chemical sensor. *Nat. Commun.* **2017**, *8*, 1800.

(197) Wadas, T. J.; Wang, Q.-M.; Kim, Y.-j.; Flaschenreim, C.; Blanton, T. N.; Eisenberg, R. Vapochromism and Its Structural Basis in a Luminescent Pt(II) Terpyridine−Nicotinamide Complex. *J. Am. Chem. Soc.* **2004**, *126*, 16841−16849.

(198) Kui, S. C. F.; Chui, S. S.-Y.; Che, C.-M.; Zhu, N. Structures, Photoluminescence, and Reversible Vapoluminescence Properties of Neutral Platinum(II) Complexes Containing Extended π-Conjugated Cyclometalated Ligands. *J. Am. Chem. Soc.* **2006**, *128*, 8297−8309.

(199) Albrecht, M.; Lutz, M.; Spek, A. L.; van Koten, G. Organoplatinum crystals for gastriggered switches. *Nature* **2000**, *406*, 970.

(200) Grove, L. J.; Oliver, A. G.; Krause, J. A.; Connick, W. B. Structure of a Crystalline Vapochromic Platinum(II) Salt. *Inorg. Chem.* **2008**, *47*, 1408−1410.

(201) Murmann, R. K.; Taube, H. The Mechanism of the Formation and Rearrangement of Nitritocobalt(III) Ammines1. *J. Am. Chem. Soc.* **1956**, *78*, 4886−4890.

(202) Penland, R. B.; Lane, T. J.; Quagliano, J. V. Infrared Absorption Spectra of Inorganic Coördination Complexes. VII. Structural Isomerism of Nitro- and Nitritopentamminecobalt(III) Chlorides1a,b. *J. Am. Chem. Soc.* **1956**, *78*, 887−889.

(203) Adell, B. Die Geschwindigkeit der Rückwandlung von bestrahltem festem Nitropentamminkobalt(III) chlorid. *Zeitschrift für anorganische und allgemeine Chemie* **1955**, *279*, 219−224.

(204) Svendsen, H.; Overgaard, J.; Chevallier, M.; Collet, E.; Iversen, B. Photomagnetic Switching of the Complex $[Nd(dmf)_4(H_2O)_3(\mu\text{-}CN)Fe(CN)_5]\cdot H_2O$ Analyzed by Single-Crystal X-Ray Diffraction. *Angew. Chem.* **2009**, *121*, 2818−2821.

(205) Zhang, J.; Zou, Q.; Tian, H. Photochromic Materials: More Than Meets The Eye. *Adv. Mater.* **2013**, *25*, 378−399.

(206) Sylvester, S. O.; Cole, J. M. Solar-Powered Nanomechanical Transduction from Crystalline Molecular Rotors. *Adv. Mater.* **2013**, *25*, 3324−3328.

(207) Carducci, M. D.; Pressprich, M. R.; Coppens, P. Diffraction Studies of Photoexcited Crystals: Metastable Nitrosyl-Linkage Isomers of Sodium Nitroprusside. *J. Am. Chem. Soc.* **1997**, *119*, 2669−2678.

(208) Dynamic single-crystal diffraction studies using synchrotron radiation. *Coord. Chem. Rev.* **2014**, *277−278*, 69−79, , Following Chemical Structures using Synchrotron Radiation.

(209) Hatcher, L. E.; Christensen, J.; Hamilton, M. L.; Trincao, J.; Allan, D. R.; Warren, M. R.; Clarke, I. P.; Towrie, M.; Fuertes, D. S.; Wilson, C. C.; Woodall, C. H.; Raithby, P. R. Steady-State and Pseudo-Steady-State Photocrystallographic Studies on Linkage Isomers of $[Ni(Et_4dien)(\eta^2\text{-}O,ON)(\eta^1\text{-}NO_2)]$: Identification of a New Linkage Isomer. *Chem.−Eur. J.* **2014***20*, 3128−3134, .

(210) Warren, M. R.; Easun, T. L.; Brayshaw, S. K.; Deeth, R. J.; George, M. W.; Johnson, A. L.; Schiffers, S.; Teat, S. J.; Warren, A. J.; Warren, J. E.; Wilson, C. C.; Woodall, C. H.; Raithby, P. R. Solid-State Interconversions: Unique 100% Reversible Transformations between the Ground and Metastable States in Single-Crystals of a Series of Nickel(II) Nitro Complexes. *Chem.−Eur. J.*, **2014***20*5468−5477, .

(211) Hatcher, L. E.; Bigos, E. J.; Bryant, M. J.; MacCready, E. M.; Robinson, T. P.; Saunders, L. K.; Thomas, L. H.; Beavers, C. M.; Teat, S. J.; Christensen, J.; Raithby, P. R. Thermal and photochemical control of nitro−nitrito linkage isomerism in singlecrystals of $[Ni(medpt)(NO_2)(\eta^2\text{-}ONO)]$. *CrystEngComm* **2014**, *16*, 8263−8271.

(212) Bowes, K. F.; Cole, J. M.; Husheer, S. L. G.; Raithby, P. R.; Savarese, T. L.; Sparkes, H. A.; Teat, S. J.; Warren, J. E. Photocrystallographic structure determination of a new geometric isomer of $[Ru(NH_3)4(H_2O)(\eta^1\text{-}OSO)][MeC_6H_4SO_3]_2$. *Chem. Commun.* **2006**, 2448−2450.

(213) Sylvester, S. O.; Cole, J. M. Quantifying Crystallographically Independent Optical Switching Dynamics in Ru SO2 Photoisomers via Lock-and-Key Crystalline Environment. *J. Phys. Chem. Lett.* **2013**, *4*, 3221−3226.

(214) Photo-Induced Linkage Isomerism of Transition Metal Nitrosyl and Dinitrogen Complexes Studied by Photocrystallographic Techniques. *Tetrahedron* **2000**, *56*, 6813−6820, .

(215) Warren, M.; Brayshaw, S.; Johnson, A.; Schiffers, S.; Raithby, P.; Easun, T.; George, M.; Warren, J.; Teat, S. Reversible 100% Linkage Isomerization in a Single-Crystal to Single-Crystal Transformation: Photocrystallographic Identification of the Metastable $[Ni(dppe)(\eta^1\text{-}ONO)Cl]$ Isomer. *Angew. Chem.*, **2009***121*5821−5824, .

(216) Hatcher, L. E. Raising the (metastable) bar: 100$[Pd(Bu_4dien)(\eta^1\text{-}\underline{N}O_2)]^+$ approaches ambient temperature. *CrystEngComm* **2016**, *18*, 4180−4187.

(217) Skelton, J. M.; Crespo-Otero, R.; Hatcher, L. E.; Parker, S. C.; Raithby, P. R.; Walsh, A. Energetics, thermal isomerisation and photochemistry of the linkage-isomer system $[Ni(Et_4dien)(\eta^2\text{-}O,ON)(\eta^1\text{-}NO_2)]$. *CrystEngComm* **2015**, *17*, 383−394.

(218) Skelton, J. M.; Lora da Silva, E.; Crespo-Otero, R.; Hatcher, L. E.; Raithby, P. R.; Parker, S. C.; Walsh, A. Electronic excitations in molecular solids: bridging theory and experiment. *Faraday Discuss.* **2015**, *177*, 181−202.

(219) Hatcher, L. E.; Skelton, J. M.; Warren, M. R.; Stubbs, C.; da Silva, E. L.; Raithby, P. R. Monitoring photo-induced population dynamics in metastable linkage isomer crystals: a crystallographic kinetic study of $[Pd(Bu_4dien)NO_2]BPh_4$. *Phys. Chem. Chem. Phys.* **2018**, *20*, 5874−5886.

(220) Casaretto, N.; Schaniel, D.; Alle, P.; Wenger, E.; Parois, P.; Fournier, B.; Bendeif, E. E.; Palin, C.; Pillet, S. In-house time-resolved photocrystallography on the millisecond timescale using a gated X-ray hybrid pixel area detector. *Acta Crystallogr., Sect. B: Struct. Sci., Cryst. Eng. Mater.* **2017**, *73*, 696−707.

(221) Chater, J. A history of nuclear power. 2004. https://courses.engr.illinois.edu/npre470/sp2018/web/readings/James_Chater_History_nuclear.pdf

(222) IEA *World Energy Outlook 2018;* IEA: Paris, 2018, DOI: 10.1787/weo-2018-en.

(223) Goldberg, S. M.; Rosner, R. *Nuclear Reactors: Generation to Generation;* American Academy of Arts and Sciences, 2011.

(224) *GIF R&D Outlook for Generation IV Nuclear Energy Systems*; GIF, Aug 21, 2009. https://inis.iaea.org/collection/NCLCollectionStore/_Public/43/002/43002386.pdf

(225) Carpenter, G. J. C.; Watters, J. F. Vacancy precipitation in zirconium alloys. *Acta Metall.* **1973**, *21*, 1207−1214.

(226) Griffiths, M. A review of microstructure evolution in zirconium alloys during irradiation. *J. Nucl. Mater.* **1988**, *159*, 190−218.

(227) Onimus, F.; Béchade, J. L. In *Comprehensive Nuclear Materials;* Konings, R. J., Ed.; Elsevier: Oxford, UK, 2012; pp 1−31, DOI: 10.1016/B978-0-08-056033-5.00064-1.

(228) Becquart, C. S.; Domain, C. Migration Energy of He in W Revisited by Ab Initio Calculations. *Phys. Rev. Lett.* **2006**, *97*, 196402.

(229) Zinkle, S. In *Structural Materials for Generation IV Nuclear Reactors;* Yvon, P., Ed.; Woodhead Publishing, 2017; pp 569−594, DOI: 10.1016/B978-0-08-100906-2.00016-1.

(230) Beyerlein, I. J.; Demkowicz, M. J.; Misra, A.; Uberuaga, B. P. Defectinterface interactions. *Prog. Mater. Sci.* **2015**, *74*, 125−210.

(231) Demkowicz, M. J.; Misra, A.; Caro, A. The role of interface structure in controlling high helium concentrations. *Curr. Opin. Solid State Mater. Sci.* **2012**, *16*, 101−108.

(232) Bai, X.-M.; Voter, A. F.; Hoagland, R. G.; Nastasi, M.; Uberuaga, B. P. Efficient Annealing of Radiation Damage Near Grain Boundaries via Interstitial Emission. *Science* **2010**, *327*, 1631−1634.

(233) Demkowicz, M. J.; Hoagland, R. G.; Hirth, J. Interface Structure and Radiation Damage Resistance in Cu-Nb Multilayer Nanocomposite. *Phys. Rev. Lett.* **2008**, *100*, 136102.

(234) Saikia, U.; Sahariah, M. B.; González, C.; Pandey, R. Vacancy assisted He-interstitial clustering and their elemental interaction at fcc-bcc semicoherent metallic interface. *Sci. Rep.* **2018**, *8*, 3884.

(235) Kolluri, K.; Demkowicz, M. J. Formation, migration, and clustering of delocalized vacancies and interstitials at a solid-state semicoherent interface. *Phys. Rev. B: Condens. Matter Mater. Phys.* **2012**, *85*, DOI: 10.1103/PhysRevB.85.205416.

(236) Kolluri, K.; Liu, X.-Y.; Hoagland, R.; Demkowicz, M. Behavior of Vacancies and Interstitials at Semicoherent Interfaces. *JOM* **2013**, *65*, 374.

(237) González, C.; Iglesias, R.; Demkowicz, M. Point defect stability in a semicoherent metallic interface. *Phys. Rev. B: Condens. Matter Mater. Phys.* **2015**, *91*, No. 064103.

(238) Metsanurk, E.; Caro, A.; Tamm, A.; Aabloo, A.; Klintenberg, M. First-principles study of point defects at semicoherent interface. *Sci. Rep.* **2015**, *4*, DOI: 10.1038/srep07567.

(239) Metsanurk, E.; Tamm, A.; Aabloo, A.; Klintenberg, M.; Caro, A. Vacancies at the Cu−Nb semicoherent interface. *Modell. Simul. Mater. Sci. Eng.* **2017**, *25*, No. 025012.

(240) Demkowicz, M.; Thilly, L. Structure, shear resistance and interaction with point defects of interfaces in Cu−Nb nanocomposites synthesized by severe plastic deformation. *Acta Mater.* **2011**, *59*, 7744−7756.

(241) Liu, X.-Y.; Uberuaga, B.; Demkowicz, M.; Germann, T.; Misra, A.; Nastasi, M. Mechanism for recombination of radiation-induced point defects at interphase boundaries. *Phys. Rev. B: Condens. Matter Mater. Phys.* **2012**, *85*, No. 012103.

(242) Snel, J.; Monclús, M. A.; Castillo-Rodríguez, M.; Mara, N.; Beyerlein, I. J.; Llorca, J.; Molina-Aldareguía, J. M. Deformation Mechanism Map of Cu/Nb Nanoscale Metallic Multilayers as a Function of Temperature and Layer Thickness. *JOM* **2017**, *69*, 2214−2226.

(243) Economy, D. R.; Schultz, B. M.; Kennedy, M. S. Impacts of accelerated aging on the mechanical properties of Cu−Nb nanolaminates. *J. Mater. Sci.* **2012**, *47*, 6986−6991.

(244) Zhang, J.; Zhang, P.; Zhang, X.; Wang, R.; Liu, G.; Zhang, G.; Sun, J. Mechanical properties of fcc/fcc Cu/Nb nanostructured multilayers. *Mater. Sci. Eng., A* **2012**, *545*, 118−122.

(245) Sen, H. S.; Polcar, T. Vacancy-interface-helium interaction in Zr-Nb multi-layer system: a first-principles study. *J. Nucl. Mater.*.**2019***51811*

(246) Demkowicz, M. J.; Hoagland, R. G.; Uberuaga, B. P.; Misra, A. Influence of interface sink strength on the reduction of radiation-induced defect concentrations and fluxes in materials with large interface area per unit volume. *Phys. Rev. B: Condens. Matter Mater. Phys.* **2011**, *84*, 104102.

(247) Li, N.; Demkowicz, M.; Mara, N. Microstructure Evolution and Mechanical Response of Nanolaminate Composites Irradiated with Helium at ElevatedTemperatures. *JOM* **2017**, *69*, 2206.

(248) Demkowicz, M. J.; Wang, Y. Q.; Hoagland, R. G.; Anderoglu, O. Mechanisms of He escape during implantation in CuNb multilayer composites. *Nucl. Instrum. Methods Phys. Res., Sect. B* **2007**, *261*, 524−528.

(249) Zhang, X.; Li, N.; Anderoglu, O.; Wang, H.; Swadener, J. G.; Höchbauer, T.; Misra, A.; Hoagland, R. G. Nanostructured Cu/Nb multilayers subjected to helium ion-irradiation. *Nucl. Instrum. Methods Phys. Res., Sect. B* **2007**, *261*, 1129−1132.

(250) Dunn, A.; McPhie, M.; Capolungo, L.; Martinez, E.; Cherkaoui, M. A rate theory study of helium bubble formation and retention in Cu−Nb nanocomposites. *J. Nucl. Mater.* **2013**, *435*, 141−152.

(251) Chen, D.; Li, N.; Yuryev, D.; Baldwin, J.; Wang, Y.; Demkowicz, M. Self-organization of helium precipitates into elongated channels within metal nanolayers. *Science Advances* **2017**, *3*, No. eaao2710.

(252) Bhattacharyya, D.; Demkowicz, M.; Wang, Y.-Q.; Baumer, R.; Nastasi, M.; Misra, A. A Transmission Electron Microscopy Study of the Effect of Interfaces on Bubble Formation in He-Implanted Cu-Nb Multilayers. *Microsc. Microanal.* **2012**, *18*, 152−161.

(253) Hattar, K.; Demkowicz, M.; Misra, A.; Robertson, I.; Hoagland, R. Arrest of He Bubble Growth in Cu-Nb Multilayer Nanocomposites. *Scr. Mater.* **2008**, *58*, 541−544.

(254) González, C.; Iglesias, R. Energetic analysis of He and monovacancies in Cu/W metallic interfaces. *Mater. Des.* **2016**, *91*, 171−179.

(255) Callisti, M.; Karlik, M.; Polcar, T. Bubbles formation in helium ion irradiated Cu/W multilayer nanocomposites: Effects on structure and mechanical properties. *J. Nucl. Mater.* **2016**, *473*, 18−27.

(256) Chen, S.; Liu, B.; Lin, L.; Jiao, G. Microstructural development and helium bubble formation in Cu/W(Re) nanometer multilayer films irradiated by He+ ion. *Nucl. Instrum. Methods Phys. Res., Sect. B* **2015**, *354*, 244−248 26th International Conference on Atomic Collisions in Solids. .

(257) Pacaud, J.; Jaouen, C.; Gladyszewski, G. Irradiation effects in Cu/W multilayers: Ion beam mixing and structural evolution. *J. Appl. Phys.* **1999**, *86*, 4847−4854.

(258) Nelasov, I. V.; Lipnitskii, A. G. The study of Cu/Nb interface diffusion using molecular dynamics simulation. *St. Petersburg Polytechnical University Journal: Physics and Mathematics* **2016**, *2*, 91−95.

(259) Woldt, E.; Jensen, D. J. Recrystallization kinetics in copper: Comparison between techniques. *Metall. Mater. Trans. A* **1995**, *26*, 1717−1724.

(260) Benchabane, G.; Boumerzoug, Z.; Thibon, I.; Gloriant, T. Recrystallization of pure copper investigated by calorimetry and microhardness. *Mater. Charact.* **2008**, *59*, 1425−1428.

(261) Monclús, M. A.; Zheng, S. J.; Mayeur, J. R.; Beyerlein, I. J.; Mara, N. A.; Polcar, T.; Llorca, J.; Molina-Aldareguía, J. M. Optimum high temperature strength of two-dimensional nanocomposites. *APL Mater.* **2013**, *1*, No. 052103.

(262) Primorac, M.-M.; Abad, M. D.; Hosemann, P.; Kreuzeder, M.; Maier, V.; Kiener, D. Elevated temperature mechanical properties of novel ultra-fine grained Cu−Nb composites. *Mater. Sci. Eng., A* **2015**, *625*, 296−302.

(263) Monclús, M. A.; Karlik, M.; Callisti, M.; Frutos, E.; LLorca, J.; Polcar, T.; Molina-Aldareguía, J. M. Microstructure and mechanical properties of physical vapor deposited Cu/W nanoscale multilayers: Influence of layer thickness and temperature. *Thin Solid Films* **2014**, *571*, 275−282 Multilayers 2013. .

(264) Monclús, M. A.; Callisti, M.; Polcar, T.; Yang, L. W.; Molina-Aldareguía, J. M.; LLorca, J. Effect of layer thickness on the mechanical behaviour of oxidationstrengthened Zr/Nb nanoscale multilayers. *J. Mater. Sci.* **2018**, *53*, 5860−5878.

(265) Callisti, M.; Polcar, T. Combined size and texture-dependent deformation and strengthening mechanisms in Zr/Nb nano-multilayers. *Acta Mater.* **2017**, *124*, 247−260.

(266) Callisti, M.; Lozano-Perez, S.; Polcar, T. Structural and mechanical properties of γ-irradiated Zr/Nb multilayer nanocomposites. *Mater. Lett.* **2016**, *163*, 138−141.

(267) Callisti, M.; Karlik, M.; Polcar, T. Competing mechanisms on the strength of ion-irradiated Zr/Nb nanoscale multilayers: Interface strength versus radiation hardening. *Scr. Mater.* **2018**, *152*, 31−35.

(268) Rodgers, D.; Griffiths, M.; Bickel, G.; Buyers, A.; Coleman, C.; Nordin, H.; Lawrence, S. Performance of pressure tubes in CANDU reactors. *CNL Nuclear Review* **2016**, *5*, 1−15.

(269) Lu, Y.; Kotoka, R.; Ligda, J.; Cao, B.; Yarmolenko, S.; Schuster, B.; Wei, Q. The microstructure and mechanical behavior of Mg/Ti multilayers as a function of individual layer thickness. *Acta Mater.* **2014**, *63*, 216−231.

(270) Lu, Y.; Kotoka, R.; Ligda, J.; Cao, B.; Yarmolenko, S.; Schuster, B.; Wei, Q. The microstructure and mechanical behavior of Mg/Ti multilayers as a function of individual layer thickness. *Acta Mater.* **2014**, *63*, 216−231.

(271) He, J.; Liu, Y.; Funahashi, R. Oxide thermoelectrics: The challenges, progress, and outlook. *J. Mater. Res.* **2011**, *26*, 1762−1772.

(272) Hébert, S.; Maignan, A. In *Functional Oxides;* Bruce, D. W., O'Hare, D., Walton, R. I., Eds.; John Wiley & Sons, Ltd: Chichester, UK, 2010 DOI: 10.1002/9780470686072.ch4.

(273) Puggioni, D.; Rondinelli, J. M. Designing a robustly metallic noncenstrosymmetric ruthenate oxide with large thermopower anisotropy. *Nat. Commun.* **2014**, *5*, 3432.

(274) Gorai, P.; Stevanovic, V.; Toberer, E. Computationally guided discovery of thermoelectric materials. *Nat. Rev. Mater.* **2017**, *2*, 17053.

(275) Xing, G.; Sun, J.; Ong, K. P.; Fan, X.; Zheng, W.; Singh, D. J. Perspective: n-type oxide thermoelectrics via visual search strategies. *APL Mater.* **2016**, *4*, No. 053201.

(276) Garrity, K. F. First-principles search for n-type oxide, nitride, and sulfide thermoelectrics. *Phys. Rev. B: Condens. Matter Mater. Phys.* **2016**, *94*, No. 045122.

(277) Lamontagne, L. K.; Laurita, G.; Gaultois, M. W.; Knight, M.; Ghadbeigi, L.; Sparks, T. D.; Gruner, M. E.; Pentcheva, R.; Brown, C. M.; Seshadri, R. High Thermopower with Metallic Conductivity in p-Type Li-Substituted $PbPdO_2$. *Chem. Mater.* **2016**, *28*, 3367−3373.

(278) Okuda, T.; Nakanishi, K.; Miyasaka, S.; Tokura, Y. Large thermoelectric response of metallic perovskites: $Sr_{1-x}La_xTiO_3(0 <\sim x <\sim 0.1)$. *Phys. Rev. B: Condens. Matter Mater. Phys.* **2001**, *63*, 113104.

(279) Jalan, B.; Stemmer, S. Large Seebeck coefficients and thermoelectric power factor of La-doped $SrTiO_3$ thin films. *Appl. Phys. Lett.* **2010**, *97*, No. 042106.

(280) Cain, T. A.; Kajdos, A. P.; Stemmer, S. La-doped $SrTiO_3$ films with large cryogenic thermoelectric power factors. *Appl. Phys. Lett.* **2013**, *102*, 182101.

(281) Gruner, M. E.; Eckern, U.; Pentcheva, R. Impact of strain-induced electronic topological transition on the thermoelectric properties of $PtCoO_2$ and $PdCoO_2$. *Phys. Rev. B: Condens. Matter Mater. Phys.* **2015**, *92*, 235140.

(282) Hicks, L. D.; Dresselhaus, M. S. Effect of quantum-well structures on the thermoelectric figure of merit. *Phys. Rev. B: Condens. Matter Mater. Phys.* **1993**, *47*, 12727−12731.

(283) Mao, J.; Liu, Z.; Ren, Z. Size effect in thermoelectric materials. *npj Quantum Mater.* **2016**, *1*, 16028.

(284) Ohta, H.; Kim, S.; Mune, Y.; Mizoguchi, T.; Nomura, K.; Ohta, S.; Nomura, T.; Nakanishi, Y.; Ikuhara, Y.; Hirano, M.; Hosono, H.; Koumoto, K. Giant thermoelectric Seebeck coefficient of two-dimensional electron gas in $SrTiO_3$. *Nat. Mater.* **2007**, *6*, 129.

(285) Filippetti, A.; Delugas, P.; Verstraete, M. J.; Pallecchi, I.; Gadaleta, A.; Marré, D.; Li, D. F.; Gariglio, S.; Fiorentini, V. Thermopower in oxide heterostructures: The importance of being multiple-band conductors. *Phys. Rev. B: Condens. Matter Mater. Phys.* **2012**, *86*, 195301.

(286) García-Fernández, P.; Verissimo-Alves, M.; Bilc, D. I.; Ghosez, P.; Junquera, J. First principles modeling of the thermoelectric properties of $SrTiO_3/SrRuO_3$ superlattices. *Phys. Rev. B: Condens. Matter Mater. Phys.* **2012**, *86*, No. 085305.

(287) Delugas, P.; Filippetti, A.; Verstraete, M. J.; Pallecchi, I.; Marré, D.; Fiorentini, V. Doping-induced dimensional crossover and thermopower burst in Nb-doped $SrTiO_3$ superlattices. *Phys. Rev. B: Condens. Matter Mater. Phys.* **2013**, *88*, No. 045310.

(288) Pallecchi, I.; Telesio, F.; Li, D.; Fête, A.; Gariglio, S.; Triscone, J.-M.; Filippetti, A.; Delugas, P.; Fiorentini, V.; Marré, D. Giant oscillating thermopower at oxide interfaces. *Nat. Commun.* **2015**, *6*, 6678.

(289) Bilc, D. I.; Floare, C. G.; Zârbo, L. P.; Garabagiu, S.; Lemal, S.; Ghosez, P. First Principles Modeling of $SrTiO_3$ Based Oxides for Thermoelectric Applications. *J. Phys. Chem. C* **2016**, *120*, 25678−25688.

(290) Geisler, B.; Blanca-Romero, A.; Pentcheva, R. Design of n- and p-type oxide thermoelectrics in $LaNiO_3/SrTiO_3(001)$ superlattices exploiting interface polarity. *Phys. Rev. B: Condens. Matter Mater. Phys.* **2017**, *95*, 125301.

(291) Geisler, B.; Pentcheva, R. Confinement- and strain-induced enhancement of thermoelectric properties in $LaNiO_3/LaAlO_3(001)$ superlattices. *Phys. Rev. Materials* **2018**, *2*, No. 055403.

(292) Geisler, B.; Pentcheva, R. Inducing n- and p-Type Thermoelectricity in Oxide Superlattices by Strain Tuning of Orbital-Selective Transport Resonances. *Phys. Rev. Appl.* **2019**, *11*, No. 044047.

(293) Geisler, B.; Kratzer, P. Spincaloric properties of epitaxial $Co_2MnSi/MgO/Co_2MnSi$ magnetic tunnel junctions. *Phys. Rev. B: Condens. Matter Mater. Phys.* **2015**, *92*, 144418.

(294) Geisler, B.; Kratzer, P.; Popescu, V. Interplay of growth mode and thermally induced spin accumulation in epitaxial $Al/Co_2TiSi/Al$ and $Al/Co_2TiGe/Al$ contacts. *Phys. Rev. B: Condens. Matter Mater. Phys.* **2014**, *89*, 184422.

(295) Comtesse, D.; Geisler, B.; Entel, P.; Kratzer, P.; Szunyogh, L. First-principles study of spin-dependent thermoelectric properties of half-metallic Heusler thin films between platinum leads. *Phys. Rev. B: Condens. Matter Mater. Phys.* **2014**, *89*, No. 094410.

(296) Popescu, V. Spin caloric transport from density-functional theory. *J. Phys. D: Appl. Phys.* **2019**, *52*, 073001.

(297) Middey, S.; Chakhalian, J.; Mahadevan, P.; Freeland, J.; Millis, A.; Sarma, D. Physics of Ultrathin Films and Heterostructures of Rare-Earth Nickelates. *Annu. Rev. Mater. Res.* **2016**, *46*, 305−334.

(298) Lorenz, M.; et al. The 2016 oxide electronic materials and oxide interfaces roadmap. *J. Phys. D: Appl. Phys.* **2016**, *49*, 433001.

(299) Wrobel, F.; Geisler, B.; Wang, Y.; Christiani, G.; Logvenov, G.; Bluschke, M.; Schierle, E.; van Aken, P. A.; Keimer, B.; Pentcheva, R.; Benckiser, E. Digital modulation of the nickel valence state in a cuprate-nickelate heterostructure. *Phys. Rev. Materials* **2018**, *2*, No. 035001.

(300) Liu, J.; Okamoto, S.; van Veenendaal, M.; Kareev, M.; Gray, B.; Ryan, P.; Freeland, J. W.; Chakhalian, J. Quantum confinement of Mott electrons in ultrathin $LaNiO_3/LaAlO_3$ superlattices. *Phys. Rev. B: Condens. Matter Mater. Phys.* **2011**, *83*, 161102.

(301) Son, J.; LeBeau, J. M.; Allen, S. J.; Stemmer, S. Conductivity enhancement of ultrathin $LaNiO_3$ films in superlattices. *Appl. Phys. Lett.* **2010**, *97*, 202109.

(302) Kaiser, A. M.; Gray, A. X.; Conti, G.; Son, J.; Greer, A.; Perona, A.; Rattanachata, A.; Saw, A. Y.; Bostwick, A.; Yang, S.; Yang, S.-H.; Gullikson, E. M.; Kortright, J. B.; Stemmer, S.; Fadley, C. S. Suppression of Near-Fermi Level Electronic States at the Interface in a $LaNiO_3/SrTiO_3$ Superlattice. *Phys. Rev. Lett.* **2011**, *107*, 116402.

(303) Hwang, J.; Son, J.; Zhang, J. Y.; Janotti, A.; Van de Walle, C. G.; Stemmer, S. Structural origins of the properties of rare earth nickelate superlattices. *Phys. Rev. B: Condens. Matter Mater. Phys.* **2013**, *87*, No. 060101.

(304) Wrobel, F.; Mark, A. F.; Christiani, G.; Sigle, W.; Habermeier, H.-U.; van Aken, P. A.; Logvenov, G.; Keimer, B.; Benckiser, E. Comparative study of $LaNiO_3/LaAlO_3$ heterostructures grown by pulsed laser deposition and oxide molecular beam epitaxy. *Appl. Phys. Lett.* **2017**, *110*, No. 041606.

(305) Kaya, P.; Gregori, G.; Baiutti, F.; Yordanov, P.; Suyolcu, Y. E.; Cristiani, G.; Wrobel, F.; Benckiser, E.; Keimer, B.; van Aken, P. A.; Habermeier, H.-U.; Logvenov, G.; Maier, J. High-Temperature Thermoelectricity in $LaNiO_3$-La_2CuO_4 Heterostructures. *ACS Appl. Mater. Interfaces* **2018**, *10*, 22786−22792.

(306) Pardo, V.; Botana, A. S.; Baldomir, D. Enhanced thermoelectric response of hole-doped $La_2NiO_{4+\delta}$ from ab initio calculations. *Phys. Rev. B: Condens. Matter Mater. Phys.* **2012**, *86*, 165114.

(307) Noguera, C. Polar oxide surfaces. *J. Phys.: Condens. Matter* **2000**, *12*, R367.

(308) Nakagawa, N.; Hwang, H. Y.; Muller, D. A. Why some interfaces cannot be sharp. *Nat. Mater.* **2006**, *5*, 204.

(309) Pentcheva, R.; Pickett, W. E. Charge localization or itineracy at $LaAlO_3/SrTiO_3$ interfaces: Hole polarons, oxygen vacancies, and mobile electrons. *Phys. Rev. B: Condens. Matter Mater. Phys.* **2006**, *74*, No. 035112.

(310) Botana, A. S.; Pardo, V.; Pickett, W. E. All-3d Electron-Hole Bilayers in CrN/MgO(111) Multilayers for Thermoelectric Applications. *Phys. Rev. Appl.* **2017**, *7*, No. 024002.

(311) Harrison, W. A.; Kraut, E. A.; Waldrop, J. R.; Grant, R. W. Polar heterojunction interfaces. *Phys. Rev. B: Condens. Matter Mater. Phys.* **1978**, *18*, 4402−4410.

(312) Blanca-Romero, A.; Pentcheva, R. Confinement-induced metal-to-insulator transition in strained $LaNiO_3/LaAlO_3$ superlattices. *Phys. Rev. B: Condens. Matter Mater. Phys.* **2011**, *84*, 195450.

(313) Freeland, J. W.; Liu, J.; Kareev, M.; Gray, B.; Kim, J. W.; Ryan, P.; Pentcheva, R.; Chakhalian, J. Orbital control in strained ultra-thin $LaNiO_3/LaAlO_3$ superlattices. *Europhys. Lett.* **2011**, *96*, 57004.

(314) Yordanov, P.; Wochner, P.; Ibrahimkutty, S.; Dietl, C.; Wrobel, F.; Felici, R.; Gregori, G.; Maier, J.; Keimer, B.; Habermeier, H.-U. Perovskite substrates boost the thermopower of cobaltate thin films at high temperatures. *Appl. Phys. Lett.* **2017**, *110*, 253101.

(315) Sivan, U.; Imry, Y. Multichannel Landauer formula for thermoelectric transport with application to thermopower near the mobility edge. *Phys. Rev. B: Condens. Matter Mater. Phys.* **1986**, *33*, 551−558.

(316) Mahan, G. D.; Sofo, J. O. The best thermoelectric. *Proc. Natl. Acad. Sci. U. S. A.* **1996**, *93*, 7436−7439.

(317) Nakpathomkun, N.; Xu, H. Q.; Linke, H. Thermoelectric efficiency at maximum power in low-dimensional systems. *Phys. Rev. B: Condens. Matter Mater. Phys.* **2010**, *82*, 235428.

(318) Jordan, A. N.; Sothmann, B.; Sánchez, R.; Büttiker, M. Powerful and efficient energy harvester with resonant-tunneling quantum dots. *Phys. Rev. B: Condens. Matter Mater. Phys.* **2013**, *87*, No. 075312.

DOI: 10.1021/acs.inorgchem.9b01785
Inorg. Chem. 2019, 58, 14939−14980

(319) Han, M. J.; Marianetti, C. A.; Millis, A. J. Chemical control of orbital polarization in artificially structured transition-metal oxides: La_2NiXO_6 (X = B, Al, Ga, In) from first principles. *Phys. Rev. B: Condens. Matter Mater. Phys.* **2010**, *82*, 134408.

(320) Wu, M.; et al. Strain and composition dependence of orbital polarization in nickeloxide superlattices. *Phys. Rev. B: Condens. Matter Mater. Phys.* **2013**, *88*, 125124.

(321) Doennig, D.; Pickett, W. E.; Pentcheva, R. Confinement-driven transitions between topological and Mott phases in $(LaNiO_3)_N/(LaAlO_3)_M(111)$ superlattices. *Phys. Rev. B: Condens. Matter Mater. Phys.* **2014**, *89*, 121110.

(322) Disa, A. S.; Kumah, D. P.; Malashevich, A.; Chen, H.; Arena, D. A.; Specht, E. D.; Ismail-Beigi, S.; Walker, F. J.; Ahn, C. H. Orbital Engineering in Symmetry Breaking Polar Heterostructures. *Phys. Rev. Lett.* **2015**, *114*, No. 026801.

(323) Bernardi, M.; Vigil-Fowler, D.; Lischner, J.; Neaton, J. B.; Louie, S. G. Ab Initio Study of Hot Carriers in the First Picosecond after Sunlight Absorption in Silicon. *Phys. Rev. Lett.* **2014**, *112*, 257402.

(324) Mustafa, J. I.; Bernardi, M.; Neaton, J. B.; Louie, S. G. Ab initio electronic relaxation times and transport in noble metals. *Phys. Rev. B: Condens. Matter Mater. Phys.* **2016**, *94*, 155105.

(325) Dekura, H.; Tsuchiya, T. Ab initio lattice thermal conductivity of MgO from a complete solution of the linearized Boltzmann transport equation. *Phys. Rev. B: Condens. Matter Mater. Phys.* **2017**, *95*, 184303.

(326) Zhang, J.; Bachman, M.; Czerner, M.; Heiliger, C. Thermal Transport and Non equilibrium Temperature Drop Across a Magnetic Tunnel Junction. *Phys. Rev. Lett.* **2015**, *115*, No. 037203.

(327) Mizuno, H.; Mossa, S.; Barrat, J.-L. Beating the amorphous limit in thermal conductivity by superlattices design. *Sci. Rep.* **2015**, *5*, 14116.

(328) O'Dwyer, C.; Chen, R.; He, J.-H.; Lee, J.; Razeeb, K. M. Scientific and Technical Challenges in Thermal Transport and Thermoelectric Materials and Devices. *ECS J. Solid State Sci. Technol.* **2017**, *6*, N3058.

(329) Katsufuji, T.; Saiki, T.; Okubo, S.; Katayama, Y.; Ueno, K. Thermal conductivity of $SrVO_3$–$SrTiO_3$ thin films: Evidence of intrinsic thermal resistance at the interface between oxide layers. *Phys. Rev. Materials* **2018**, *2*, No. 051002.

(330) Ravichandran, J.; et al. Crossover from incoherent to coherent phonon scattering in epitaxial oxide superlattices. *Nat. Mater.* **2014**, *13*, 168.

(331) Luckyanova, M. N.; Garg, J.; Esfarjani, K.; Jandl, A.; Bulsara, M. T.; Schmidt, A. J.; Minnich, A. J.; Chen, S.; Dresselhaus, M. S.; Ren, Z.; Fitzgerald, E. A.; Chen, G. Coherent Phonon Heat Conduction in Superlattices. *Science* **2012**, *338*, 936–939.

(332) Garg, J.; Bonini, N.; Marzari, N. High Thermal Conductivity in Short-Period Superlattices. *Nano Lett.* **2011**, *11*, 5135–5141.

(333) Zhao, H. J.; Filippetti, A.; Escorihuela-Sayalero, C.; Delugas, P.; Canadell, E.; Bellaiche, L.; Fiorentini, V.; Íñiguez, J. Meta-screening and permanence of polar distortion in metallized ferroelectrics. *Phys. Rev. B: Condens. Matter Mater. Phys.* **2018**, *97*, No. 054107.

(334) Filippetti, A.; Fiorentini, V.; Ricci, F.; Delugas, P.; Íñiguez, J. Prediction of a native ferroelectric metal. *Nat. Commun.* **2016**, *7*, 11211.

(335) Urru, A.; Filippetti, A.; Ricci, F.; Íñiguez, J.; Fiorentini, V. *to be published.*.

(336) Anderson, P. W.; Blount, E. I. Symmetry Considerations on Martensitic Transformations: "Ferroelectric" Metals? *Phys. Rev. Lett.* **1965**, *14*, 217–219.

(337) Padmanabhan, H.; Park, Y.; Puggioni, D.; Yuan, Y.; Cao, Y.; Gasparov, L.; Shi, Y.; Chakhalian, J.; Rondinelli, J. M.; Gopalan, V. Linear and nonlinear optical probe of the ferroelectric-like phase transition in a polar metal, $LiOsO_3$. *Appl. Phys. Lett.* **2018**, *113*, 122906.

(338) Puggioni, D.; Giovannetti, G.; Capone, M.; Rondinelli, J. M. Design of a Mott Multiferroic from a Nonmagnetic Polar Metal. *Phys. Rev. Lett.* **2015**, *115*, No. 087202.

(339) Puggioni, D.; Rondinelli, J. M. Designing a robustly metallic noncenstrosymmetric ruthenate oxide with large thermopower anisotropy. *Nat. Commun.* **2014**, *5*, 3432.

(340) Benedek, N. A.; Birol, T. "Ferroelectric" metals reexamined: fundamental mechanisms and design considerations for new materials. *J. Mater. Chem. C* **2016**, *4*, 4000–4015.

(341) Scarrozza, M.; Filippetti, A.; Fiorentini, V. Ferromagnetism and Orbital Order in a Topological Ferroelectric. *Phys. Rev. Lett.* **2012**, *109*, 217202.

(342) López-Pérez, J.; Íñiguez, J. Ab initio study of proper topological ferroelectricity in layered perovskite $La_2Ti_2O_7$. *Phys. Rev. B: Condens. Matter Mater. Phys.* **2011**, *84*, No. 075121.

(343) Vanderbilt, D. *Berry Phases in Electronic Structure Theory;* Cambridge University Press, 2018.

(344) Park, S. J.; Kim, T. Y.; Park, C.-H.; Kim, D.-S. Optical responses of a metal with sub-nm gaps. *Sci. Rep.* **2016**, *6*, 22981.

(345) Garrity, K. F.; Rabe, K. M.; Vanderbilt, D. Hyperferroelectrics: Proper Ferroelectrics with Persistent Polarization. *Phys. Rev. Lett.* **2014**, *112*, 127601.

(346) Puggioni, D.; Stroppa, A.; Rondinelli, J. M. Design of a polar half-metallic ferromagnet with accessible and enhanced electric polarization. *Phys. Rev. Materials* **2018**, *2*, 114403.

(347) Rao, C.; Cheetham, A.; Thirumurugan, A. Hybrid inorganic–organic materials: a new family in condensed matter physics. *J. Phys.: Condens. Matter* **2008**, *20*, No. 083202.

(348) Wenk, H.-R.; Bulakh, A. *Minerals: their constitution and origin;* Cambridge University Press, 2016.

(349) Jain, P.; Ramachandran, V.; Clark, R. J.; Zhou, H. D.; Toby, B. H.; Dalal, N. S.; Kroto, H. W.; Cheetham, A. K. Multiferroic behavior associated with an order–disorder hydrogen bonding transition in metal-organic frameworks (MOFs) with the perovskite ABX_3 architecture. *J. Am. Chem. Soc.* **2009**, *131*, 13625–13627.

(350) Besara, T.; Jain, P.; Dalal, N. S.; Kuhns, P. L.; Reyes, A. P.; Kroto, H. W.; Cheetham, A. K. Mechanism of the order–disorder phase transition, and glassy behavior in the metal-organic framework $[(CH_3)_2NH_2]\ Zn(HCOO)_3$. *Proc. Natl. Acad. Sci. U. S. A.* **2011**, *108*, 6828.

(351) Ramesh, R. Materials science: Emerging routes to multiferroics. *Nature* **2009**, *461*, 1218.

(352) Kieslich, G.; Sun, S.; Cheetham, A. K. An extended tolerance factor approach for organic–inorganic perovskites. *Chemical science* **2015**, *6*, 3430–3433.

(353) Kieslich, G.; Sun, S.; Cheetham, A. K. Solid-state principles applied to organic–inorganic perovskites: new tricks for an old dog. *Chemical Science* **2014**, *5*, 4712–4715.

(354) Hu, K.-L.; Kurmoo, M.; Wang, Z.; Gao, S. Metal–Organic Perovskites: Synthesis, Structures, and Magnetic Properties of $[C(NH_2)_3][MII(HCOO)_3](M$ = Mn, Fe, Co, Ni, Cu, and Zn; $C(NH_2)_3$ = Guanidinium). *Chem.–Eur. J.* **2009**, *15*, 12050–12064.

(355) Stroppa, A.; Jain, P.; Barone, P.; Marsman, M.; Perez-Mato, J. M.; Cheetham, A. K.; Kroto, H. W.; Picozzi, S. Electric control of magnetization and interplay between orbital ordering and ferroelectricity in a multiferroic metal–organic framework. *Angew. Chem., Int. Ed.* **2011**, *50*, 5847–5850.

(356) Ghosh, S.; Di Sante, D.; Stroppa, A. Strain tuning of ferroelectric polarization in hybrid organic inorganic perovskite compounds. *J. Phys. Chem. Lett.* **2015**, *6*, 4553–4559.

(357) Stroppa, A.; Barone, P.; Jain, P.; Perez-Mato, J. M.; Picozzi, S. Hybrid Improper Ferroelectricity in a Multiferroic and Magnetoelectric Metal-Organic Framework. *Adv. Mater.* **2013**, *25*, 2284–2290.

(358) Tian, Y.; Stroppa, A.; Chai, Y.; Yan, L.; Wang, S.; Barone, P.; Picozzi, S.; Sun, Y. Cross coupling between electric and magnetic orders in a multiferroic metal-organic framework. *Sci. Rep.* **2015**, *4*, 6062.

(359) Stroppa, A.; Di Sante, D.; Barone, P.; Bokdam, M.; Kresse, G.; Franchini, C.; Whangbo, M.-H.; Picozzi, S. Tunable ferroelectric

polarization and its interplay with spin−orbit coupling in tin iodide perovskites. *Nat. Commun.* **2014**, *5*, 5900.

(360) Di Sante, D.; Stroppa, A.; Jain, P.; Picozzi, S. Tuning the ferroelectric polarization in a multiferroic metal−organic framework. *J. Am. Chem. Soc.* **2013**, *135*, 18126−18130.

(361) Mazzuca, L.; Cañadillas-Delgado, L.; Rodríguez-Velamazán, J. A.; Fabelo, O.; Scarrozza, M.; Stroppa, A.; Picozzi, S.; Zhao, J.-P.; Bu, X.-H.; Rodríguez-Carvajal, J. Magnetic structures of heterometallic M (II)−M (III) formate compounds. *Inorg. Chem.* **2017**, *56*, 197−207.

(362) Kamminga, M. E.; Stroppa, A.; Picozzi, S.; Chislov, M.; Zvereva, I. A.; Baas, J.; Meetsma, A.; Blake, G. R.; Palstra, T. T. Polar Nature of $(CH_3NH_3)_3Bi_2I_9$ Perovskite-Like Hybrids. *Inorg. Chem.* **2017**, *56*, 33−41.

(363) Gómez-Aguirre, L.; Pato-Doldán, B.; Stroppa, A.; Yang, L.; Frauenheim, T.; Mira, J.; Yáñez-Vilar, S.; Artiaga, R.; Castro-García, S.; Sánchez-Andújar, M.; Señaris Rodríguez, M. Coexistence of Three Ferroic Orders in the Multiferroic Compound $[(CH_3)_4N][Mn(N_3)_3]$ with Perovskite-Like Structure. *Chem.−Eur. J.* **2016**, *22*, 7863−7870.

(364) Ptak, M.; Mączka, M.; Gągor, A.; Sieradzki, A.; Stroppa, A.; Di Sante, D.; PerezMato, J. M.; Macalik, L. Experimental and theoretical studies of structural phase transition in a novel polar perovskite-like $[C_2H_5\ NH_3][Na_{0.5}Fe_{0.5}(HCOO)_3]$ formate. *Dalton transactions* **2016**, *45*, 2574−2583.

(365) Zhao, W.-P.; Shi, C.; Stroppa, A.; Di Sante, D.; Cimpoesu, F.; Zhang, W. LonePair-Electron-Driven Ionic Displacements in a Ferroelectric Metal-Organic Hybrid. *Inorg. Chem.* **2016**, *55*, 10337−10342.

(366) Gómez-Aguirre, L.; Pato-Doldán, B.; Stroppa, A.; Yáñez-Vilar, S.; Bayarjargal, L.; Winkler, B.; Castro-García, S.; Mira, J.; Sánchez-Andújar, M.; Señarís-Rodríguez, M. Room-temperature polar order in $[NH_4][Cd(HCOO)_3]$-a hybrid inorganic-organic compound with a unique perovskite architecture. *Inorg. Chem.* **2015**, *54*, 2109−2116.

(367) Stroppa, A.; Quarti, C.; De Angelis, F.; Picozzi, S. Ferroelectric polarization of $CH_3NH_3PbI_3$: a detailed study based on density functional theory and symmetry mode analysis. *J. Phys. Chem. Lett.* **2015**, *6*, 2223−2231.

(368) Tian, Y.; Stroppa, A.; Chai, Y.-S.; Barone, P.; Perez-Mato, M.; Picozzi, S.; Sun, Y. High-temperature ferroelectricity and strong magnetoelectric effects in a hybrid organic−inorganic perovskite framework. *Phys. Status Solidi RRL* **2015**, *9*, 62−67.

(369) Lee, C.; Hong, J.; Stroppa, A.; Whangbo, M.-H.; Shim, J. H. Organic−inorganic hybrid perovskites ABI_3 ($A = CH_3\ NH_3$, $NH_2\ CHNH_2$; $B = Sn, Pb$) as potential thermoelectric materials: a density functional evaluation. *RSC Adv.* **2015**, *5*, 78701−78707.

(370) Lee, M. M.; Teuscher, J.; Miyasaka, T.; Murakami, T. N.; Snaith, H. J. Efficient hybrid solarcells based on meso-superstructured organometal halide perovskites. *Science* **2012**, *338*, 1228604.

(371) Kim, H.-S.; Lee, C.-R.; Im, J.-H.; Lee, K.-B.; Moehl, T.; Marchioro, A.; Moon, S. J.; Humphry-Baker, R.; Yum, J.-H.; Moser, J. E.; Grätzel, M.; Park, N.-G. Lead Iodide Perovskite Sensitized All-Solid-State Submicron Thin Film Mesoscopic Solar Cell with Efficiency Exceeding 9%. *Sci. Rep.* **2012**, *2*, 591.

(372) Docampo, P.; Ball, J. M.; Darwich, M.; Eperon, G. E.; Snaith, H. J. Efficient organometal trihalide perovskite planar-heterojunction solar cells on flexible polymer substrates. *Nat. Commun.* **2013**, *4*, 2761.

(373) Burschka, J.; Pellet, N.; Moon, S.-J.; Humphry-Baker, R.; Gao, P.; Nazeeruddin, M. K.; Grätzel, M. Sequential deposition as a route to high-performance perovskite-sensitized solar cells. *Nature* **2013**, *499*, 316.

(374) Liu, M.; Johnston, M. B.; Snaith, H. J. Efficient planar heterojunction perovskite solar cells by vapour deposition. *Nature* **2013**, *501*, 395.

(375) Liu, D.; Kelly, T. L. Perovskite solar cells with a planar heterojunction structure prepared using room-temperature solution processing techniques. *Nat. Photonics* **2014**, *8*, 133.

(376) Malinkiewicz, O.; Yella, A.; Lee, Y. H.; Espallargas, G. M.; Graetzel, M.; Nazeeruddin, M. K.; Bolink, H. J. Perovskite solar cells employing organic charge-transport layers. *Nat. Photonics* **2014**, *8*, 128.

(377) Mei, A.; Li, X.; Liu, L.; Ku, Z.; Liu, T.; Rong, Y.; Xu, M.; Hu, M.; Chen, J.; Yang, Y.; Grätzel, M.; Han, H. A hole-conductor−free,fullyprintablemesoscopicperovskitesolar cell with high stability. *Science* **2014**, *345*, 295−298.

(378) Green, M. A.; Ho-Baillie, A.; Snaith, H. J. The emergence of perovskite solar cells. *Nat. Photonics* **2014**, *8*, 506.

(379) Bellitto, C.; Bauer, E. M.; Righini, G. Organic−inorganic hybrids: from magnetic perovskite metal (II) halides to multifunctional metal (II) phosphonates. *Coord. Chem. Rev.* **2015**, *289*, 123−136.

(380) Náfrádi, B.; Szirmai, P.; Spina, M.; Lee, H.; Yazyev, O.; Arakcheeva, A.; Chernyshov, D.; Gibert, M.; Forró, L.; Horváth, E. Optically switched magnetism in photovoltaic perovskite $CH_3NH_3(Mn:Pb)I_3$. *Nat. Commun.* **2016**, *7*, 13406.

(381) Ping, Y.; Zhang, J. Z. Spin-optotronic Properties of Organometal Halide Perovskites. *J. Phys. Chem. Lett.* **2018**, *9*, 6103−6111.

(382) Gong, C.; Li, L.; Li, Z.; Ji, H.; Stern, A.; Xia, Y.; Cao, T.; Bao, W.; Wang, C.; Wang, Y.; Qiu, Z. Q.; Cava, R. J.; Louie, S. G.; Xia, J.; Zhang, X. Discovery of intrinsic ferromagnetism in two-dimensional van der Waals crystals. *Nature* **2017**, *546*, 265.

(383) Huang, B.; Clark, G.; Navarro-Moratalla, E.; Klein, D. R.; Cheng, R.; Seyler, K. L.; Zhong, D.; Schmidgall, E.; McGuire, M. A.; Cobden, D. H.; Yao, W.; Xiao, D.; JarilloHerrero, P.; Xu, X. Layer-dependent ferromagnetism in a van der Waals crystal down to the monolayer limit. *Nature* **2017**, *546*, 270.

(384) Huang, B.; Zhang, J.-Y.; Huang, R.-K.; Chen, M.-K.; Xue, W.; Zhang, W.-X.; Zeng, M.-H.; Chen, X.-M. Spin-reorientation-induced magnetodielectric coupling effects in two layered perovskite magnets. *Chemical Science* **2018**, *9*, 7413−7418.

(385) Pedersen, K. S.; et al. Formation of the layered conductive magnet $CrCl_2(pyrazine)_2$ through redox-active coordination chemistry. *Nat. Chem.* **2018**, *10*, 1056−1061.

(386) Fiebig, M.; Lottermoser, T.; Meier, D.; Trassin, M. The evolution of multiferroics. *Nature Reviews Materials* **2016**, *1*, 16046.

(387) Dong, S.; Liu, J.-M.; Cheong, S.-W.; Ren, Z. Multiferroic materials and magnetoelectric physics: symmetry, entanglement, excitation, and topology. *Adv. Phys.* **2015**, *64*, 519−626.

(388) Eerenstein, W.; Mathur, N.; Scott, J. F. Multiferroic and magnetoelectric materials. *Nature* **2006**, *442*, 759.

(389) Dadoenkova, Y. S.; Lyubchanskii, I. L.; Lee, Y.; Rasing, T. Electric field controlled magneto-optical kerr effect at light reflection from an electro-optic/magneto-optic bilayer. *IEEE Trans. Magn.* **2011**, *47*, 1623−1626.

(390) Prati, E. Propagation in Gyroelectromagnetic Guiding Systems. *Journal of Electromagnetic Waves and Applications* **2003**, *17*, 1177−1196.

(391) Brown, W., Jr; Shtrikman, S.; Treves, D. Possibility of visual observation of antiferromagnetic domains. *J. Appl. Phys.* **1963**, *34*, 1233−1234.

(392) Fan, F.-R.; Wu, H.; Nabok, D.; Hu, S.; Ren, W.; Draxl, C.; Stroppa, A. ElectricMagneto-Optical Kerr Effect in a Hybrid Organic−Inorganic Perovskite. *J. Am. Chem. Soc.* **2017**, *139*, 12883−12886.

(393) Kerr, J. XLIII. On rotation of the plane of polarization by reflection from the pole of a magnet. *London, Edinburgh, and Dublin Philosophical Magazine and Journal of Science* **1877**, *3*, 321−343.

(394) Buschow, K. v.; Van Engen, P.; Jongebreur, R. Magneto-optical properties of metallic ferromagnetic materials. *J. Magn. Magn. Mater.* **1983**, *38*, 1−22.

(395) Mansuripur, M. *The physical principles of magneto-optical recording;* Cambridge University Press, 1998.

(396) Mee, C. D.; Daniel, E. D. *Magnetic Recording Technology;* McGraw-Hill: New York, 1987; Vol. *1*, pp 323−324.

(397) Waser, R.; Keller, H.; Erb, U. *Nanoelectronics and information technology: Advanced electronic materials and novel devices;* John Wiley & Sons, Inc., 2004.

(398) Schmidt, F.; Rave, W.; Hubert, A. Enhancement of magneto-optical domain observation by digital image processing. *IEEE Trans. Magn.* **1985**, *21*, 1596−1598.

(399) Stroppa, A.; Picozzi, S.; Continenza, A.; Kim, M.; Freeman, A. J. Magneto-optical properties of (Ga, Mn) As: An ab initio determination. *Phys. Rev. B: Condens. Matter Mater. Phys.* **2008**, *77*, No. 035208.

(400) Feng, W.; Guo, G.-Y.; Zhou, J.; Yao, Y.; Niu, Q. Large magneto-optical Kerr effect in noncollinear antiferromagnets Mn_3X (X = Rh, Ir, Pt). *Phys. Rev. B: Condens. Matter Mater. Phys.* **2015**, *92*, 144426.

(401) Sivadas, N.; Okamoto, S.; Xiao, D. Gate-controllable magneto-optic Kerr effect in layered collinear antiferromagnets. *Phys. Rev. Lett.* **2016**, *117*, 267203.

(402) Sangalli, D.; Marini, A.; Debernardi, A. Pseudopotential-based first-principles approach to the magneto-optical Kerr effect: From metals to the inclusion of local fields and excitonic effects. *Phys. Rev. B: Condens. Matter Mater. Phys.* **2012**, *86*, 125139.

(403) Eremenko, V. V.; Kharchenko, N.; Litvinenko, Y. G.; Naumenko, V. *Magneto-optics and Spectroscopy of Antiferromagnets;* Springer Science & Business Media, 2012.

(404) Jungwirth, T.; Marti, X.; Wadley, P.; Wunderlich, J. Antiferromagnetic spintronics. *Nat. Nanotechnol.* **2016**, *11*, 231.

(405) Baltz, V.; Manchon, A.; Tsoi, M.; Moriyama, T.; Ono, T.; Tserkovnyak, Y. Antiferromagnetic spintronics. *Rev. Mod. Phys.* **2018**, *90*, No. 015005.

(406) Jungwirth, T.; Sinova, J.; Manchon, A.; Marti, X.; Wunderlich, J.; Felser, C. The multiple directions of antiferromagnetic spintronics. *Nat. Phys.* **2018**, *14*, 200.

(407) Šmejkal, L.; Mokrousov, Y.; Yan, B.; MacDonald, A. H. Topological antiferromagnetic spintronics. *Nat. Phys.* **2018**, *14*, 1.

(408) Bodnar, S. Y.; Šmejkal, L.; Turek, I.; Jungwirth, T.; Gomonay, O.; Sinova, J.; Sapozhnik, A.; Elmers, H.-J.; Kläui, M.; Jourdan, M. Writing and reading antiferromagnetic Mn_2Au by Néel spin-orbit torques and large anisotropic magnetoresistance. *Nat. Commun.* **2018**, *9*, 348.

(409) Němec, P.; Fiebig, M.; Kampfrath, T.; Kimel, A. V. Antiferromagnetic opto-spintronics. *Nat. Phys.* **2018**, *1*, 229.

(410) Wadley, P.; et al. Electrical switching of an antiferromagnet. *Science* **2016**, *351*, 587−590.

(411) Godinho, J.; Reichlova, H.; Kriegner, D.; Novak, V.; Olejnik, K.; Kaspar, Z.; Soban, Z.; Wadley, P.; Campion, R. P.; Otxoa, R. M.; Roy, P. E.; Zelezny, J.; Jungwirth, T.; Wunderlich, J. Electrically induced and detected Néel vector reversal in a collinear antiferromagnet. *Nat. Commun.* **2018**, *9*, DOI: 10.1038/s41467-018-07092-2.

(412) Haldane, F. D. M. Nobel lecture: Topological quantum matter. *Rev. Mod. Phys.* **2017**, *89*, No. 040502.

(413) DC, M.; Grassi, R.; Chen, J.-Y.; Jamali, M.; Reifsnyder Hickey, D.; Zhang, D.; Zhao, Z.; Li, H.; Quarterman, P.; Lv, Y.; Li, M.; Manchon, A.; Mkhoyan, K. A.; Low, T.; Wang, J.-P. Room-temperature high spin-orbit torque due to quantum confinement in sputtered $Bi_xSe_{(1-x)}$ films. *Nat. Mater.* **2018**, *17*, 800−807.

(414) Li, P.; Wu, W.; Wen, Y.; Zhang, C.; Zhang, J.; Zhang, S.; Yu, Z.; Yang, S. A.; Manchon, A.; Zhang, X.-x. Spin-momentum locking and spin-orbit torques in magnetic nano-heterojunctions composed of Weyl semimetal WTe_2. *Nat. Commun.* **2018**, *9*, 3990.

(415) Xing, W.; Chen, Y.; Odenthal, P. M.; Zhang, X.; Yuan, W.; Su, T.; Song, Q.; Wang, T.; Zhong, J.; Jia, S.; Xie, X. C.; Li, Y.; Han, W. Electric field effect in multilayer $Cr_2Ge_2Te_6$: a ferromagnetic 2D material. *2D Mater.* **2017**, *4*, No. 024009.

(416) Higo, T.; et al. Large magneto-optical Kerr effect and imaging of magnetic octupole domains in an antiferromagnetic metal. *Nat. Photonics* **2018**, *12*, 73−78.

(417) Hutchings, I.; Shipway, P. *Tribology,* 2nd ed.; Butterworth-Heinemann, 2017; DOI: 10.1016/B978-0-08-100910-9.00001-5.

(418) Holmberg, K.; Erdemir, A. Influence of tribology on global energy consumption, costs and emissions. *Friction* **2017**, *5*, 263−284.

(419) Vakis, A.; et al. Modeling and Simulation in Tribology Across Scales: an Overview. *Tribol. Int.* **2018**, *125*, 169−199.

(420) Wang, Z. Self-Powered Nanosensors and Nanosystems. *Adv. Mater.* **2012**, *24*, 280.

(421) Hinchet, R.; Seung, W.; Kim, S.-W. Recent Progress on Flexible Triboelectric Nanogenerators for Self-Powered Electronics. *ChemSusChem* **2015**, *8*, 2327.

(422) Zi, Y.; Wang, Z. Nanogenerators: An Emerging Technology towards Nanoenergy. *APL Mater.* **2017**, *5*, 74103.

(423) Khan, U.; Hinchet, R.; Ryu, H.; Kim, S.-W. Research Update: Nanogenerators for self-powered autonomous wireless sensors. *APL Mater.* **2017**, *5*, No. 073803.

(424) Wang, Z. Triboelectric Nanogenerators as New Energy Technology for Self-Powered Systems and as Active Mechanical and Chemical Sensors. *ACS Nano* **2013**, *7*, 9533.

(425) Zi, Y.; Guo, H.; Wen, Z.; Yeh, M.-H.; Hu, C.; Wang, Z. Harvesting Low-Frequency (<5 Hz) Irregular Mechanical Energy: A Possible Killer Application of Triboelectric Nanogenerator. *ACS Nano* **2016**, *10*, 4797.

(426) Wang, Z.; Song, J. Piezoelectric Nanogenerators Based on Zinc Oxide Nanowire Arrays. *Science* **2006**, *312*, 242.

(427) Wang, Z. On Maxwell's displacement current for energy and sensors: the origin of nanogenerators. *Mater. Today* **2017**, *20*, 74.

(428) Wang, S.; Lin, L.; Xie, Y.; Jing, Q.; Niu, S.; Wang, Z. Sliding-Triboelectric Nanogenerators Based on In-Plane Charge-Separation Mechanism. *Nano Lett.* **2013**, *13*, 2226.

(429) Yang, Y.; Zhang, H.; Chen, J.; Jing, Q.; Zhou, Y.; Wen, X.; Wang, Z. Single-Electrode Based Sliding Triboelectric Nanogenerator for Self-Powered Displacement Vector Sensor System. *ACS Nano* **2013**, *7*, 7342.

(430) Xie, Y.; Wang, S.; Niu, S.; Lin, L.; Jing, Q.; Yang, J.; Wu, Z.; Wang, Z. Grating Structured Freestanding Triboelectric-Layer Nanogenerator for Harvesting Mechanical Energy at 85% Total Conversion Efficiency. *Adv. Mater.* **2014**, *26*, 6599.

(431) Lee, J.; Ye, B.; Baik, J. Research Update: Recent progress in the development of effective dielectrics for high-output triboelectric nanogenerator. *APL Mater.* **2017**, *5*, No. 073802.

(432) Li, J.; Wang, X. Research Update: Materials design of implantable nanogenerators for biomechanical energy harvesting. *APL Mater.* **2017**, *5*, No. 073801.

(433) Fan, F.-R.; Lin, L.; Zhu, G.; Wu, W.; Zhang, R.; Wang, Z. Transparent Triboelectric Nanogenerators and Self-Powered Pressure Sensors Based on Micropatterned Plastic Films. *Nano Lett.* **2012**, *12*, 3109.

(434) Bai, P.; Zhu, G.; Jing, Q.; Yang, J.; Chen, J.; Su, Y.; Ma, J.; Zhang, G.; Wang, Z. Membrane-Based Self-Powered Triboelectric Sensors for Pressure Change Detection and Its Uses in Security Surveillance and Healthcare Monitoring. *Adv. Funct. Mater.* **2014**, *24*, 5807.

(435) Lin, L.; Wang, S.; Xie, Y.; Jing, Q.; Niu, S.; Hu, Y.; Wang, Z. Segmentally Structured Disk Triboelectric Nanogenerator for Harvesting Rotational Mechanical Energy. *Nano Lett.* **2013**, *13*, 2916.

(436) Bao, Y.; Wang, R.; Lu, Y.; Wu, W. Lignin biopolymer based triboelectric nanogenerators. *APL Mater.* **2017**, *5*, No. 074109.

(437) Kim, S.; Gupta, M.; Lee, K.; Sohn, A.; Kim, T.; Shin, K.-S.; Kim, D.; Kim, S.; Lee, K.; Shin, H.-J.; Kim, D.-W.; Kim, S.-W. Transparent Flexible Graphene Triboelectric Nanogenerators. *Adv. Mater.* **2014**, *26*, 3918.

(438) Liu, J.; Goswami, A.; Jiang, K.; Khan, F.; Kim, S.; McGee, R.; Li, Z.; Hu, Z.; Lee, J.; Thundat, T. Direct-current triboelectricity generation by a sliding Schottky nanocontact on MoS_2 multilayers. *Nat. Nanotechnol.* **2018**, *13*, 112.

(439) Diaz, A. F.; Felix-Navarro, R. M. A semi-quantitative tribo-electric series for polymeric materials: the influence of chemical structure and properties. *J. Electrost.* **2004**, *62*, 277.

(440) The NOMAD Laboratory−A European Centre of Excellence. https://nomadrepository.eu/. Online; accessed Aug 27, 2019.

(441) Pizzi, G.; Cepellotti, A.; Sabatini, R.; Marzari, N.; Kozinsky, B. AiiDA: automated interactive infrastructure and database for computational science. *Comput. Mater. Sci.* **2016**, *111*, 218−230.

(442) Castle, G. Contact charging between insulators. *J. Electrost.* **1997**, *40−41*, 13−20.

(443) Cheng, G.-G.; Jiang, S.-Y.; Li, K.; Zhang, Z.-Q.; Wang, Y.; Yuan, N.-Y.; Ding, J.-N.; Zhang, W. Effect of argon plasma treatment on the output perfomance of triboelectric nanogenerator. *Appl. Surf. Sci.* **2017**, *412*, 350−356.

(444) Kim, D.; Tcho, I.-W.; Jin, I.; Park, S.-J.; Jeon, S.-B.; Kim, W.-G.; Cho, H.-S.; Lee, H. S.; Jeoung, S.; Choi, Y.-K. Direct-laser-patterned friction layer for the output enhancement of a triboelectric nanogenerator. *Nano Energy* **2017**, *35*, 379−386.

(445) Nguyen, V.; Yang, R. Effect of humidity and pressure on the triboelectric nanogenerator. *Nano Energy* **2013**, *2*, 604−608.

(446) Lu, C.; Han, C.; Gu, G.; Chen, J.; Yang, Z.; Jiang, T.; He, C.; Wang, Z. Temperature Effect on Performance of Triboelectric Nanogenerator. *Adv. Eng. Mater.* **2017**, *19*, 1700275.

(447) Wen, Z.; Guo, H.; Zi, Y.; Yeh, M.-H.; Wang, X.; Deng, J.; Wang, J.; Li, S.; Hu, C.; Zhu, L.; Wang, Z. L. Harvesting Broad Frequency Band Blue Energy by a Triboelectric-Electromagnetic Hybrid Nanogenerator. *ACS Nano* **2016**, *10*, 6526.

(448) Wang, Z. Triboelectric nanogenerators as new energy technology and self-powered sensors−principles, problems and perspectives. *Faraday Discuss.* **2014**, *176*, 447−458.

(449) Guo, H.; Wen, Z.; Zi, Y.; Yeh, M.-H.; Wang, J.; Zhu, L.; Hu, C.; Wang, Z. A Water-Proof Triboelectric-Electromagnetic Hybrid Generator for Energy Harvesting in Harsh Environments. *Adv. Energy Mater.* **2016**, *6*, 1501593.

(450) Zhu, G.; Lin, Z.-H.; Jing, Q.; Bai, P.; Pan, C.; Yang, Y.; Zhou, Y.; Wang, Z. Toward Large-Scale Energy Harvesting by a Nanoparticle-Enhanced Triboelectric Nanogenerator. *Nano Lett.* **2013**, *13*, 847.

(451) Goswami, A.; Dhandaria, P.; Pal, S.; McGee, R.; Khan, F.; Antić, Ž.; Gaikwad, R.; Prashanthi, K.; Thundat, T. Effect of interface on mid-infrared photothermal response of MoS_2 thin film grown by pulsed laser deposition. *Nano Res.* **2017**, *10*, 3571.

(452) Park, J.; Salmeron, M. Fundamental Aspects of Energy Dissipation in Friction. *Chem. Rev.* **2014**, *114*, 677−711.

(453) Nonnenmacher, M.; O'Boyle, M.; Wickramasinghe, H. Kelvin probe force microscopy. *Appl. Phys. Lett.* **1991**, *58*, 2921−2923.

(454) Wang, H.; Huang, C.-C.; Polcar, T. Controllable Tunneling Triboelectrification of Two-Dimensional Chemical Vapor Deposited MoS_2. *Sci. Rep.* **2019**, *9*, 334.

(455) Drolle, E.; Bennett, W.; Hammond, K.; Lyman, E.; Karttunen, M.; Leonenko, Z. Molecular dynamics simulations and Kelvin probe force microscopy to study of cholesterol-induced electrostatic nanodomains in complex lipid mixtures. *Soft Matter* **2017**, *13*, 355−362.

(456) Korir, K.; Cicero, G.; Catellani, A. Piezoelectric properties of zinc oxide nanowires: an ab initio study. *Nanotechnology* **2013**, *24*, 475401−475406.

(457) Seol, M.-L.; Han, J.-W.; Moon, D.-I.; Meyyappan, M. Hysteretic behavior of contact force response in triboelectric nanogenerator. *Nano Energy* **2017**, *32*, 408−413.

(458) Cammarata, A.; Polcar, T. Electro-vibrational coupling effects on "intrinsic friction" in transition metal dichalcogenides. *RSC Adv.* **2015**, *5*, 106809.

(459) Cammarata, A.; Polcar, T. Tailoring Nanoscale Friction in MX_2 Transition Metal Dichalcogenides. *Inorg. Chem.* **2015**, *54*, 5739.

(460) Cammarata, A.; Polcar, T. Layering effects on low frequency modes in n-layered MX_2 transition metal dichalcogenides. *Phys. Chem. Chem. Phys.* **2016**, *18*, 4807.

(461) Cammarata, A.; Polcar, T. Vibrational contributions to intrinsic friction in charged transition metal dichalcogenides. *Nanoscale* **2017**, *9*, 11488.

(462) Irving, B.; Nicolini, P.; Polcar, T. On the lubricity of transition metal dichalcogenides: an ab initio study. *Nanoscale* **2017**, *9*, 5597.

(463) Cammarata, A.; Nicolini, P.; Simonovic, K.; Ukraintsev, E.; Polcar, T. Atomic-scale design of friction and energy dissipation. *Phys. Rev. B: Condens. Matter Mater. Phys.* **2019**, *99*, No. 094309.